

**Carrier Dynamics of Colloidal Solutions and Arrays of Lead
Chalcogenide Quantum Dots**

by

Danielle M. Buckley

B.S., University of Texas at San Antonio, 2006

A thesis submitted to the
Faculty of the Graduate School of the
University of Colorado in partial fulfillment
of the requirements for the degree of
Doctor of Philosophy
Department of Chemistry and Biochemistry

2014

This thesis entitled:
Carrier Dynamics of Colloidal Solutions and Arrays of Lead Chalcogenide Quantum Dots
written by Danielle M. Buckley
has been approved for the Department of Chemistry and Biochemistry

David Jonas

Prof. Gordana Dukovic

Date _____

The final copy of this thesis has been examined by the signatories, and we find that both the content and the form meet acceptable presentation standards of scholarly work in the above mentioned discipline.

Buckley, Danielle M. (Ph.D., Physical Chemistry)

Carrier Dynamics of Colloidal Solutions and Arrays of Lead Chalcogenide Quantum Dots

Thesis directed by Prof. David Jonas

While quantum dots (QDs) potentially offer routes to increase the efficiency of solar energy harvesting, fundamental photophysical processes, such as carrier cooling, are still not fully understood. Ultrafast degenerate pump-probe spectroscopy is used to investigate carrier dynamics in both isolated colloidal quantum dots, uncoupled quantum dot arrays, and most importantly, coupled quantum dot arrays that may be suitable for device applications. Pumping and probing at the same wavelength overcomes frequency-dependent absorption cross-section issues that may complicate results. Additionally, utilizing novel sample refreshing techniques minimizes photodegradation and photocharging.

The time-dependent behavior of PbS nanocrystal arrays and colloidal solutions is measured at the band gap with sub-100fs time resolution and at higher photon energies with sub-40fs resolution. Different ligand treatments are employed to exchange bulky long-chain organics for shorter chains with different functional groups. Ligand exchange is performed on films as well as a colloidal solution.

Investigations of 2nm diameter PbS quantum dots at the band gap and at 1.4 times the band gap show the biexciton lifetime in an uncoupled array is the same as in colloidal solution. This is in contrast to previous reports of different decay times for various sizes of PbSe QD solutions and uncoupled arrays. Degenerate studies of these same 2nm diameter PbS QDs as coupled arrays at the band gap indicate substantial excited state absorption that increases with increasing pump fluence.

Dedication

To my mom, Gloria Buckley, who started me on this path.

Acknowledgements

There is a long list of people I must thank but will begin by thanking my advisor, Dr. David Jonas, for welcoming me into his lab and allowing me to play with lasers and quantum dots. His energy and incredible intelligence are a force to be reckoned with and make him not just a wonderful source of information and scientific anecdotes, but also a brilliant mentor. And of course as with any thesis, this was a group effort and I could not have done it without the stimulating discussions that happened with others in my group, as well as the ridiculous ones that sometimes took place. A big ‘thank you’ to Trevor Courtney, Bill Peters, Rob Hill, Jordan Corbman, and Byungmoon Cho, with whom I spent the majority of my time and who have since moved on from the Jonas Group; to Austin Spencer, Vivek Tiwari, Dmitry Baranov, and Sam Park who were there with me to the end, proof-reading and watching me practice the same presentation a million times; and to the newer group members, Anna Curtis and Jisu Ryu, who were always willing to help where they could. Finally, to my friends and family - those in Colorado, Texas, and everywhere - you were and are a constant source of support. I always looked forward to a relaxing ‘cribbage night’ with Drs. Sydney Kaufman and Jennifer Lubbeck after a long day in the lab, or having a Sunday night dinner with Jess Townsend, Nathan Hinkley, the Courtney’s, and the Arpin’s. And whether on a phone call or a visit to Colorado, Carolyn Birge and Jennifer Lynch have always been there to share in big news, good or bad, for almost my entire life. But nothing made me happier than visiting my nephews, Wyatt, Haydin, and Ryder - they always put a smile on my face no matter how much work I still had left to do. Thank you to my sister and brother, Natalie and Christopher, who are my best friends; to my brother-in-law Chris who was a great sounding board for tough decisions; to Aunt Vick who gave the best gifts to decorate my office with; to my step-mom Sharon, who was always free to listen; and to my dad, Jack Buckley, who’s love and support got me here.

Contents

Chapter

| | | |
|----------|---|----|
| 1 | Introduction | 1 |
| 1.1 | Photovoltaic Background | 1 |
| 1.2 | Lead Chalcogenides | 2 |
| 1.3 | Bulk Semiconductors vs Quantum Dots | 4 |
| 1.3.1 | Bulk | 4 |
| 1.3.2 | Quantum Dots | 5 |
| 1.4 | Ultrafast Experiments | 7 |
| 1.4.1 | Poisson Assumptions | 7 |
| 1.4.2 | Quantum Efficiency | 8 |
| 1.4.3 | Photocharging and Photodegradation | 12 |
| 1.5 | Ligand Exchange and Film Studies | 12 |
| 1.6 | Conclusions | 16 |
| 1.7 | References | 18 |
| | Bibliography | 18 |
| 2 | Small Lead Sulfide Quantum Dots in Colloidal Solutions and Uncoupled Arrays | 22 |
| 2.1 | Introduction | 22 |
| 2.2 | Experimental Procedure | 23 |

| | | |
|---------------------|---|----|
| 2.2.1 | Sample Preparation | 23 |
| 2.2.2 | Pump-Probe Measurements | 24 |
| 2.3 | Results & Discussion | 27 |
| 2.3.1 | Pump-probe at the Band Gap | 27 |
| 2.3.2 | 2nm diameter PbS at less than $2E_g$ | 39 |
| 2.4 | Conclusion | 43 |
| 2.5 | References | 47 |
| Bibliography | | 47 |
| 3 | Octylamine and 1,2-Ethanedithiol Treated Lead Sulfide Quantum Dots | 49 |
| 3.1 | Introduction | 49 |
| 3.2 | Experimental Procedure | 50 |
| 3.2.1 | Sample Preparation | 50 |
| 3.2.2 | Characterization | 51 |
| 3.2.3 | Pump-Probe Measurements | 54 |
| 3.3 | Results & Discussion | 54 |
| 3.3.1 | Octylamine-treated PbS | 54 |
| 3.3.2 | EDT-treated PbS | 64 |
| 3.4 | Conclusion | 68 |
| 3.5 | References | 70 |
| Bibliography | | 70 |
| 4 | High energy transitions in Lead Sulfide Quantum Dots | 72 |
| 4.1 | Introduction | 72 |
| 4.2 | Experimental Procedure | 74 |
| 4.2.1 | Sample Preparation | 74 |

| | | |
|---------------------|--|------------|
| 4.2.2 | Characterization | 75 |
| 4.2.3 | Spectroscopic Measurements | 75 |
| 4.3 | Results & Discussion | 78 |
| 4.3.1 | Degenerate Pump-probe Signals | 82 |
| 4.4 | Linear Absorption Analysis | 84 |
| 4.5 | Conclusion | 89 |
| 4.6 | References | 92 |
| Bibliography | | 92 |
| 5 | E_1 transition in Lead Sulfide Quantum Dots Treated with 1,2-Ethanedithiol | 93 |
| 5.1 | Introduction | 93 |
| 5.2 | Experimental Procedure | 94 |
| 5.2.1 | Sample Preparation | 94 |
| 5.2.2 | Spectroscopic Measurements | 98 |
| 5.3 | Results & Discussion | 98 |
| 5.4 | Conclusion | 100 |
| 5.5 | References | 106 |
| Bibliography | | 106 |
| Bibliography | | 107 |
| Bibliography | | 107 |
| Appendix | | |
| A | Additional Figures | 112 |

Tables

Table

| | | |
|-----|--|----|
| 2.1 | Coefficients and decay times for the two colloidal solutions of 1.9nm diameter oleate-capped PbS in hexane based on exponential fits to non-normalized transients, recorded with a pulse spectrum centered at 800nm. A , B , and C are coefficients in the multi-exponential fits while τ_x denotes the time constant for decay, $Ae^{-t/\tau_3} + Be^{-t/\tau_2} + Ce^{-t/\tau_1}$. Dashes denote no values associated with the respective coefficient and τ | 33 |
| 2.2 | Coefficients and decay times for the array of 1.9nm diameter oleate-capped PbS QDs based on exponential fits to non-normalized transients, recorded with the pulse spectrum centered at 800nm. A , B , and C are coefficients in the multi-exponential fits while τ_x denotes the time constant for decay, $Ae^{-t/\tau_3} + Be^{-t/\tau_2} + Ce^{-t/\tau_1}$. Dashes denote no values associated with the respective coefficient and τ | 34 |
| 2.3 | Coefficients and decay times for the 1.9nm diameter PbS solution and array based on exponential fits. A , B , and C are coefficients in the fit: $Ae^{-t/\tau_3} + Be^{-t/\tau_2} + Ce^{-t/\tau_1}$. All of the transients have a maximum negative signal around 200fs followed by decay to zero at less than 3ps. | 40 |
| 3.1 | Coefficients and decay times for 1.9nm diameter octylamine-treated PbS in hexane and as an array based on the multi-exponential fit, $Ae^{-t/\tau_3} + Be^{-t/\tau_2} + Ce^{-t/\tau_{2'}} + De^{-t/\tau_1}$. Values in italics denote those taken from the fit of the transient with the lowest $\langle N \rangle$, rather than an independent fit, and dashes denote no values associated with the respective coefficient and τ | 63 |

| | | |
|-----|--|-----|
| 3.2 | Coefficients and decay times for 1.9nm diameter EDT-treated PbS arrays based on multiexponential fits of individual transients, $Ae^{-t/\tau_2} + Be^{-t/\tau_{2'}} + Ce^{-t/\tau_1}$. A , B , and C are coefficients in the fits. | 65 |
| 5.1 | Coefficients and decay times for colloidal solution and EDT-treated array of 4nm diameter PbS based on exponential fits. A , B , and C are coefficients in the multiexponential fit, $Ae^{-t/\tau_{2'}} + Be^{-t/\tau_2} + Ce^{-t/\tau_1}$. Similar to other samples, discussed in Chapters 2 and 3, an additional short lifetime, labeled $\tau_{2'}$ appears here, but is an order of magnitude less than the expected AR lifetime. | 100 |

Figures

Figure

- 1.1 Absorption of a high energy photon excites an electron (black) from the valence band (VB) to the conduction band (CB), leaving behind a positively-charged hole (white). Excess energy absorbed in the bulk results in either the production of multiple electron-hole pairs through impact ionization or energy lost through phonon cooling before radiative recombination of the remaining electron and hole. 5
- 1.2 **a)** Optical absorption spectra showing the first absorption peak of colloidal CdTe quantum dots, increasing in diameter with increasing wavelength, and **b)** a representation of the quantization and increase in band gap with decreasing semiconductor size, including differences in wave function and confinement of the electron (top) and hole (bottom) due to their different effective masses. Reprinted with permission from Rühle, et al. Quantum-dot-sensitized solar cells. *ChemPhysChem*. Copyright 2010 Wiley-VCH. [23] 6
- 1.3 Representation of a typical trace found with TA when exciting above the CM threshold (blue) and below the CM threshold (green), both with low pump fluence. *a* and *b* are used to extrapolate quantum yield, as described in the text. 9

- 1.4 In each panel, the circles represent data obtained from time-resolved photoluminescence (TRPL), the crosses are from transient absorption (TA) data, and the diamonds are bulk values that the authors extrapolated from reference [22]. **a)** denotes an increase in quantum efficiency of quantum dots over bulk when evaluated against the normalized photon energy while **b)** shows bulk PbSe to be more efficient when absolute photon energy is considered. **c)** and **d)** further evaluate different perspectives by maintaining the absolute photon energy in the x-axis but using values that determine power conversion efficiency in a photovoltaic device and compare real and ideal multiexciton yields in the y-axis. Reprinted with permission from McGuire, et al. Apparent versus true carrier multiplication yields in semiconductor nanocrystals *Nano Letters*. Copyright 2010 American Chemical Society. [30] 11
- 1.5 Quantum dots are passivated with long-chain organic ligands, such as oleate (left), but ligand exchanges replace these with shorter organic molecules, such as 1,2-ethanedithiol, which reduces interdot spacing (right). 13
- 1.6 Absorption spectra of oleate-capped PbSe colloidal solutions and PbSe arrays that have undergone ligand exchange, which can lead to a red-shift and broadening of the first transition peak. Adapted with permission from **a)** Beard, et al. Variations in the quantum efficiency of multiple exciton generation for a series of chemically treated PbSe nanocrystal films. *Nano Letters*. Copyright 2009 American Chemical Society [41], **b)** Luther, et al. Structural, optical, and electrical properties of self-assembled films of PbSe nanocrystals treated with 1,2-ethanedithiol. *ACS Nano*. Copyright 2008 American Chemical Society [43], and **c)** Law, et al. Structural, Optical, and Electrical Properties of PbSe Nanocrystal Solids Treated Thermally or with Simple Amines. *Journal of the American Chemical Society*. Copyright 2008 American Chemical Society [42]. 14

- 1.7 Transient absorption data of 7.4 nm diameter colloidal oleate-capped PbSe quantum dots in trichloroethylene (TCE), a PbSe array treated with hydrazine (hy) in acetonitrile (CH_3CN), and a PbSe array treated with 1,2-ethanedithiol (EDT) in CH_3CN . All were taken at increasing pump fluence but with excitation at $1.6E_g$, well below the CM threshold energy, and probed at the first exciton peak. Reprinted with permission from Beard, et al. "Variations in the quantum efficiency of multiple exciton generation for a series of chemically treated PbSe nanocrystal films". *Nano Letters*. Copyright 2009 American Chemical Society. [41] 15
- 1.8 J_0 indicates the fluence and R_{pop} represents the ratio of the signal at short versus long times, or (a/b) from Figure 1.3, and is shown for excitation below and above the CM threshold. The MEG yield is reflected in the value of R_{pop} in the limit as J_0 goes to zero. The hy treated array shows a reduction in MEG compared to isolated colloidal PbSe in tetrachloroethylene while the EDT treated array indicates no MEG. Reprinted with permission from Beard, et al. "Variations in the quantum efficiency of multiple exciton generation for a series of chemically treated PbSe nanocrystal films". *Nano Letters*. Copyright 2009 American Chemical Society. [41] 16
- 2.1 The sample is only drop-cast onto one of the substrates, which is separated from the other window by a teflon spacer. Viton o-rings are pressed against both the outside of each substrate and the inner walls of the cell base by bevelled aluminum rings as the top of the cell is screwed onto the base, sealing the cell. 25
- 2.2 Linear absorption spectra of oleate-capped 2nm diameter PbS quantum dots in hexane and as an array. The colloidal solution is in blue [$E_g = 820\text{nm}$] and the array is in red [$E_g = 822\text{nm}$]. 25

| | | |
|-----|---|----|
| 2.3 | Linear absorption spectra of 2nm diameter PbS quantum dots in hexane and as an oleate-capped array. The colloidal solution is in blue [$OD(800nm) = 0.13$ and $E_g = 820nm$] and the array is in red [$OD(800nm) = 0.11$ and $E_g = 822nm$]. The pulse spectrum used for pump-probe experiments is overlaid as the dark red trace - it is roughly Gaussian with a center wavelength near 800nm. | 27 |
| 2.4 | Pump-probe transients, recorded with the pulse spectrum centered at 800nm, of the 1.9nm diameter oleate-capped PbS colloidal solution. The pump-induced change in probe transmission, ΔT is on the y-axis and multi-exponential fits to each transient, which are discussed later in the text, are overlaid in black. | 28 |
| 2.5 | Pump-probe transients, recorded with the pulse spectrum centered at 800nm, of the 1.9nm diameter oleate-capped PbS film. The pump-induced change in probe transmission, ΔT is on the y-axis and multi-exponential fits to each transient, which are discussed later in the text, are overlaid in black. | 29 |
| 2.6 | Pump-probe transients of 1.9nm diameter oleate-capped PbS in hexane (solution) and drop-cast array (film). The pump-induced change in probe transmission, ΔT , on the y-axis, is divided by the respective optical density and pump power, which is proportional to energy per pump pulse used to record each individual transient, U_{pump} . In the low excitation probability limit, $\Delta T/U_{pump}$ should not vary with U_{pump} | 30 |
| 2.7 | Transients for the oleate-capped film are normalized at long-times, the average amplitude between 0.5ns and 1ns, to illustrate differences in amplitude at early times, which indicates biexciton, trion, or possible multi-exciton population decay. | 31 |
| 2.8 | As for the film data in Figure 2.7, pump-probe transients for the oleate-capped solution are normalized at long-times, the average amplitude between 0.5ns and 1ns, to illustrate differences in amplitude at early times, indicating biexciton, trion, or possible multi-exciton population decay. | 31 |

- 2.9 The long-time normalized transients, recorded with the center of the pulse spectrum at 800 nm, of the PbS QDs in solution with $\langle N \rangle = 1.57$ and $\langle N \rangle = 0.0184$ are shown here. **a** is the amplitude at early times when the greatest contribution from multiexcitons is present and **b** is the initial single exciton contribution obtained from the lowest $\langle N \rangle$ transient. The ratio, **a/b** reflects the average number of excitons photoexcited per excited QD, which is 1.5 in this example. 34
- 2.10 (a/b), found from degenerate pump-probe transients recorded with the center of the pulse spectrum at 800nm, from the array (red) and the two solution samples (blue). These are compared to $\langle N_{eh} \rangle = \frac{\langle N \rangle}{1 - e^{-\langle N \rangle}}$ versus $\langle N \rangle$ (blue curve). Spatially averaged Poisson statistics apply at low $\langle N \rangle$ but are not valid once the sample is saturated at higher $\langle N \rangle$ 35
- 2.11 Transients of the first oleate-capped PbS colloidal solution, recorded with the center of the pulse spectrum at 800nm (shown in Figure 2.8), are normalized by their average amplitude at long-times, between 0.5 and 1ns. Assuming that the oleate-capped PbS solution transient with $\langle N \rangle = 0.0184$ includes only a single exciton decay signal, the larger amplitude at early times of transients with $\langle N \rangle = 1.57$, $\langle N \rangle = 0.431$, and $\langle N \rangle = 0.0431$ signify multi-exciton decay. 36
- 2.12 As in Figure 2.11, transients of the oleate-capped PbS array, recorded with the center of the pulse spectrum at 800nm (shown in Figure 2.7), are normalized by their average amplitude at long-times, between 0.5 and 1ns. Assuming that the PbS film transient with $\langle N \rangle = 0.0189$ includes only a single exciton decay signal, the larger amplitude at early times of transients with $\langle N \rangle = 1.56$, $\langle N \rangle = 0.443$, and $\langle N \rangle = 0.0443$ signify multi-exciton decay. 36

- 2.13 Linear absorption spectra of oleate-capped 2nm diameter PbS quantum dots in hexane and as an array. The colloidal solution is in blue [$OD(574nm) = 0.34$ and $E_g = 820nm$] and the array is in red [$OD(574nm) = 0.36$ and $E_g = 822nm$]. They have ODs of 0.15 and 0.17 at their respective E_g , 820nm and 822nm. The pulse spectrum used for pump-probe experiments is overlaid as the green trace, centered at 574nm. 40
- 2.14 Degenerate pump-probe transients, recorded with the pulse spectrum centered at 574nm, of 2nm diameter PbS solution ($\langle N \rangle = 0.035$ and 0.13) and film ($\langle N \rangle = 0.059$ and 0.11), taken while samples were refreshed between laser shots. The pump-induced change in probe transmission, ΔT , on the y-axis, is divided by the respective pump power, which is proportional to energy per pump pulse of the individual spectrum, U_{pump} . Although there is a difference in amplitude between solution and film, the overall shape appears similar within the signal to noise. 41
- 2.15 Degenerate pump-probe transients, recorded with the center of the pulse spectrum at 574nm, of 2nm diameter oleate-capped PbS in hexane, $\langle N \rangle = 0.035$ and 0.13, with multi-exponential fits. Transients and fits are shown out to 200ps (left) and to 5ps (right), although fits were made out to 500ps. The initial decays at early time appear very similar but some deviation can be seen at later times. The $\langle N \rangle = 0.035$ transient appears to decrease at long times (become more negative) but it is difficult to quantify because of the noise. 42
- 2.16 Pump-probe transients, recorded with the pulse spectrum centered at 574nm, for a film made from 2nm diameter oleate-capped PbS quantum dots, $\langle N \rangle = 0.059$ and 0.11, with multi-exponential fits. The transients are shown out to 200ps (left) and 5ps (right). 42

- 2.17 Pump-probe transients, recorded with a pulse spectrum centered at 574nm, for a film made from 2nm diameter oleate-capped PbS and for colloidal solution of the same dots, $\langle N \rangle = 0.059$ and 0.035, normalized at 1ps in order to compare the overall shape of decay and recovery of the signal. Transients are shown out to 100ps (left) and 2.5ps (right). With the normalization, it is apparent that the solution and film have the same decay and recovery dynamics (within the signal-to-noise) over the first hundred picoseconds. 44
- 2.18 Degenerate pump-probe transients, recorded with the pulse spectrum centered at 574nm, of 2nm diameter PbS solution and film, $\langle N \rangle = 0.13$ and 0.11, normalized at 1ps in order to compare the overall shape of the decay and recovery of the signal. The transients are again shown out to 100ps (left) and 2.5ps (right). With the normalization, it is apparent that the solution and film have the same decay and recovery dynamics within the signal-to-noise, including a small dip that occurs at approximately 100fs and is not seen in samples at lower $\langle N \rangle$ 44
- 3.1 Linear absorption spectra of 2nm diameter PbS quantum dots in hexane. The oleate-capped PbS is in blue and the octylamine-treated PbS is in purple [$OD(800nm) = 0.078$ and $E_g = 830nm$]. The blue y-axis shows OD for the oleate-capped PbS while the purple axis shows OD for the octylamine-treated PbS. The inset highlights the small red-shift and broadening of the first exciton peak after treatment. 53
- 3.2 Linear absorption spectra of 2nm diameter PbS quantum dot arrays. The oleate-capped PbS is in red; the octylamine-treated PbS is in blue [$OD(800nm) = 0.032$ and $E_g = 832nm$]; the first PbS sample treated with EDT is in green [$OD(800nm) = 0.19$ and $E_g = 867nm$]; and the second PbS sample treated with EDT is in dark brown [$OD(800nm) = 0.13$ and $E_g = 876nm$]. The inset shows the arrays normalized at 800nm. 53

| | | |
|-----|--|----|
| 3.3 | Images of 1.9nm diameter oleate-capped PbS (a) and octylamine-treated PbS (b) taken with a Phillips CM30 TEM at NREL. Octylamine-treated QDs are more closely spaced than oleate-capped dots due to the shorter ligand length. The text provides a further description of differences. | 55 |
| 3.4 | Pump-probe transients recorded using pulse spectra centered at 800nm for octylamine-treated PbS in hexane solution ($OD(800nm) = 0.078$) and as a drop-cast film ($OD(800nm) = 0.031$). The pump-induced change in probe transmission, ΔT , is divided by the respective energy per pump pulse and OD of the sample. | 56 |
| 3.5 | Pump-probe transients recorded using pulse spectra centered at 800nm for octylamine-treated PbS in hexane. S1(purple) and S2 (blue) represent solutions taken from the same stock solution at different times and diluted to similar ODs. S2 transients were taken less than two months after S1 transients. The pump-induced change in probe transmission, ΔT , is divided by the respective energy per pump pulse and OD of the sample. | 58 |
| 3.6 | Pump-probe transients, recorded using pulse spectra centered at 800nm, of the two octylamine-treated PbS solutions from Figure 3.5 are normalized at long times to find (a/b) , as described in the text. | 59 |
| 3.7 | The octylamine-treated film in orange and the two solution samples in purple are compared to the expected number of excitons using Poisson assumptions. The spatially averaged number of photons absorbed per QD, $\langle N \rangle$, is shown on the x-axis, while the experimental indicator for the number of excitons per QD, (a/b) , is on the y-axis. The (a/b) ratio is experimentally determined but the curve, $\langle N_{eh} \rangle = \frac{\langle N \rangle}{1 - e^{-\langle N \rangle}}$, is the number of excitons expected based on Poisson assumptions. These equations are discussed in Chapter 2. Although the data points for S1 and the film are similar to one another, data from S2 shows an early departure from the other samples as well as the curve. | 60 |

- 3.8 Long-time normalized pump-probe transients of the first sample of 2nm diameter octylamine-treated PbS in hexane (S1) for $\langle N \rangle = 0.431$ and $\langle N \rangle = 0.0431$ (shown in Figure 3.6) with the normalized multiple of the lowest excitation probability signal, $\langle N \rangle = 0.0184$, subtracted. 61
- 3.9 Long-time normalized pump-probe transients of the second sample of 2nm diameter octylamine-treated PbS in hexane (S2) for $\langle N \rangle = 0.454$, $\langle N \rangle = 0.137$, $\langle N \rangle = 0.0454$, and $\langle N \rangle = 0.0190$ (shown in Figure 3.6) with the normalized multiple of the lowest excitation probability signal, $\langle N \rangle = 0.0085$, subtracted. 62
- 3.10 Long-time normalized pump-probe transients of film made from 2nm diameter octylamine-treated PbS for $\langle N \rangle = 0.333$ and $\langle N \rangle = 0.155$ (shown in Figure 3.4), with the normalized multiple of the lowest excitation probability signal, $\langle N \rangle = 0.0333$, subtracted. 62
- 3.11 Pump-probe transients, recorded using a pulse spectrum centered at 800nm, of the first EDT-treated array (EDT1) are shown ($OD(800nm) = 0.19$). The inset shows that transients approach zero very early compared to uncoupled arrays. The positive amplitude at early times of the transient with the lowest excitation probability, $\langle N \rangle = 0.013$, reflects a ground state bleach, but an initial negative signal (induced absorption) appears at time zero for a higher excitation probability of 0.140. This signal quickly recovers, within 200fs, and becomes positive. Raising $\langle N \rangle$ to 0.310 increases the negative signal at time zero, which does not decay to zero until approximately 1.5ps. Higher $\langle N \rangle$ also appears to prevent ground state bleach from making large signal contributions. 66
- 3.12 Pump-probe transients, recorded using a pulse spectrum centered at 800nm, of the second EDT-treated film, EDT2 ($OD(800nm) = 0.13$). The positive transient signals at time zero (see inset) indicate ground state bleach dominates, regardless of $\langle N \rangle$. Similar to transients for EDT1, the signals quickly approach zero within about 100ps. 67

- 4.1 Bulk band structure of PbS from Kohn et al. (black) with E_0 , E_1 , and E_2 transition labels added (brown). The E_0 transition at the L -point is referred to as E_g in quantum dots. The E_1 transition in bulk is assigned to a high energy peak in quantum dot spectra that increases in energy with decrease in QD size. The E_2 bulk transition is also assigned to QD spectra but is regarded as bulk-like, with changing QD diameters having little or no affect on the transition. [3] The dashed line at the L -point references the transition from L_6^+ in the valence band to L_6^- in a higher conduction band than for the E_0 transition and will be mentioned later in the text. *Adapted from Figure 9 of Kohn, et. al, Electronic band structure and optical properties of PbTe, PbSe, and PbS. Physical Review B vol. 8, p.1482, 1973. [2]* . . . 73
- 4.2 Linear absorption spectra of oleate-capped PbS QDs synthesized in the lab (1.6nm), purchased from Voxel Inc. (1.9, 2.3, and 2.5nm), and purchased from Evident Technologies (4.3, 5.2, 7.8nm). The molar extinction coefficient ε ($M^{-1}cm^{-1}$) on the y-axis is divided by the nanocrystal volume in this figure to enable a direct comparison of spectra. 76
- 4.3 Images taken at NREL with a Phillips CM30 TEM with the assistance of Dr. Joseph Luther. a) 1.9nm diameter PbS from Voxel, b) 2.5nm diameter PbS from Voxel, c) 4.3nm diameter PbS from Evident, and d) 7.8nm PbS from Evident. 77
- 4.4 Degenerate pump-probe transients, taken with the pulse spectrum centered at different wavelengths, for the 4.3nm PbS QDs purchased from Evident ($E_g = 1168nm$ and $E_1 = 556nm$). ESA is the predominate feature at all of the wavelengths but a short-lived, early-time positive signal is seen for at 550nm which indicates GSB. The inset shows the GSB at around 100fs for $\lambda_{p-p} = 550nm$ 79

- 4.5 Degenerate pump-probe transients, taken with the pulse spectrum centered at different wavelengths, for the 5.2nm PbS QDs purchased from Evident ($E_g = 1434\text{nm}$ and $E_1 = 584\text{nm}$). As in Figure 4.4, ESA dominates each transient but an early, short-lived bleach is seen with $\lambda_{p-p} = 570\text{nm}$, again, near the center of the E_1 transition for this size of QD. Additionally, $\lambda_{p-p} = 507\text{nm}$ shows an increased decay toward zero, compared to other transients, beginning around 500fs. The inset shows GSB around 100fs for $\lambda_p - p = 570\text{nm}$ 80
- 4.6 Degenerate pump-probe transients, taken with the pulse spectrum centered at different wavelengths, for the 7.8nm PbS QDs purchased from Evident ($E_g = 1800\text{nm}$ and $E_1 = 610\text{nm}$). Similar to transients of 4.3nm and 5.2nm QDs, the 7.8nm QDs show increasing ESA at early times ($< 500\text{fs}$) for all λ_{p-p} except that near the E_1 peak, $\lambda_{p-p} = 610\text{nm}$. Like the 5.2nm QD transients with $\lambda_{p-p} = 507\text{nm}$, there is a decay toward zero beginning around 500fs, but in this case it is much larger and reaches zero by 3ps. Additionally, a lesser rise is seen with $\lambda_{p-p} = 525\text{nm}$ 81
- 4.7 The first 1ps of transients, taken with the pulse spectrum centered at different wavelengths, for the 7.8nm PbS QDs (Figure 4.6) is shown. GSB is observed around 100fs at $\lambda_{p-p} = 610\text{nm}$ 81
- 4.8 Approximations of the L -point electronic energy levels are shown. A photon with $\lambda > E_1$ only contains enough energy to excite an electron from the L -point VB to the lowest lying L -point CB. The initial pump pulse (red) excites an electron and the subsequent probe pulse (pink) may experience GSB, ESE (dashed), or ESA arising from the same electron and hole (left). Electrons and holes may also relax to the edges of the CB and VB, respectively, usually within a few hundred femtoseconds (gray dashed arrows). It is also possible for the excitation of one electron-hole pair to affect the excitation of another carrier, generating a two-particle ESA pump-probe signal (right). 83

- 4.9 A similar picture of the Σ - (left) and L - (right) points are shown as in Figure 4.8, but a photon with $\lambda \approx E_1$ now has enough energy to excite an electron at either point. The initial pump pulse (dark green) may excite an electron at either the L -point or the Σ - point. The subsequent probe pulse (light green) may experience GSB, ESE (dashed), or ESA (solid). Again the dashed, gray arrows represent electron and hole cooling to the band edges. As in Figure 4.8, two-particle ESA signals are possible, but not shown here. 85
- 4.10 Similar to Figure 4.9, a pump photon with $\lambda < E_1$ (dark blue) has enough energy to excite an electron at either the L -point or Σ - point. The subsequent probe pulse (light blue) may experience GSB, ESE (dashed), or ESA (solid). Again the dashed, gray arrows represent electron and hole cooling to the band edges and as in Figure 4.8, two-particle ESA signals are possible, but not shown here. 86
- 4.11 Absorption spectra of 2.5nm diameter PbS QDs are shown in green with the second derivative in blue. Fits to absorption spectra and the second derivative are overlaid in black. **a** is the fit using only a single Gaussian to fit the E_1 transition while **b** uses two Gaussians to fit the area around the E_1 transition. Only the Gaussians fit to E_1 transitions are shown under each absorption curve. While there is little difference between the fits at lower energies, the second derivative fit using two Gaussians at E_1 (**b**) accounts for the second derivative minimum at 2.65eV and allows a better fit for the minimum at 3.2eV compared to the fit with only a single Gaussian at the E_1 transition (**a**). 88

- 4.12 Absorption spectra of 7.8nm diameter PbS QDs are shown in green with the second derivative in blue. Fits to absorption spectra and the second derivative are overlaid in black. **a** is the fit using only a single Gaussian to fit the E_1 transition while **b** uses two Gaussians to fit the area around the E_1 transition. Only the Gaussians fit to E_1 transitions are shown under each absorption curve. Again, there is little difference between the fits at lower energies, but the second derivative fit using two Gaussians at E_1 (**b**) better accounts for the shoulders seen around 2.3eV and 2.8eV when compared to the fit with only a single Gaussian at the E_1 transition (**a**). . . . 88
- 4.13 **a)** Full width at the half maximum (FWHM) of the single Gaussian fit for the E_1 transition versus the QD diameter (nm). **b)** The y-axis is proportional to the oscillator strength (f_{if}) of the E_1 transition and the x-axis is the volume (nm^3) of the QD. Blue diamonds represent f_{if} for the single Gaussian fit to the E_1 transition while red squares are the sum of f_{if} for the fit with two Gaussians at the E_1 transition. Similar comparisons are shown using the energy of the E_1 peak, instead of QD size, in the Appendix. **c)** & **d)** The same plots that are described for **a** and **b** are shown here for E_g to illustrate trends for a band gap transition, but it should be noted that the first exciton peaks of the smallest size of QDs likely contain contributions from other transitions that overlap as it blue-shifts. 90
- 5.1 Linear absorption spectra of the oleate-capped PbS QD colloidal solution in hexane and the EDT-treated PbS array after exposure to atmosphere. The centers of the pulse spectra, which occur at 560nm and 570nm, used in the experiment are overlaid in green and red, respectively. Similar to previous reports [1,2] and results in Chapter 3, EDT-treatment results in an offset of the absorption spectrum and a red-shift of the first exciton peak, which is discussed further in the text. 96

- 5.2 Linear absorption spectra of the EDT-treated film in air free conditions shortly after being deposited on the substrate (purple) and after being exposed to atmosphere during data collection (green). The overall shape of the spectrum at higher energies appears the same but includes a blue-shift of the E_1 transition from 585nm to 560nm. A more obvious shift is seen at longer wavelengths where the center of the first exciton peak changes from 1230nm to 1180nm. 97
- 5.3 Degenerate pump-probe transients, recorded with the center of the pulse spectrum at 570nm and refreshed between laser shots with a 40ms resampling time, of 4nm diameter PbS as a colloidal solution in hexane and as an EDT-treated array with $\langle N \rangle \approx 0.25$. The inset shows the transients over the first 50ps and illustrates the differences at early times. Both transients are normalized by the average pump power. 101
- 5.4 Degenerate pump-probe transients, recorded with the center of the pulse spectrum at 560nm and at 570nm and refreshed between laser shots with a 40ms resampling time, of 4nm diameter PbS as an EDT-treated array with $\langle N \rangle \approx 0.25$ and ≈ 0.50 . Transients are normalized by average pump power. At both excitation wavelengths, transients display a large negative signal at early times, indicating ESA. The inset illustrates the similarity in the shape of the transients over the first 50ps. 102
- 5.5 Degenerate pump-probe transients, recorded with the center of the pulse spectrum at 560nm and at 570nm and refreshed between laser shots with a 40ms resampling time, of 4nm diameter PbS as an EDT-treated array with $\langle N \rangle \approx 0.25$ and ≈ 0.50 . Transients are normalized at 1ps to compare the shape and the early time dynamics when the pulse spectrum is centered at 560nm and at 570nm. With 1ps normalization, transients exhibit agreement within the signal-to-noise at both early (inset) and late times except for a small bleach at time zero that occurs in transients excited at 560nm (see Figure 5.6), but is not seen in any transients at 570nm. 103

- 5.6 The first picosecond of degenerate pump-probe transients, recorded with the center of the pulse spectrum at 560nm and refreshed between laser shots with a 40ms resampling time, of the EDT-treated array of PbS. Transients are normalized by the average pump power. An initial, short-lived bleach is observed that is not seen in transients of the array or solution when the pulse spectrum is centered at 570nm. This positive signal begins just before time zero and continues to almost 200fs, indicating an initial GSB. 104
- A.1 Chem-VacTM Chem-Cap[®] valve with single sidearm from Chemglass Life Sciences. . 112
- A.2 A second set of degenerate pump-probe transients were recorded in addition to those shown in Chapter 2, with a pulse spectrum centered at 800nm, of 1.9nm oleate-capped PbS QDs in hexane (OD(800nm)=0.12 and E_g =820nm). Transients were normalized at long-time using the average amplitude between 0.5ns and 1ns. 113
- A.3 Assuming that the oleate-capped PbS solution transient with $\langle N \rangle = 0.0081$ includes only a single exciton decay signal, tail-matching multiples are subtracted from the $\langle N \rangle = 1.57$, $\langle N \rangle = 0.431$, and $\langle N \rangle = 0.0431$ transients of the solution shown in Figure A.2. The resulting data and fits are shown here. 114
- A.4 Linear absorption spectra of 1.9nm diameter octylamine-treated PbS in hexane. Individual samples were taken at different times from stock solution stored in the glovebox. S1 was taken on September 24, 2012 and S2 was taken on November 13, 2012, less than two months apart. 114

- A.5 Absorption spectra of 4.3nm diameter PbS QDs are shown in green with the second derivative in blue. Fits to absorption spectra and the second derivative are overlaid in black and based on a third order polynomial background with a sum of Gaussians to describe discrete transitions. The figure on the left is a fit using only a single Gaussian at the E_1 transition while the figure on the right uses two Gaussians to fit the area around the E_1 transition. Only the Gaussians fit at E_1 transitions are shown under each absorption curve. 115
- A.6 Absorption spectra of 5.2nm diameter PbS QDs are shown in green with the second derivative in blue. Fits to absorption spectra and the second derivative are overlaid in black and based on a third order polynomial background with a sum of Gaussians to describe discrete transitions. The figure on the left is a fit using only a single Gaussian at the E_1 transition while the figure on the right uses two Gaussians to fit the area around the E_1 transition. Only the Gaussians fit at E_1 transitions are shown under each absorption curve. 115
- A.7 **a)** Full width at the half maximum (FWHM) of the single Gaussian fit for the E_1 transition versus the energy peak (eV). The FWHM increases as the location of the E_1 peak increases in energy (with decreasing QD diameter) until it reaches a maximum at 2.48eV (2.3nm diameter) and then begins decreasing at 2.51eV (1.9nm diameter). **b)** The y-axis is proportional to the oscillator strength (f_{if}) of the E_1 transition and the x-axis is the energy peak (eV) of the transition. Blue diamonds represent f_{if} for the single Gaussian fit to the E_1 transition while red squares are the sum of f_{if} for the fit with two Gaussians at the E_1 transition. The E_1 peak energy for the two Gaussian fit is taken to be the average of the two peak energies. The oscillator strengths the different fits follow the same trend although the peak energies do not agree exactly. 116

Chapter 1

Introduction

1.1 Photovoltaic Background

The majority of photovoltaics (PVs) on the market today are considered ‘first generation’ and are single-junction silicon devices with market energy efficiencies around 15-20%. [1] Unfortunately, first generation devices suffer from at least four losses in efficiency: 1) inability to absorb photons with energy less than the band gap; 2) phonon-cooling of electrons and holes with excess energy above the band gap; 3) radiative recombination of electrons and holes; and 4) trap-assisted recombination of electrons and holes.

Second generation devices are based on thin film designs and provide similar or even lower cell efficiencies than those of the first generation, the highest laboratory efficiencies being 20% using silicon and 29% with gallium arsenide [2]; however, the lower material and manufacturing costs associated with thin films on glass compared to that of first generation silicon wafers can provide lower cost for comparable power [1] even though these devices suffer from the same efficiency losses listed above.

Both generations of PV devices are restricted by the Shockley-Queisser (S-Q) limit of a maximum efficiency of 33% for the conversion of unconcentrated solar irradiance into electrical free energy. In 1961, Shockley and Queisser used detailed balance to calculate this upper limit, which assumes, for a defect-free bulk semiconductor, that radiative recombination is the only route for the loss of charge carriers, that only one electron-hole pair is produced per photon, and that excited electrons cool to the band edge via electron-phonon scattering. [3]

A later calculation by Ross and Nozik overcomes the S-Q limit by assuming excess photon energy is converted into electrical free energy rather than lost to cooling processes, producing a maximum efficiency of 66%. [4] In this instance solar photon conversion is increased via increased photovoltage if carriers can be extracted before the excess kinetic energy is dissipated. [5]

Another route to increased conversion efficiency is via increased photocurrent, producing two or more electron-hole pairs per single high energy photon. [6, 7] Hanna and Nozik extended the detailed balance analysis of Shockley and Queisser to allow for carrier multiplication, which raises the maximum efficiency from 33% to 44%. [8]

These two latter calculations form the basis for some third generation PV designs. Third generation photovoltaics, also referred to as next generation PVs, aim to correct one or more of the efficiency losses found in first and second generation devices, providing much higher cost efficiency. Next generation approaches to achieve this include utilizing intermediate band (IB) cells, hot-carriers, multiple exciton generation (MEG), and spectrum conversion. [9]

Many of these approaches use quantum dots in their design. In the case of MEG, it is theorized that these quantum confined, semiconductor nanocrystals increase photocurrent more efficiently than their bulk counterparts; however, many of the experiments that reported increased efficiencies do not account for the photocharging of stationary samples [10,11] and the wavelength dependence of the absorption cross-section when pumping and probing at different energies [12]. My thesis focuses on understanding the fundamental carrier dynamics in as-synthesized and ligand-exchanged lead sulfide quantum dot samples, both in colloids and in arrays, while avoiding these known errors.

1.2 Lead Chalcogenides

The IV-VI lead chalcogenide semiconductor quantum dots have received much of the attention for harnessing carrier multiplication and applications in third generation photovoltaics. Although lead selenide is more widely investigated, lead sulfide was recently used in the construction of a quantum dot solar cell with the highest certified power conversion yet, 7% [13] and is the material

I chose for my studies, in part, due to its greater stability when exposed to atmosphere [14, 15].

Bulk lead chalcogenides include PbS, PbSe, and PbTe, which all have rock-salt cubic lattice structure and similar conduction and valence band curvature, generating electrons and holes with nearly equal effective masses [16]. In addition, PbS and PbSe have large Bohr exciton radii (a_B), 18 nm and 46 nm respectively. In bulk, the exciton Bohr radius is the closest distance at which an electron-hole pair can exist in a bound state, defined by

$$a_B = \frac{4\pi\epsilon\epsilon_0\hbar^2}{\mu e^2} \quad (1.1)$$

with

$$\mu = \frac{m_e m_h}{m_e + m_h} \quad (1.2)$$

where ϵ is the dielectric constant, μ defines the exciton reduced mass, and m_e and m_h are again the effective masses of the electron and hole.

The nanocrystal radius must be smaller than a_B for quantum confinement effects to occur, which is what makes it a ‘quantum dot’, but equally important, the individual electron and hole Bohr radii (a_e and a_h , respectively) must be confined by the size of the dot. a_e and a_h can be defined using equation 1.1 listed above, replacing μ with m_e or m_h . [17]

In PbS, $a_e = a_h = 9$ nm allowing different sizes of dots that experience strong confinement effects to be synthesized, whereas other semiconductors may have a much smaller Bohr exciton radius or electron/hole Bohr radius. A small Bohr exciton radius, such as $a_B = 6$ nm in CdSe, allows a more limited range of sizes with strong confinement. A semiconductor with a small electron or hole Bohr radius, such as InSb which has $a_B = 54$ nm but $a_h = 2$ nm, presents a similar problem. [18]

1.3 Bulk Semiconductors vs Quantum Dots

1.3.1 Bulk

Electronic energy levels in bulk semiconductors are spaced so closely together that they approximately form continuous bands. At thermal equilibrium and without photoexcitation, the highest occupied band, the valence band (VB), is normally full while the conduction band (CB) is normally empty. The valence band contains the equilibrium population, forcing a carrier (electron or hole) to energetically overcome the band gap, E_g , in order to be promoted to the conduction band.

The absorption of a photon with energy greater than the band gap excites an electron from a valence band to a conduction band, leaving behind a hole in the valence band. The excess kinetic energy is then imparted to these carriers. If the carrier does not equilibrate with its environment, maintaining the excess electronic energy in a non-equilibrium state with the lattice, it is considered a ‘hot’ electron or hole. A hot carrier then either dissipates its excess energy via phonon cooling in order to relax back down to the band edge or undergoes impact ionization (II), transferring its excess energy to promote another carrier, depicted in Figure 1.1.

Ideally, impact ionization occurs when a photon with as little as $2E_g$ is absorbed; but in reality, energy many times the band gap is required for II to occur in bulk semiconductors, making it inefficient until photon energies are in the ultraviolet region of the solar spectrum. The larger energy requirement is partly because the carriers, electron and hole, are uncoupled and act independently in II. Assuming parabolic bands with $m_e = m_h$ (m_e and m_h represent the effective masses of the electron and hole respectively), the analysis of Anderson and Crowell [19], which is based on conservation of energy and crystal momentum, indicates that the electron or hole must have $\frac{3}{2}E_g$ excess energy. When absorbing a photon, excess energy is partitioned equally between the electron and hole with equal effective masses, so the photon energy threshold for impact ionization is

$$\frac{3}{2}E_g + E_g + \frac{3}{2}E_g = 4E_g \quad (1.3)$$

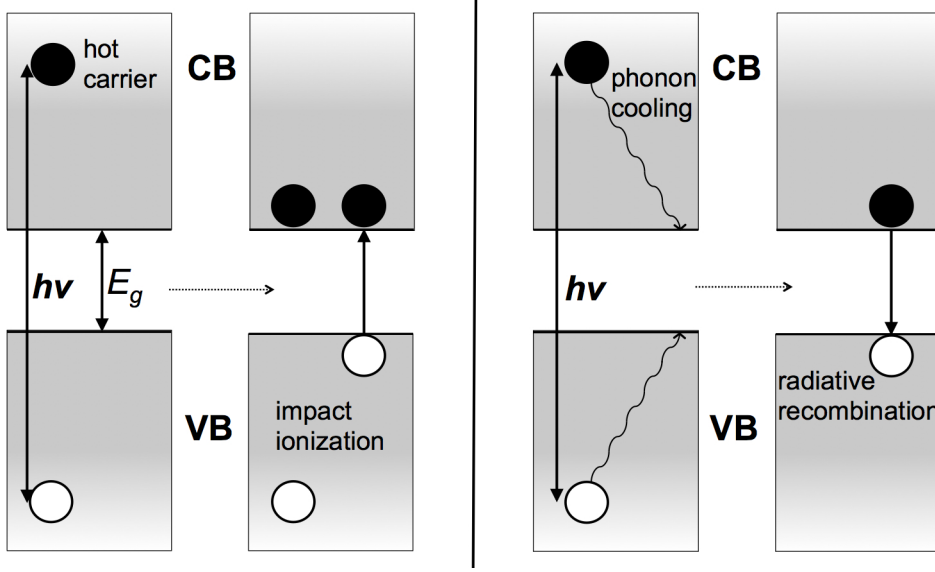


Figure 1.1: Absorption of a high energy photon excites an electron (black) from the valence band (VB) to the conduction band (CB), leaving behind a positively-charged hole (white). Excess energy absorbed in the bulk results in either the production of multiple electron-hole pairs through impact ionization or energy lost through phonon cooling before radiative recombination of the remaining electron and hole.

in such a bulk semiconductor. Similar analysis by Wolff [20] finds a threshold of $4E_g$ while Beattie and Landsberg [21] report $\frac{4}{3}E_g$ excess energy per carrier when $m_e = m_h$. For the case of bulk lead sulfide, where the effective mass of the electron and hole are approximately equal, this theoretical threshold is still less than those reported experimentally. [22] In addition to the large amount of energy required by conservation laws, phonon-carrier cooling occurs very quickly, in less than a picosecond, competing with the II process and further lessening its likelihood.

1.3.2 Quantum Dots

An electron-hole pair in a nanocrystal is spatially confined in three dimensions and can undergo very strong quantum confinement if the size of the crystal is smaller than its exciton Bohr radius, described in Section 1.2.

In quantum dots, these bound electron-hole pairs, or excitons, experience greatly enhanced Coulombic attraction due to their spatial proximity. The strong quantum confinement gives rise to the term quantum dot and creates discrete electronic energy levels within the valence and

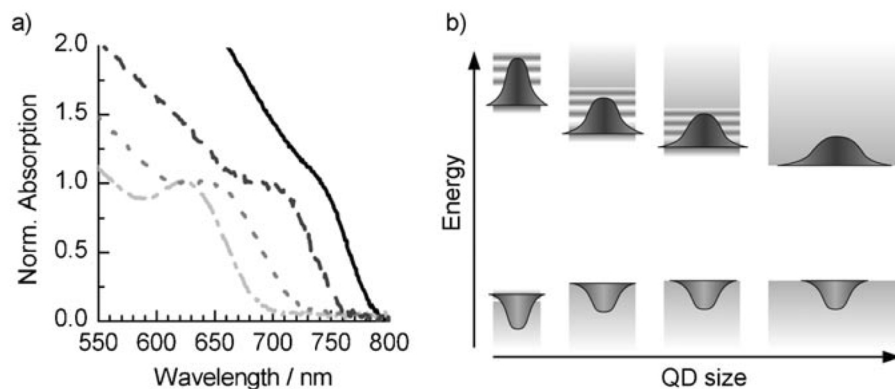


Figure 1.2: **a)** Optical absorption spectra showing the first absorption peak of colloidal CdTe quantum dots, increasing in diameter with increasing wavelength, and **b)** a representation of the quantization and increase in band gap with decreasing semiconductor size, including differences in wave function and confinement of the electron (top) and hole (bottom) due to their different effective masses. Reprinted with permission from Rühle, et al. Quantum-dot-sensitized solar cells. *ChemPhysChem*. Copyright 2010 Wiley-VCH. [23]

conduction bands, rather than the continuum of each band found in bulk, creating a 3-D particle-in-a-box atmosphere.

The confinement also acts to ‘tune’ the band gap to smaller or larger energies based on the semiconductor material and the size of the nanocrystal; as the size of the particle decreases, more energy is required for an electron to be excited from the VB to the CB. An example of this is shown in Figure 1.2 [23] for different sizes of cadmium telluride quantum dots. The first absorption peak represents the first optical transition, excitation from the highest level of the valence band to the lowest level of the conduction band, and approximately corresponds to the band gap of the quantum dot.

Figure 1.2 b) illustrates the effect of $a_e \neq a_h$ on the electronic energy levels and wavefunctions for cadmium telluride. The smaller effective mass of the electron is reflected in the larger spatial spread of the electron wavefunction as well as discrete energy levels associated with electron confinement at larger particle sizes than hole confinement. [23]

Boudreaux, et al.’s 1980 paper predicted an increase in carrier relaxation times in quantized structures due to multi-phonon relaxation requirements from increased intraband spacing. A the-

oretical increase in efficiency of carrier multiplication (CM) in QDs, often called multiple exciton generation (MEG), over bulk was attributed to this ‘phonon bottleneck’ which allowed CM to compete with electron-phonon cooling. [24] However, even achieving a bottleneck for relaxation from the second exciton level to the first exciton level requires significant surface engineering. [25]

1.4 Ultrafast Experiments

In 2004 researchers reported multiple electron-hole pair signatures that persisted at low laser intensity in ultrafast experiments on lead selenide quantum dots. [10] This was attributed to highly efficient carrier multiplication from a single photon. It is hypothesized that an increase in CM efficiency in quantum dots over bulk can be attributed to the relaxation of conservation of crystal momentum, which lowers the threshold energy necessary for CM.

Soon after the 2004 study by Schaller and Klimov, experiments on other semiconductor quantum dots, such as PbS [26], CdSe [27], and Si [28], reported similar persistent signals attributed to efficient production of multiple electron-hole pairs from one photon. But others have reported lower carrier multiplication yields [29, 30] and offered arguments against more efficient CM in quantum dots compared to bulk [22], which has led to controversy over the topic. Work addressing these differences has shown that some of the early experiments led to over-estimates of the CM efficiency, which is discussed below.

1.4.1 Poisson Assumptions

Electron-hole pair creation follows Poisson statistics in bulk semiconductors and it is assumed that at initial times, before recombination, quantum dots will also follow the Poisson distribution:

$$P_k = \frac{\langle N_0 \rangle^k}{k!} e^{-\langle N_0 \rangle} \quad (1.4)$$

where P_k describes the fraction of dots with k excitons. $\langle N_0 \rangle$ is the average number of photons absorbed per quantum dot and is the product of the absorption cross-section at the excitation wavelength, $\sigma(\lambda)$, and the density of incident photons per sample area at a given point in the

sample, or fluence j , $\langle N_0 \rangle = \sigma(\lambda) \cdot j$. Allowing this assumption in nanocrystals suggests that absorption occurs via independent carriers rather than excitons; it should be noted that the bulk-like assumption of Poisson behavior is inconsistent with the expectation of strongly coupled excitons due to spatial confinement. [31] At wavelengths well above the bandgap, excitation events may be described randomly due to the bulk background observed in linear absorption spectra, but at lower wavelengths where stronger confinement is present (i.e., near the bandgap) this randomized approach may not be valid, especially at high $\langle N_0 \rangle$.

Efforts have been made to find a model that accurately describes the multiexciton decay dynamics of individual dots using bulk-like [32, 33] and statistical [33, 34] approaches, but each approach has weaknesses. For example, a bulk approach is assumed to be valid for ultrafast experiments pump at high energies where the QD is believed to behave like bulk, but the probe is commonly tuned to the band gap where the 8-fold degeneracy of lead chalcogenides is still much too low to assure that Poissonian assumptions apply at higher $\langle N_0 \rangle$.

1.4.2 Quantum Efficiency

In order to quantify pump-probe results into efficiencies of multiple electron-hole pair production, signal amplitudes with excitation above and well below the energetic threshold for a particular material are compared. [10] Since non-radiative Auger recombination takes place on a much faster timescale than radiative decay, the signal at very long times is assumed to reflect the decay of a single electron-hole pair while early times are associated with the decay of multiple electron-hole pairs.

Multiple electron-hole pairs per quantum dot can be produced either via multiple photon absorption or via carrier multiplication after single photon absorption. In order to distinguish between the two events using ultrafast spectroscopic techniques, photon energy and laser fluence, or incident photons per sample area, are important parameters. Figure 1.3 is a representation of traces obtained in a transient absorption (TA) experiment using low fluence for photon energy in, below, and above the energetic threshold for CM.

The signal generated at low fluence with energy less than the threshold (green trace in Figure 1.3) remains fairly constant and reflects long decay times corresponding to the rate of single electron-hole recombination. For example, the energetic threshold for PbSe QDs to undergo MEG is approximately $3E_g$ [10], meaning that a single absorbed photon with less than this energy will not produce multiple electron-hole pairs; however, if the low energy is maintained but the fluence is raised to ensure multiple photons are absorbed by a single quantum dot then multiple electron-hole pairs can be created at this energy.

In this latter instance, the shape of the signal when scaled to the same value at long times will resemble the blue trace in Figure 1.3. The large amplitude at early times reflects the multiple electron-hole pairs compared to the lower amplitude at later times which matches temporal dynamics of the single electron-hole pair decay of the light green trace.

With this in mind, MEG experiments excite quantum dot samples with photon energy above the threshold but at fluences that should only allow, at most, absorption of one photon per quantum dot. Then, the signal at short times is compared to that at long times and the number of electron-

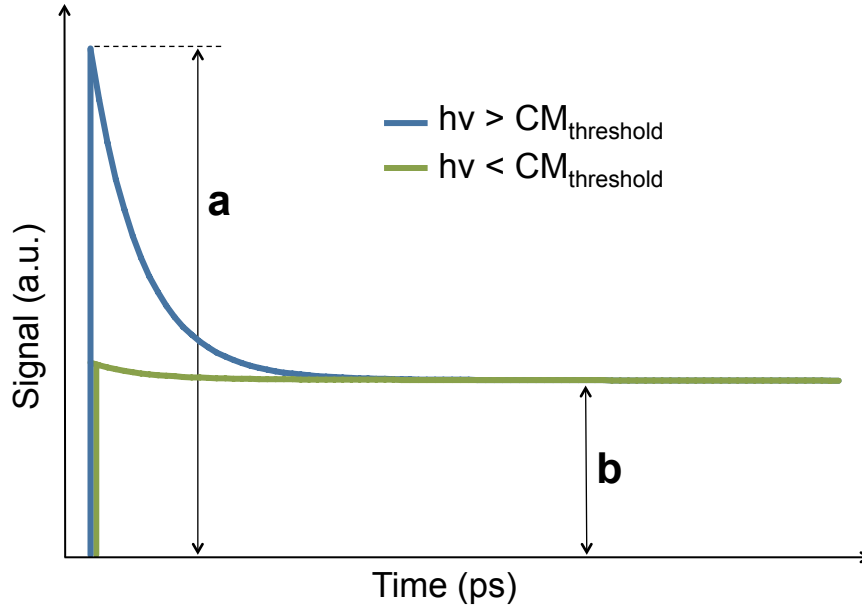


Figure 1.3: Representation of a typical trace found with TA when exciting above the CM threshold (blue) and below the CM threshold (green), both with low pump fluence. a and b are used to extrapolate quantum yield, as described in the text.

hole pairs is extrapolated. Referring back to the PbSe example, if the photon energy is at least $3E_g$ then CM should be measured with very low fluence, when the probability of absorbing a photon is very low so that at most one photon is absorbed per quantum dot, and should resemble the blue trace in Figure 1.3.

The ratio of signals at early and late times (a/b) is assumed to represent the quantum efficiency (QE), or yield, in transient absorption experiments. QE refers to the average number of electron-hole pairs produced per absorbed photon [10] and is discussed further in the following section. In some experiments, b is measured just after zero pump-probe delay for low fluence transients below the CM threshold.

1.4.2.1 Quantum Yield Arguments

A question of whether the quantum yield should be plotted against the photon energy, ($h\nu$), or photon energy per quantum dot band gap, ($h\nu/E_g$), is part of the previously mentioned controversy surrounding MEG efficiency in quantum dots versus bulk materials. Some [30, 35] stress the importance of comparing the quantum yield to the incoming photon energy per quantum dot band gap, or reduced photon energy, in order to assess the efficiency of nanocrystals of different sizes and semiconductor materials. The yield versus ($h\nu/E_g$) comparison, shown in Figure 1.4 a), demonstrates the ability of quantum dots to undergo MEG with a smaller percentage of their band gap energy than that required by bulk, reflecting an increase in efficiency.

Others [29, 36] view the important quantity to be the photon energy needed to produce multiple carriers regardless of band gap, and therefore size, since this value determines if a device will undergo CM under solar illumination and potentially make an efficient PV (shown in Figure 1.4 b). While Nair, et al. agree that MEG in quantum dots can potentially provide more energy for PVs simply due to the higher energy of their band gap, they dispute the increase in efficiency that has been claimed by others. In addition, they assert that differences in the underlying photophysics of quantum dots versus bulk materials are best evaluated through quantum yield vs ($h\nu$).

Figure 1.4 [30] demonstrates the different trends observed by analyzing the quantum efficiency

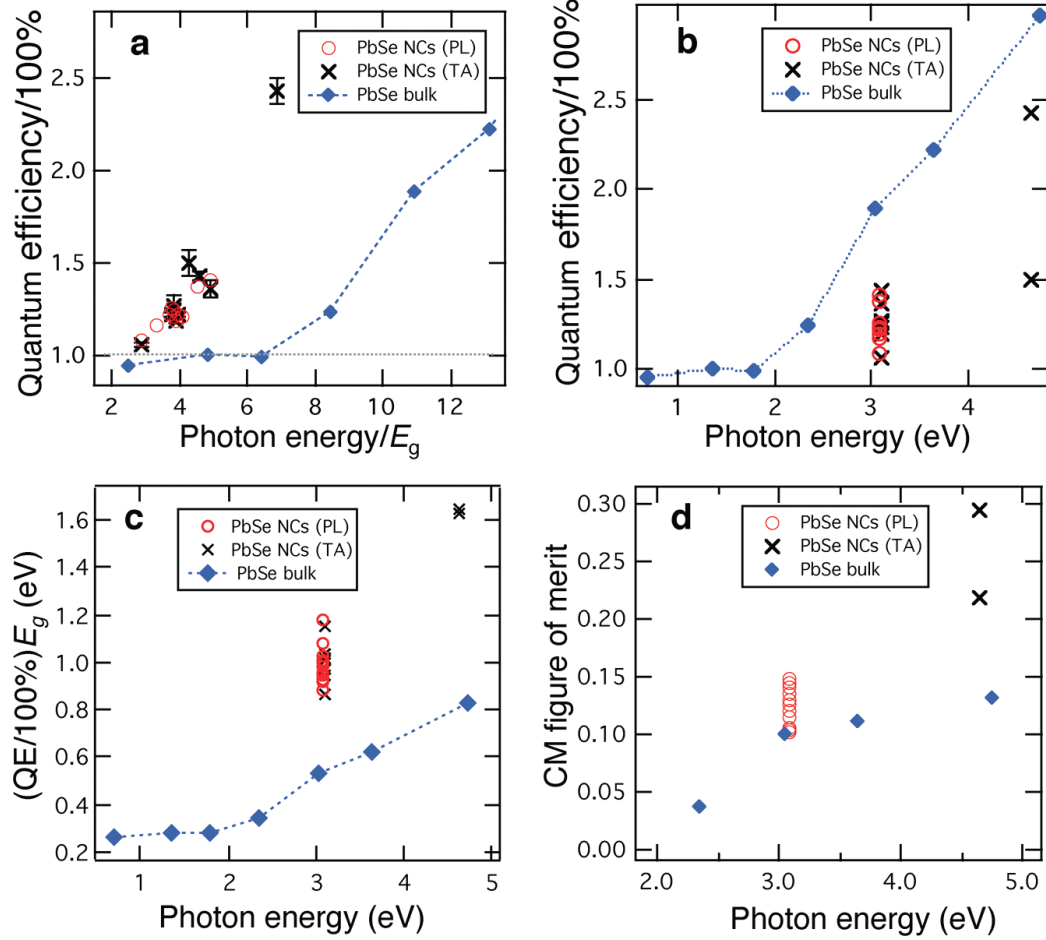


Figure 1.4: In each panel, the circles represent data obtained from time-resolved photoluminescence (TRPL), the crosses are from transient absorption (TA) data, and the diamonds are bulk values that the authors extrapolated from reference [22]. **a)** denotes an increase in quantum efficiency of quantum dots over bulk when evaluated against the normalized photon energy while **b)** shows bulk PbSe to be more efficient when absolute photon energy is considered. **c)** and **d)** further evaluate different perspectives by maintaining the absolute photon energy in the x-axis but using values that determine power conversion efficiency in a photovoltaic device and compare real and ideal multiexciton yields in the y-axis. Reprinted with permission from McGuire, et al. Apparent versus true carrier multiplication yields in semiconductor nanocrystals *Nano Letters*. Copyright 2010 American Chemical Society. [30]

versus (a) $(h\nu/E_g)$ or simply (b) $(h\nu)$ as well as by changing the y-axis to reflect different ‘figures of merit’, (c) and (d). McGuire, et al. explain that from a device design perspective, the product of the quantum efficiency and band gap is necessary and appropriate to evaluate the power conversion efficiency of the resulting PV; further, a CM figure of merit, the ratio of real and ideal multiexciton

yields for absorption of a photon with energy $h\nu$, is employed in order to compare experimental results to ideal theoretical performance.

1.4.3 Photocharging and Photodegradation

Early experiments used stationary samples [10, 26], which are susceptible to photo-charging and -degradation, but more recent data has been taken with flowing [37], stirring [29], and spinning [38] colloidal samples. McGuire, et al. studied the difference in dynamics between static and stirred colloidal solutions of PbSe and found additional short time scales in static samples as well as signal increase at early times and decrease at late times. [30] The change in signal amplitude for static solutions can explain some of the previous reports of extremely high CM efficiencies [39]; nonetheless, the ratio of early to late time signals of the stirred samples exhibit some increase in CM of the PbSe quantum dots over that of bulk in McGuire's analysis.

Quantum dot arrays, or well-ordered thin films, are direct precursors to functional photovoltaic devices but challenges exist in obtaining data on refreshed arrays, which cause most such experiments to be performed on static samples. Fortunately, novel techniques have recently been developed to better deal with this dilemma, such as a low-noise, high-speed, air-free, rotating sample cell. Initial transient absorption experiments on lead selenide arrays using such a rotating cell found no difference in the decays of refreshed and static samples, but further studies are needed to confirm and expand on these results. [40]

1.5 Ligand Exchange and Film Studies

During synthesis, most quantum dots are capped with long-chain organic ligands, such as oleic acid (18-carbon chain) which attaches to the dot as oleate, for surface passivation. These ligands work well to prevent aggregation when dots are studied in colloidal form, but are too bulky and insulating when working with arrays as precursors to functional photovoltaics. Some studies look at ligand exchange, substituting shorter carbon chains and different functional groups (Figure 1.5) in place of the bulky organics, as a means of reducing dot-to-dot distance, increasing

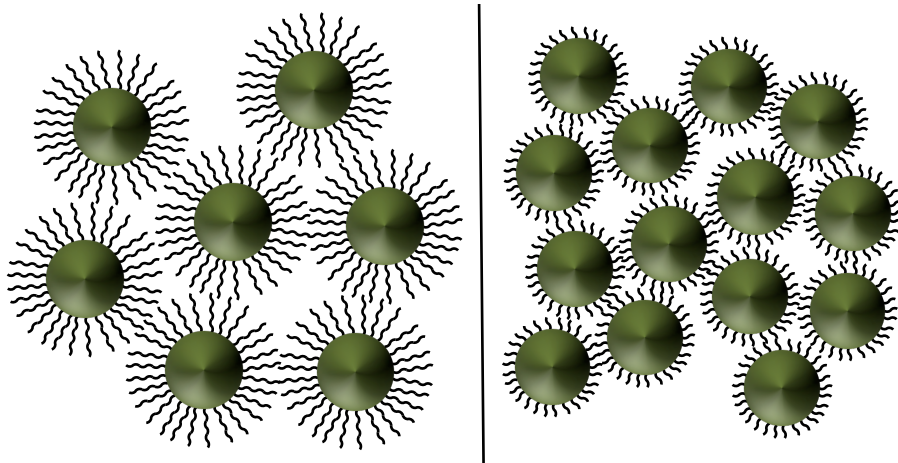


Figure 1.5: Quantum dots are passivated with long-chain organic ligands, such as oleate (left), but ligand exchanges replace these with shorter organic molecules, such as 1,2-ethanedithiol, which reduces interdot spacing (right).

interdot coupling, and better understanding how different ligands may otherwise modify carrier dynamics. [41,42]

Although it varies from ligand to ligand, a common procedure for the exchange includes coating a substrate with oleate-capped dots by spin-casting, dip-coating, or drop-casting and then dipping the substrate into a dilute solution containing the desired ligand for some period of time. The amount of time necessary varies with the new ligand; while 1,2-ethanedithiol (EDT) requires only a few minutes [43], certain amines are treated over a 24-hour period [42]. Many iterations of dipping the substrate in the oleate-capped solution followed by the shorter ligand solution may be necessary in order to achieve the necessary optical density for ultrafast studies.

Determining structural and optical changes that occur after treating arrays provides important information for spectroscopists when performing ultrafast studies. For example, Talapin and Murray observed the evolution of a red-shift in the absorption spectrum of PbSe treated with hydrazine in acetonitrile. [44] Similarly, Law, et al. replaced the oleate ligand on PbSe quantum dots with various amines and found the expected red-shift of the first absorption peak, but treatments with pure hydrazine and pure pyridine caused considerable nanocrystal growth so that the first absorption peak was not even observed on the absorption spectra out to 2500nm (Figure 1.6,

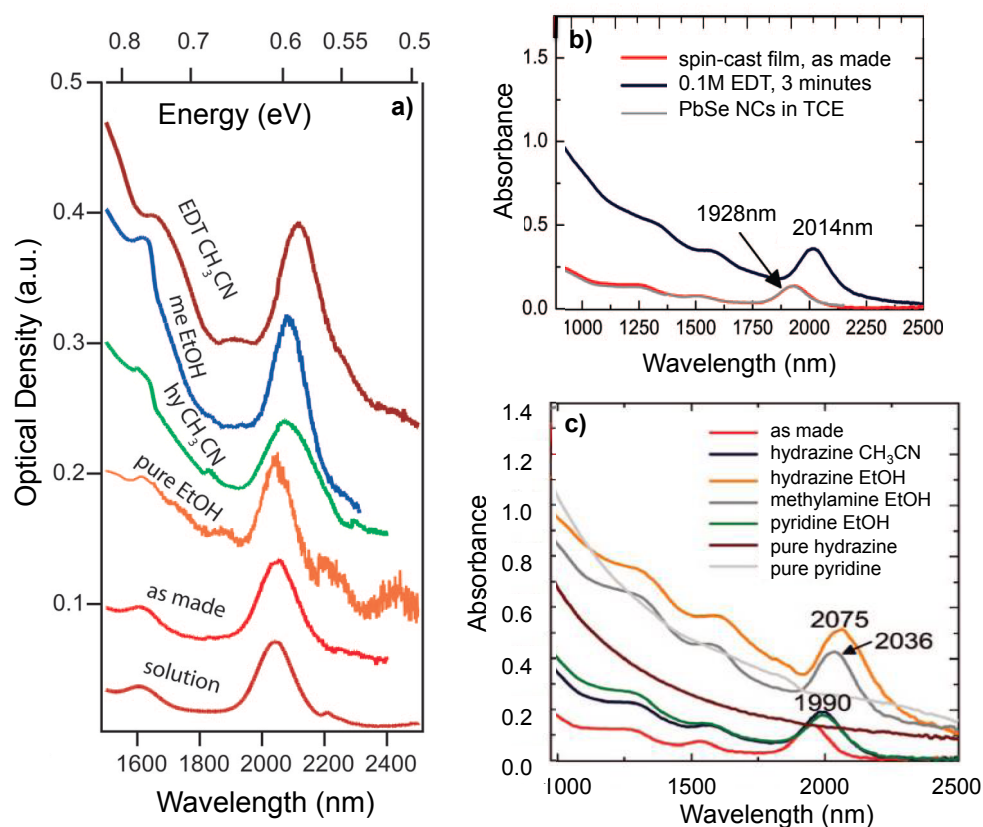


Figure 1.6: Absorption spectra of oleate-capped PbSe colloidal solutions and PbSe arrays that have undergone ligand exchange, which can lead to a red-shift and broadening of the first transition peak. Adapted with permission from **a)** Beard, et al. Variations in the quantum efficiency of multiple exciton generation for a series of chemically treated PbSe nanocrystal films. *Nano Letters*. Copyright 2009 American Chemical Society [41], **b)** Luther, et al. Structural, optical, and electrical properties of self-assembled films of PbSe nanocrystals treated with 1,2-ethanedithiol. *ACS Nano*. Copyright 2008 American Chemical Society [43], and **c)** Law, et al. Structural, Optical, and Electrical Properties of PbSe Nanocrystal Solids Treated Thermally or with Simple Amines. *Journal of the American Chemical Society*. Copyright 2008 American Chemical Society [42].

c). [42]

The red-shift of the first exciton peak consistently occurs for PbSe after ligand exchange treatment, as well as in other semiconductor quantum dots, and has been attributed to: 1) an increase in dipole-dipole interactions between neighboring dots [45]; 2) polarization effects caused by dielectric changes in the environment [46]; 3) a combination of increases in inter-dot radiative and electronic non-radiative coupling [43]; 4) sintering of properly oriented particles spaced very closely [47]; or 5) surface state coupling with electron or hole states [48].

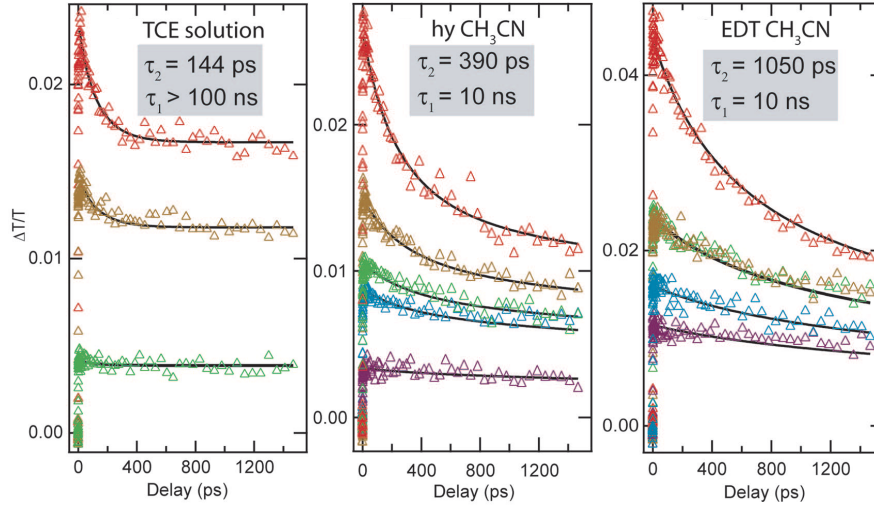


Figure 1.7: Transient absorption data of 7.4 nm diameter colloidal oleate-capped PbSe quantum dots in trichloroethylene (TCE), a PbSe array treated with hydrazine (hy) in acetonitrile (CH_3CN), and a PbSe array treated with 1,2-ethanedithiol (EDT) in CH_3CN . All were taken at increasing pump fluence but with excitation at $1.6E_g$, well below the CM threshold energy, and probed at the first exciton peak. Reprinted with permission from Beard, et al. "Variations in the quantum efficiency of multiple exciton generation for a series of chemically treated PbSe nanocrystal films". *Nano Letters*. Copyright 2009 American Chemical Society. [41]

Beard, et al. followed similar methods as those listed above to study ligand exchange but also looked at carrier multiplication efficiencies and lifetimes that different treatments produced. [41] This study built upon their previous work with 1,2-ethanedithiol [43, 49] as well as hydrazine and methylamine [11, 50] by performing exchanges on arrays of two different sizes of PbSe quantum dots (see Figure 1.6 a & b).

The data from this study is shown in Figure 1.7 and Figure 1.8 [41] and illustrates differences in the carrier dynamics between colloidal solutions and various film treatments. In most cases, the authors find a decrease in CM efficiency with the ligand exchange but an increase in Auger decay times; however, ultrafast studies alone may not absolutely predict the success of a particular ligand, such as EDT, in producing greater CM QE. Although EDT was shown to extremely reduce efficient CM in both sizes of these PbSe dots, this ligand treatment has enabled successful Schottky- [49] and hetero-junction [51] solar cells.

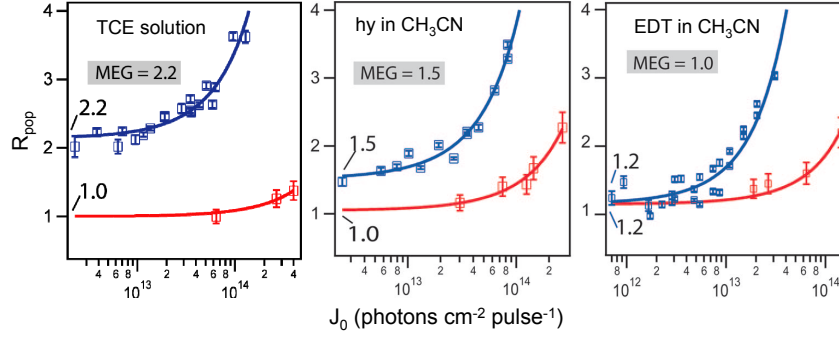


Figure 1.8: J_0 indicates the fluence and R_{pop} represents the ratio of the signal at short versus long times, or (a/b) from Figure 1.3, and is shown for excitation below and above the CM threshold. The MEG yield is reflected in the value of R_{pop} in the limit as J_0 goes to zero. The hy treated array shows a reduction in MEG compared to isolated colloidal PbSe in tetrachloroethylene while the EDT treated array indicates no MEG. Reprinted with permission from Beard, et al. "Variations in the quantum efficiency of multiple exciton generation for a series of chemically treated PbSe nanocrystal films". *Nano Letters*. Copyright 2009 American Chemical Society. [41]

1.6 Conclusions

Although a large body of work exists that addresses the potential for quantum dots, and specifically lead chalcogenides, to produce extremely efficient photovoltaics, the underlying physics that govern these processes are not completely understood. This thesis addresses some of these missing pieces through degenerate ultrafast spectroscopic studies of lead sulfide quantum dot colloidal solutions and arrays.

Chapter 2 summarizes pump-probe experiments performed at the band gap and at less than $2E_g$ of small lead sulfide quantum dots. Both solutions and arrays are investigated in an effort to compare dynamics of uncoupled solutions and films. Unlike previous studies, all solutions and films are refreshed between laser shots to minimize photocharging and photodegradation.

Chapter 3 includes degenerate pump-probe experiments of ligand-exchanged arrays and solution near the band gap. Comparison of a ligand-exchanged solution and an array made from the solution is done to observe changes in dynamics that occur with a less bulky ligand than oleate, before and after deposition.

Chapter 4 includes spectroscopic studies of different sizes of oleate-capped, lead sulfide quan-

tum dot colloidal solutions. Degenerate pump-probe experiments with time resolution below 30 femtoseconds, at varying visible wavelengths, are used to investigate high energy transitions that are seen in both quantum dots and in bulk.

Chapter 5 includes visible, degenerate pump-probe investigations of a lead sulfide solution compared to a ligand-exchanged array. The well-ordered film is compared to the oleate-capped solution with excitation at the E_1 transition to investigate differences in dynamics for this high energy transition that is observed in both bulk and quantum dots.

1.7 References

- [1] M. A. Green, Third generation photovoltaics: advanced solar energy conversion. Springer, 2003.
- [2] National Renewable Energy Laboratory, U.S.D.O.E., “Research cell efficiency records,” Apr. 2013.
- [3] W. Shockley and H. J. Queisser, “Detailed balance limit of efficiency of p-n junction solar cells,” Journal of Applied Physics, vol. 32, no. 3, pp. 510–519, 1961.
- [4] R. T. Ross and A. J. Nozik, “Efficiency of hot-carrier solar energy converters,” Journal of Applied Physics, vol. 53, no. 5, pp. 3813–3818, 1982.
- [5] D. Boudreaux, F. Williams, and A. Nozik, “Hot carrier injection at semiconductor-electrolyte junctions,” Journal of Applied Physics, vol. 51, no. 4, pp. 2158–2163, 1980.
- [6] S. Kolodinski, J. H. Werner, T. Wittchen, and H. J. Queisser, “Quantum efficiencies exceeding unity due to impact ionization in silicon solar cells,” Applied Physics Letters, vol. 63, no. 17, pp. 2405–2407, 1993.
- [7] P. Landsberg, H. Nussbaumer, and G. Willeke, “Band-band impact ionization and solar cell efficiency,” Journal of Applied Physics, vol. 74, no. 2, pp. 1451–1452, 1993.
- [8] M. Hanna and A. Nozik, “Solar conversion efficiency of photovoltaic and photoelectrolysis cells with carrier multiplication absorbers,” Journal of Applied Physics, vol. 100, no. 7, pp. 074510–074510, 2006.
- [9] O. E. Semonin, J. M. Luther, and M. C. Beard, “Quantum dots for next-generation photovoltaics,” Materials Today, vol. 15, no. 11, pp. 508–515, 2012.
- [10] R. D. Schaller and V. I. Klimov, “High efficiency carrier multiplication in PbSe nanocrystals: implications for solar energy conversion,” Physical Review Letters, vol. 92, no. 18, p. 186601, 2004.
- [11] J. M. Luther, M. C. Beard, Q. Song, M. Law, R. J. Ellingson, and A. J. Nozik, “Multiple exciton generation in films of electronically coupled PbSe quantum dots,” Nano Letters, vol. 7, no. 6, pp. 1779–1784, 2007.
- [12] R. D. Schaller, V. M. Agranovich, and V. I. Klimov, “High-efficiency carrier multiplication through direct photogeneration of multi-excitons via virtual single-exciton states,” Nature Physics, vol. 1, no. 3, pp. 189–194, 2005.
- [13] A. H. Ip, S. M. Thon, S. Hoogland, O. Voznyy, D. Zhitomirsky, R. Debnath, L. Levina, L. R. Rollny, G. H. Carey, A. Fischer, et al., “Hybrid passivated colloidal quantum dot solids,” Nature nanotechnology, vol. 7, no. 9, pp. 577–582, 2012.
- [14] J. Tang, L. Brzozowski, D. A. R. Barkhouse, X. Wang, R. Debnath, R. Wolowiec, E. Palmiano, L. Levina, A. G. Pattantyus-Abraham, D. Jamakosmanovic, et al., “Quantum dot photovoltaics in the extreme quantum confinement regime: the surface-chemical origins of exceptional air-and light-stability,” ACS Nano, vol. 4, no. 2, pp. 869–878, 2010.

- [15] M. Sykora, A. Y. Kuposov, J. A. McGuire, R. K. Schulze, O. Tretiak, J. M. Pietryga, and V. I. Klimov, "Effect of air exposure on surface properties, electronic structure, and carrier relaxation in pbse nanocrystals," ACS Nano, vol. 4, no. 4, pp. 2021–2034, 2010.
- [16] Y. I. Ravich and D. Khokhlov, "Lead chalcogenides: basic physical features," Lead Chalcogenides: Physics & Applications; Khokhlov, D., Ed.; Taylor and Francis: New York, p. 3, 2003.
- [17] A. L. Efros and A. L. Efros, "Interband absorption of light in a semiconductor sphere," Soviet Physics: Semiconductors, vol. 16, pp. 772–774, 1982.
- [18] F. W. Wise, "Lead salt quantum dots: the limit of strong quantum confinement," Accounts of Chemical Research, vol. 33, no. 11, pp. 773–780, 2000.
- [19] C. Anderson and C. Crowell, "Threshold energies for electron-hole pair production by impact ionization in semiconductors," Physical Review B, vol. 5, no. 6, p. 2267, 1972.
- [20] P. Wolff, "Theory of electron multiplication in silicon and germanium," Physical Review, vol. 95, no. 6, p. 1415, 1954.
- [21] A. Beattie and P. Landsberg, "Auger effect in semiconductors," Proceedings of the Royal Society of London. Series A. Mathematical and Physical Sciences, vol. 249, no. 1256, pp. 16–29, 1959.
- [22] J. Pijpers, R. Ulbricht, K. Tielrooij, A. Osherov, Y. Golan, C. Delerue, G. Allan, and M. Bonn, "Assessment of carrier-multiplication efficiency in bulk PbSe and PbS," Nature Physics, vol. 5, no. 11, pp. 811–814, 2009.
- [23] S. Rühle, M. Shalom, and A. Zaban, "Quantum-dot-sensitized solar cells," ChemPhysChem, vol. 11, no. 11, pp. 2290–2304, 2010.
- [24] A. J. Nozik, "Spectroscopy and hot electron relaxation dynamics in semiconductor quantum wells and quantum dots," Annual Review of Physical Chemistry, vol. 52, no. 1, pp. 193–231, 2001.
- [25] A. Pandey and P. Guyot-Sionnest, "Slow electron cooling in colloidal quantum dots," Science, vol. 322, no. 5903, pp. 929–932, 2008.
- [26] R. J. Ellingson, M. C. Beard, J. C. Johnson, P. Yu, O. I. Micic, A. J. Nozik, A. Shabaev, and A. L. Efros, "Highly efficient multiple exciton generation in colloidal PbSe and PbS quantum dots," Nano Letters, vol. 5, no. 5, pp. 865–871, 2005.
- [27] R. D. Schaller, M. A. Petruska, and V. I. Klimov, "Effect of electronic structure on carrier multiplication efficiency: Comparative study of PbSe and CdSe nanocrystals," Applied Physics Letters, vol. 87, no. 25, pp. 253102–253102, 2005.
- [28] M. C. Beard, K. P. Knutsen, P. Yu, J. M. Luther, Q. Song, W. K. Metzger, R. J. Ellingson, and A. J. Nozik, "Multiple exciton generation in colloidal silicon nanocrystals," Nano Letters, vol. 7, no. 8, pp. 2506–2512, 2007.
- [29] G. Nair, S. M. Geyer, L.-Y. Chang, and M. G. Bawendi, "Carrier multiplication yields in PbS and PbSe nanocrystals measured by transient photoluminescence," Physical Review B, vol. 78, no. 12, p. 125325, 2008.

- [30] J. A. McGuire, M. Sykora, J. Joo, J. M. Pietryga, and V. I. Klimov, "Apparent versus true carrier multiplication yields in semiconductor nanocrystals," Nano Letters, vol. 10, no. 6, pp. 2049–2057, 2010.
- [31] W. K. Peters and D. M. Jonas. personal communication, 2013.
- [32] V. Klimov, A. Mikhailovsky, D. McBranch, C. Leatherdale, and M. Bawendi, "Quantization of multiparticle auger rates in semiconductor quantum dots," Science, vol. 287, no. 5455, pp. 1011–1013, 2000.
- [33] V. Klimov, J. McGuire, R. Schaller, and V. Rupasov, "Scaling of multiexciton lifetimes in semiconductor nanocrystals," Physical Review B, vol. 77, no. 19, p. 195324, 2008.
- [34] A. Barzykin and M. Tachiya, "Stochastic models of charge carrier dynamics in semiconducting nanosystems," Journal of Physics: Condensed Matter, vol. 19, no. 6, p. 065105, 2007.
- [35] M. C. Beard, "Multiple exciton generation in semiconductor quantum dots," The Journal of Physical Chemistry Letters, vol. 2, no. 11, pp. 1282–1288, 2011.
- [36] G. Nair, L.-Y. Chang, S. M. Geyer, and M. G. Bawendi, "Perspective on the prospects of a carrier multiplication nanocrystal solar cell," Nano Letters, vol. 11, no. 5, pp. 2145–2151, 2011.
- [37] A. G. Midgett, H. W. Hillhouse, B. K. Hughes, A. J. Nozik, and M. C. Beard, "Flowing versus static conditions for measuring multiple exciton generation in PbSe quantum dots," The Journal of Physical Chemistry C, vol. 114, no. 41, pp. 17486–17500, 2010.
- [38] B. Cho, W. K. Peters, R. J. Hill, T. L. Courtney, and D. M. Jonas, "Bulk-like hot carrier dynamics in lead sulfide quantum dots," Nano Letters, vol. 10, no. 7, pp. 2498–2505, 2010.
- [39] R. D. Schaller, M. Sykora, J. M. Pietryga, and V. I. Klimov, "Seven excitons at a cost of one: redefining the limits for conversion efficiency of photons into charge carriers," Nano Letters, vol. 6, no. 3, pp. 424–429, 2006.
- [40] R. J. Hill, Enabling two-dimensional fourier transform electronic spectroscopy on quantum dots. PhD thesis, University of Colorado at Boulder, 2013.
- [41] M. C. Beard, A. G. Midgett, M. Law, O. E. Semonin, R. J. Ellingson, and A. J. Nozik, "Variations in the quantum efficiency of multiple exciton generation for a series of chemically treated PbSe nanocrystal films," Nano Letters, vol. 9, no. 2, pp. 836–845, 2009.
- [42] M. Law, J. M. Luther, Q. Song, B. K. Hughes, C. L. Perkins, and A. J. Nozik, "Structural, optical, and electrical properties of PbSe nanocrystal solids treated thermally or with simple amines," Journal of the American Chemical Society, vol. 130, no. 18, pp. 5974–5985, 2008.
- [43] J. M. Luther, M. Law, Q. Song, C. L. Perkins, M. C. Beard, and A. J. Nozik, "Structural, optical, and electrical properties of self-assembled films of PbSe nanocrystals treated with 1, 2-ethanedithiol," ACS Nano, vol. 2, no. 2, pp. 271–280, 2008.
- [44] D. V. Talapin and C. B. Murray, "PbSe nanocrystal solids for n-and p-channel thin film field-effect transistors," Science, vol. 310, no. 5745, pp. 86–89, 2005.

- [45] H. Döllefeld, H. Weller, and A. Eychmüller, “Semiconductor nanocrystal assemblies: experimental pitfalls and a simple model of particle-particle interaction,” The Journal of Physical Chemistry B, vol. 106, no. 22, pp. 5604–5608, 2002.
- [46] C. Leatherdale and M. Bawendi, “Observation of solvatochromism in CdSe colloidal quantum dots,” Physical Review B, vol. 63, no. 16, p. 165315, 2001.
- [47] P. Guyot-Sionnest, “Electrical transport in colloidal quantum dot films,” The Journal of Physical Chemistry Letters, vol. 3, no. 9, pp. 1169–1175, 2012.
- [48] P. Guyot-Sionnest, E. Lhuillier, and H. Liu, “A mirage study of CdSe colloidal quantum dot films, Urbach tail, and surface states,” The Journal of Chemical Physics, vol. 137, p. 154704, 2012.
- [49] J. M. Luther, M. Law, M. C. Beard, Q. Song, M. O. Reese, R. J. Ellingson, and A. J. Nozik, “Schottky solar cells based on colloidal nanocrystal films,” Nano Letters, vol. 8, no. 10, pp. 3488–3492, 2008.
- [50] J. E. Murphy, M. C. Beard, and A. J. Nozik, “Time-resolved photoconductivity of PbSe nanocrystal arrays,” The Journal of Physical Chemistry B, vol. 110, no. 50, pp. 25455–25461, 2006.
- [51] J. J. Choi, Y.-F. Lim, M. B. Santiago-Berrios, M. Oh, B.-R. Hyun, L. Sun, A. C. Bartnik, A. Goedhart, G. G. Malliaras, H. D. Abrua, et al., “PbSe nanocrystal excitonic solar cells,” Nano Letters, vol. 9, no. 11, pp. 3749–3755, 2009.

Chapter 2

Small Lead Sulfide Quantum Dots in Colloidal Solutions and Uncoupled Arrays

2.1 Introduction

Of the many studies done on quantum dot solutions and films using pump-probe techniques, none offer a comparative analysis of both colloidal solutions and films that are refreshed between laser shots. In addition, most studies pump with photon energy well above that of the probe. The different wavelengths of the pump and probe are attenuated differently as they propagate through the sample due to the frequency-dependence of the absorption cross-section. This frequency-dependence causes the bluer pump to be attenuated more strongly, concentrating excitation in dots near the front of the sample while the redder probe absorption is more evenly distributed throughout the length of the sample.

To address the former issue, I make use of a novel beam scanning technique developed by other Jonas group members [1] to minimize repetitive excitation by spreading excitation over a larger fraction of the sample area. The resampling times for my experiments are on the order of 100 ms, which is much longer than single exciton relaxation times (ns to μ s), reducing the effects of photo charging; however, studies show that trap states may take as long as several seconds to relax [2,3] and that such trapped carriers can reduce the time it takes for an exciton to non-radiatively recombine so that the timescale becomes comparable to that of Auger recombination. The concerns involving differences in optical density and frequency-dependent propagation in studies of multiple exciton generation (MEG) are avoided by performing degenerate ultrafast pump-probe studies, maintaining the same pump and probe wavelengths for each of the samples,

and performing experiments on solution and array samples with similar optical densities (OD).

In addition, there are only a few reports that offer a direct comparison between colloidal solutions and uncoupled films of lead chalcogenide quantum dots. [4, 5] In works by Beard et al., when pumping at energies above the band gap ($1.6E_g$ and $4E_g$) and probing at the band gap (E_g), different biexciton decay times are reported for PbSe colloidal solution compared to an uncoupled array. To investigate dynamics at the lower energies, my experiments make use of degenerate pump probe at the band edge, where others normally probe, and at $1.4E_g$, less than two times the band gap, on 2nm diameter PbS QDs. A direct comparison at $1.6E_g$ is avoided because this would be at or above the prominent, high energy E_1 transition that is seen in both bulk and in QDs.

2.2 Experimental Procedure

2.2.1 Sample Preparation

Oleate-capped lead sulfide quantum dots dispersed in hexanes were purchased from Voxtel Inc. The center of the first absorption peak of the untreated colloidal solution appears at 820nm (1.5eV), which corresponds to a diameter of 1.9nm based on sizing information provided by Voxtel Inc. Colloidal samples were stored in the glovebox and transferred to airtight quartz cuvettes (1-mm path length) for spectroscopic measurements. These quartz cuvettes were purchased from Starna Cells, Inc. and modified by the Chemistry Department glass shop where a Chem-VacTM Chem-Cap[®] sidearm valve from Chemglass Life Sciences was added (Figure shown in the Appendix). The sidearm is made of glass and the valve includes a teflon stopper with a set of three Viton O-rings that make an airtight seal against the glass, protecting the sample from exposure to atmosphere. Although the sidearm itself is not necessary in the experiments here, it allows samples to be attached to the Schlenk line and put under vacuum or inert gas, if necessary.

Anhydrous solvents ($\geq 99\%$) were purchased from Sigma-Aldrich. Hexane and octane were degassed by bubbling argon through for several hours on the Schlenk line before being transferred to the glovebox. The glovebox atmosphere remained at ≤ 0.1 ppm O_2 and H_2O after degassed

chemicals were introduced.

All thin film preparation took place in the glovebox with degassed, anhydrous solvents. Films were prepared on 1-inch (25.4mm) diameter (1mm thick) circular optical grade fused quartz substrates (purchased from Esco Optics) by drop-casting colloidal quantum dot solution (9:1 hexane:octane) onto the substrate.

Drop-casting is a simple method in which a drop of solution is dropped onto a substrate. As the solvent evaporates, QDs self-organize to produce a densely-packed array. [6] The OD of the film is controlled by the concentration of the solution. Nanocrystal packing is controlled, in part, by the choice of solvent. The hexane-octane mix allows a slower evaporation rate compared to other solvents, such as toluene, and results in locally well-ordered films. [6]

Films were allowed to dry overnight in the glovebox before sealing them in an airtight sample cell. The sample cell (shown in Figure 2.1) consists of two optical grade fused quartz substrates, separated by a $250\mu\text{m}$ thick teflon spacer. Viton O-rings on the outside of each substrate seal the sample when compressed in two directions by beveled aluminum rings as the top of the cell is screwed onto the base.

Linear absorption spectra of each sample were taken with a Varian Cary 500 UV-VIS-NIR Spectrophotometer. Spectra of the solution and array are shown in Figure 2.2. The oleate-capped solution and thin film have their first absorption peak at 820nm and 822nm, respectively. A similar small red-shift between solution and uncoupled array has been reported in other studies [4, 5] and is largely attributed to changes in polarization of the environment [7].

2.2.2 Pump-Probe Measurements

Degenerate pump-probe measurements were recorded with the pulse spectrum centered at 800nm, E_g , and at 574nm, $< 2E_g$. The sub-100fs, 800nm output of a RegA 9000 regenerative amplifier with 10kHz repetition rate was used for the band gap measurements. A $42\mu\text{m}$ spot size was determined by beam imaging at the sample location. [8] An image of beam overlap at time zero was taken with a ZoomCam USD Video Camera (640 x 480 resolution) and a 2-dimensional

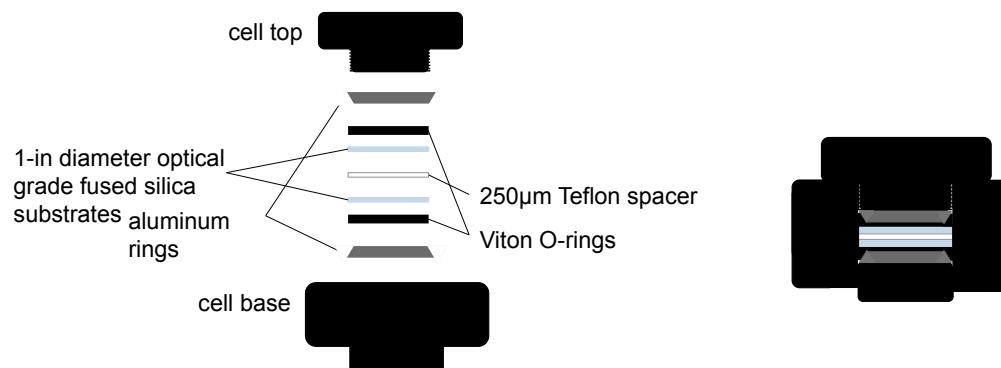


Figure 2.1: The sample is only drop-cast onto one of the substrates, which is separated from the other window by a teflon spacer. Viton o-rings are pressed against both the outside of each substrate and the inner walls of the cell base by bevelled aluminum rings as the top of the cell is screwed onto the base, sealing the cell.

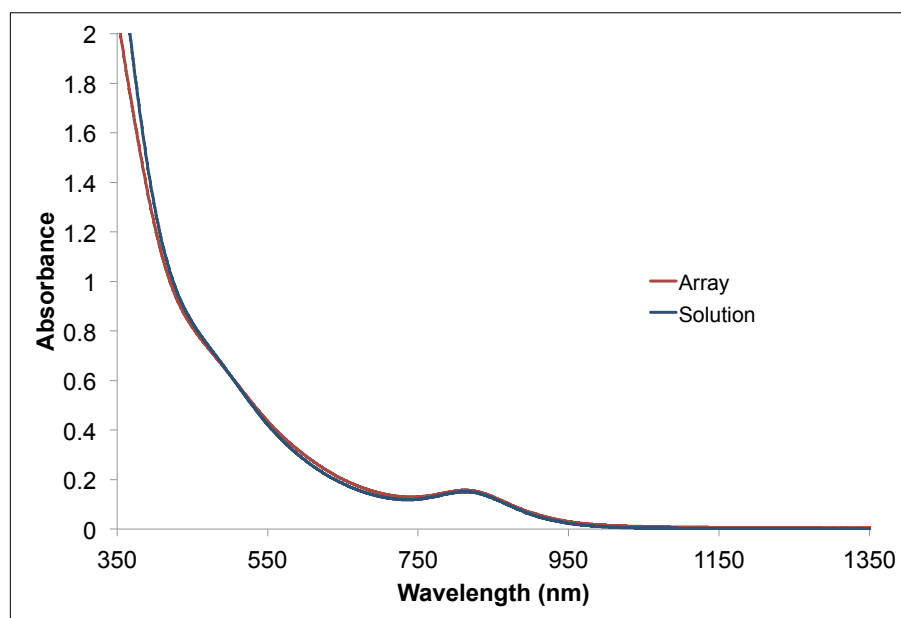


Figure 2.2: Linear absorption spectra of oleate-capped 2nm diameter PbS quantum dots in hexane and as an array. The colloidal solution is in blue [$E_g = 820nm$] and the array is in red [$E_g = 822nm$].

elliptical Gaussian profile was fit to the image. This fit determines the full-width at half-maximum (FWHM) in two dimensions, the average of which is taken to be the spot size of the beam at the sample. The average probe power was maintained around $5.5\mu\text{W}$ while the pump power was varied, in some cases from $16\mu\text{W}$ to 2.4mW , to collect data at different excitation probabilities, or average number of photons absorbed per quantum dot, denoted by $\langle N \rangle$.

For higher photon energy experiments, sub-40fs pulses were generated from a home-built, visible non-colinear optical parametric amplifier (NOPA), pumped by the RegA. The NOPA was tuned to 574nm and the beam imaging method described above determined an average beam FWHM of $58\mu\text{m}$. The lower power output of the NOPA compared to the RegA and the smaller signal size from the QDs at this wavelength (as compared to excitation near the band edge) prevented measurements with the same range of pump powers mentioned above. The probe was maintained around $5.2\mu\text{W}$ and the pump was varied between $25\mu\text{W}$ and $100\mu\text{W}$, as feasible.

The overlap of the pump and probe beam spatial profiles (dimensions of area^{-1}) is given by:

$$H = \int_0^\infty h_{\text{pu}}(r) h_{\text{pr}}(r) 2\pi r dr \quad (2.1)$$

where $h_{\text{pu}}(r)$ and $h_{\text{pr}}(r)$ are the pump and probe profiles, respectively. [8] For each beam,

$\int_0^\infty h(r) 2\pi r dr = 1$ and the intensity spatial profile is $I(r) = I_{\text{tot}} h(r)$. The total number of absorbed pump photons, P :

$$P = \rho(\nu_0)(1 - 10^{-A(\nu_0)}) \quad (2.2)$$

is found by multiplying the fraction of quantum dots that absorb at the center of the pulse spectrum, $1 - 10^{-A(\nu_0)}$, by the number of pump photons per pulse incident upon the front of the sample at the center (ν_0) of the pump frequency spectrum, $\rho(\nu)$ ($\nu_0 = c/\lambda_0$ with $\lambda_0 = 800\text{nm}$ and 574nm for the transients collected here). $A(\nu_0)$ is the frequency-dependent absorbance of the sample at the pump wavelength, taken from the linear absorption spectrum. [8] Multiplying H and P by the absorption cross-section, $\sigma(\nu_0)$ results in a probe-detected spatial average of the number of photons absorbed per QD:

$$\langle N \rangle = H \sigma P \quad (2.3)$$

2.3 Results & Discussion

2.3.1 Pump-probe at the Band Gap

Figure 2.3 shows the linear absorption spectra of the solution and film used in degenerate pump-probe experiments at the band gap. The optical densities of the solution and array at 800nm are similar, 0.13 and 0.11, respectively.

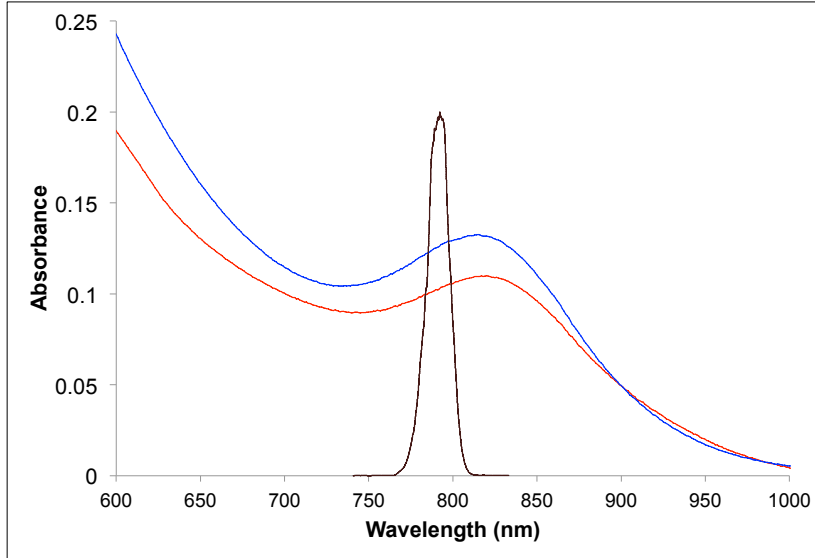


Figure 2.3: Linear absorption spectra of 2nm diameter PbS quantum dots in hexane and as an oleate-capped array. The colloidal solution is in blue [$OD(800nm) = 0.13$ and $E_g = 820nm$] and the array is in red [$OD(800nm) = 0.11$ and $E_g = 822nm$]. The pulse spectrum used for pump-probe experiments is overlaid as the dark red trace - it is roughly Gaussian with a center wavelength near 800nm.

Figures 2.4 & 2.5 illustrate the first 100ps of the raw, non-normalized transients, with multi-exponential fits overlaid in black. The data and fits are discussed in the next section. Figure 2.6 shows the transients of both the oleate-capped solution and film, divided by the respective optical density and pump power, which is proportional to energy per pump pulse, U_{pump} . Close inspection reveals that the PbS film has a consistently faster single exciton decay time (slowest decay time constant) than the solution. A similar faster single exciton decay was reported in a study of PbSe by Luther, et al. [9], in which the authors attribute the faster decay in the film to an increase in surface recombination from ligand bond-breaking during film preparation. This slowest decay is

not dependent upon excitation probability.

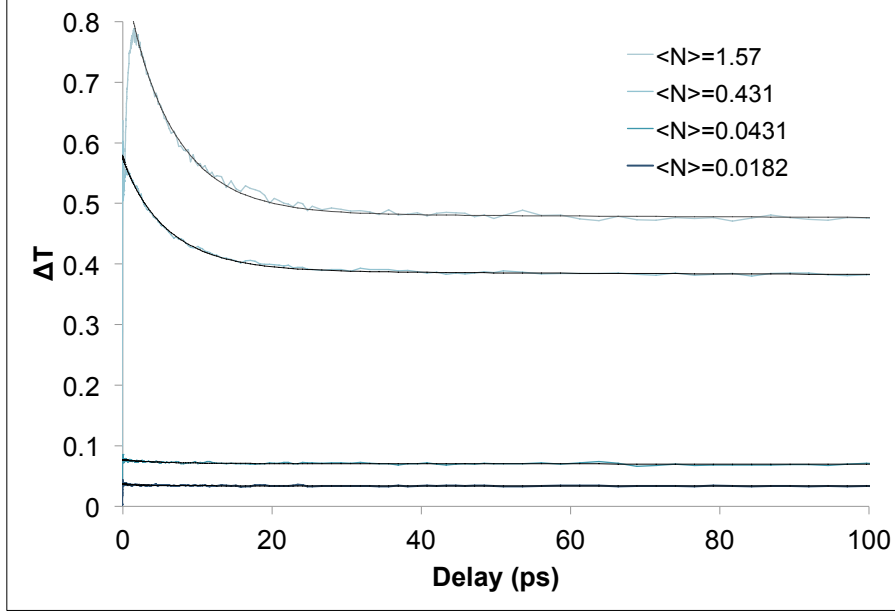


Figure 2.4: Pump-probe transients, recorded with the pulse spectrum centered at 800nm, of the 1.9nm diameter oleate-capped PbS colloidal solution. The pump-induced change in probe transmission, ΔT is on the y-axis and multi-exponential fits to each transient, which are discussed later in the text, are overlaid in black.

Figures 2.7 (film) & 2.8 (solution) show transients from Figure 2.6, which have been normalized at long times to illustrate differences in early time amplitudes with changing pump power. Experiments were repeated on a second sample of oleate-capped solution which yielded similar results and is shown in the Appendix.

2.3.1.1 Discussion

Since maintaining very low excitation probability will allow, at most, the absorption of a single photon per QD, producing one electron-hole pair per QD, then an assumption made in most literature analysis is used here: the pump-probe transients with very low excitation probability contains negligible contributions from multi-excitons and the signal is dominated by single exciton dynamics.

Most literature analysis assumes the ratio of the signal at short and long times, (a/b) taken

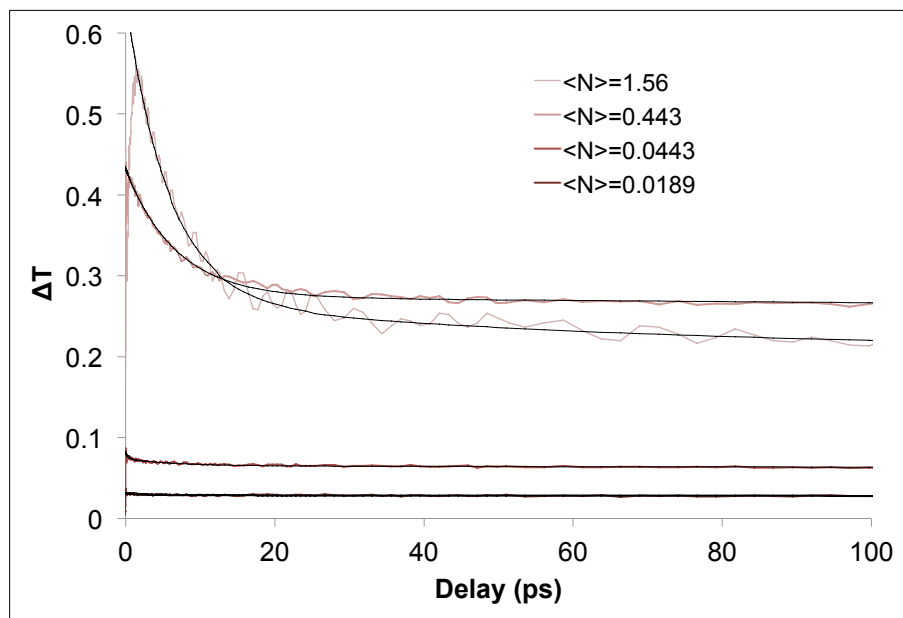


Figure 2.5: Pump-probe transients, recorded with the pulse spectrum centered at 800nm, of the 1.9nm diameter oleate-capped PbS film. The pump-induced change in probe transmission, ΔT is on the y-axis and multi-exponential fits to each transient, which are discussed later in the text, are overlaid in black.

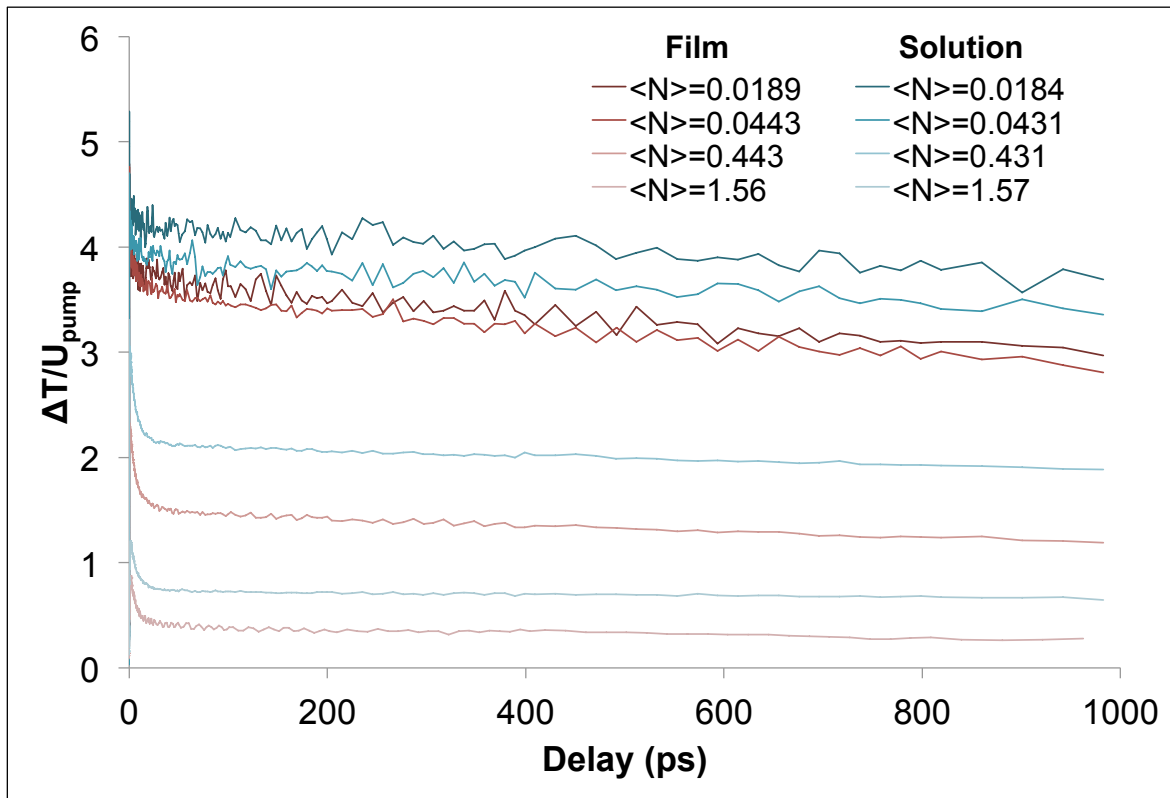


Figure 2.6: Pump-probe transients of 1.9nm diameter oleate-capped PbS in hexane (solution) and drop-cast array (film). The pump-induced change in probe transmission, ΔT , on the y-axis, is divided by the respective optical density and pump power, which is proportional to energy per pump pulse used to record each individual transient, U_{pump} . In the low excitation probability limit, $\Delta T/U_{pump}$ should not vary with U_{pump} .

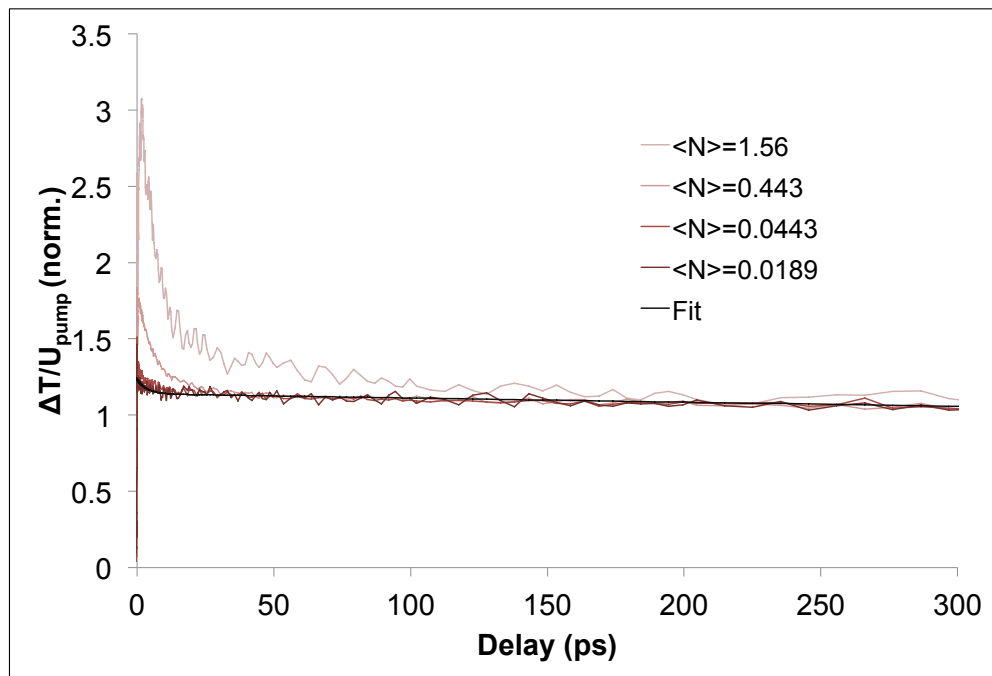


Figure 2.7: Transients for the oleate-capped film are normalized at long-times, the average amplitude between 0.5ns and 1ns, to illustrate differences in amplitude at early times, which indicates biexciton, trion, or possible multi-exciton population decay.

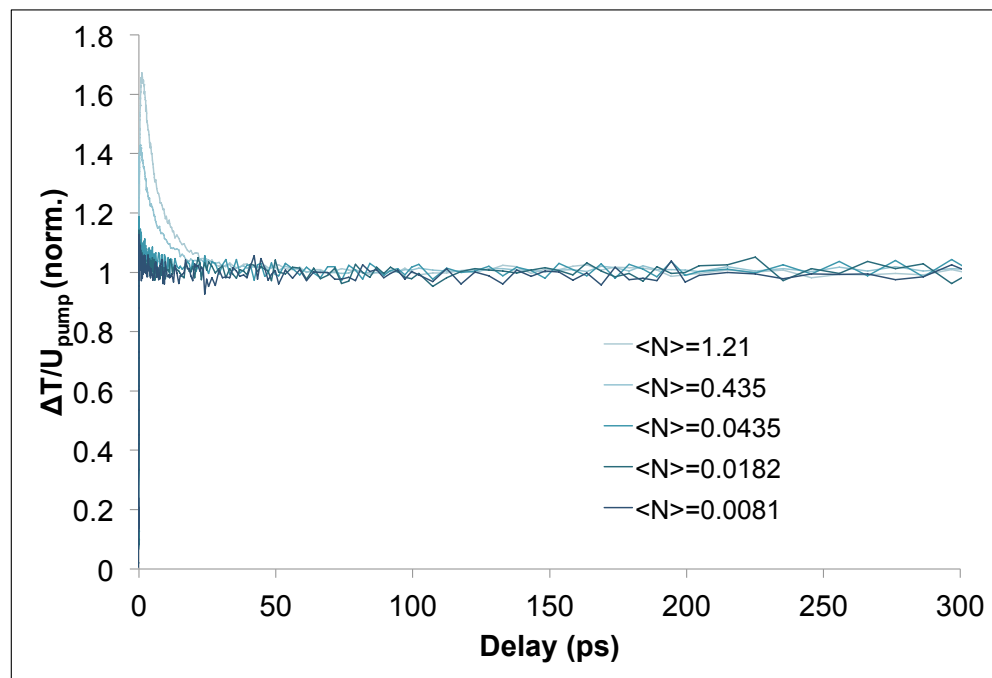


Figure 2.8: As for the film data in Figure 2.7, pump-probe transients for the oleate-capped solution are normalized at long-times, the average amplitude between 0.5ns and 1ns, to illustrate differences in amplitude at early times, indicating biexciton, trion, or possible multi-exciton population decay.

directly from transients, is equal to the average number of excitons per QD; however, additional early time dynamics are seen for $\langle N \rangle = 0.0189$ (film) and $\langle N \rangle = 0.0184$ (solution) and prompt the use of the early time amplitude for long-time normalized transients at low $\langle N \rangle$ as ‘ b ’ in the (a/b) ratio for larger $\langle N \rangle$, as depicted in Figure 2.9.

In the case of the solution transients, $(a/b) = 1.0; 1.0; 1.3;$ and 1.5 with increasing fluence. Very similar ratios are found for the second set of solution transients mentioned previously, resulting in $(a/b) = 1.0; 1.0; 1.1; 1.4;$ and 1.6 . The lowest three $\langle N \rangle$ for the array have ratios $(a/b) = 1.0; 1.1;$ and 1.4 but the film transient with $\langle N \rangle = 1.56$ produces $(a/b) = 2.4$.

In this simple analysis, assumptions are tested using Poisson statistics, where P_k is the probability of a quantum dot having k excitons:

$$P_k = \frac{\langle N \rangle^k}{k!} e^{-\langle N \rangle} \quad (2.4)$$

It should be noted that since there is spatial variation in the $\langle N \rangle$ used here, P_k is a function of position within the beam, resulting in a spatially varying probability distribution. [10] This spatial distribution can be averaged to yield the spatially averaged probability distribution, which is not Poisson.

This results in the lowest excitation probability for the solution and film having the probability of a quantum dot containing multiexcitons, $\sum_{k=2}^{\infty} P_k$, equal to 1.7×10^{-4} and 1.8×10^{-4} , respectively. The ratio:

$$\frac{\sum_{k=2}^{\infty} k P_k}{P_1} \quad (2.5)$$

is significant in approximating contamination of the signal by multiple excitons and is found to be 0.019 for both the solution and the film, less than 2% contamination at the lowest pump powers.

Next, Poisson statistics are used and compared to the experimental ratio, (a/b) . The average number of excitons *per excited dot* is calculated:

$$\langle N_{eh} \rangle = \frac{\langle N \rangle}{\sum_{k=1}^{\infty} P_k} = \frac{\langle N \rangle}{1 - P_0} = \frac{\langle N \rangle}{1 - e^{-\langle N \rangle}}. \quad (2.6)$$

Following the approach of Schaller, et al. [11], $\langle N_{eh} \rangle$ is expected to be equal to the experimental (a/b) . Plotting (a/b) versus $\langle N \rangle$ for all oleate-capped samples (two solution and one film) in

Figure 2.10 and comparing it to $\langle N_{eh} \rangle$, determined by spatially averaged Poisson statistics, shows agreement for low $\langle N \rangle$, but shows increasing deviation as $\langle N \rangle$ increases. At the band edge, Poisson statistics are expected to apply at very low $\langle N \rangle$ for lead chalcogenides because of the 8-fold degeneracy of the band gap, but once the sample is saturated, at high $\langle N \rangle$, Poisson assumptions are no longer valid.

At the lowest $\langle N \rangle$ for each sample, one exciton per excited QD is predicted by spatially averaged Poisson statistics. Prior work suggests that a single exponential should be sufficient to fit the transients and extract constants for single exciton decay, but a short-lived, small amplitude decay is present for each in the first few picoseconds and necessitates a biexponential fit, $Ae^{-t/\tau_3} + Ce^{-t/\tau_1}$. The additional short time decays have lifetimes, τ_3 , on the order of 2-3ps and at such $\langle N \rangle$, are likely a relaxation process among single exciton states rather than a multiexciton contribution. Multi-exponential fits are found for each non-normalized transient, and the coefficients and time constants for the two solution samples are listed in Table 2.1, while those found for the film are listed in Table 2.2. It should be noted that while exponential fits to each of the film transients provide a τ_2 of 6-7ps as in solution, $\langle N \rangle = 1.56$ in the film requires an additional exponential with a time constant in the tens of picoseconds, labeled as $\tau_{2'}$.

| | $\langle N \rangle$ | A | τ_3 | B | τ_2 | C | τ_1 |
|------------|---------------------|--------------------|------------------------|--------------------|------------------------|--------------------|----------------|
| Solution 1 | 0.0184 | 0.003 ± 0.0002 | $3.1 \pm 0.5\text{ps}$ | - | - | 0.034 ± 0.0001 | $> 1\text{ns}$ |
| | 0.0431 | - | - | 0.006 ± 0.0003 | $5.3 \pm 0.7\text{ps}$ | 0.071 ± 0.002 | $> 1\text{ns}$ |
| | 0.431 | 0.027 ± 0.021 | $2.6 \pm 1.3\text{ps}$ | 0.159 ± 0.022 | $6.9 \pm 0.5\text{ps}$ | 0.387 ± 0.004 | $> 1\text{ns}$ |
| | 1.57 | 0.040 ± 0.033 | 1.4 ± 1.8 | 0.375 ± 0.020 | $6.7 \pm 0.3\text{ps}$ | 0.483 ± 0.009 | $> 1\text{ns}$ |
| Solution 2 | 0.0081 | 0.001 ± 0.0002 | $1.5 \pm 0.4\text{ps}$ | - | - | 0.019 ± 0.0001 | $> 1\text{ns}$ |
| | 0.0182 | 0.003 ± 0.0003 | $1.9 \pm 0.4\text{ps}$ | - | - | 0.041 ± 0.0001 | $> 1\text{ns}$ |
| | 0.0435 | 0.006 ± 0.0015 | $0.8 \pm 0.5\text{ps}$ | 0.006 ± 0.0015 | $7.6 \pm 2.6\text{ps}$ | 0.097 ± 0.0030 | $> 1\text{ns}$ |
| | 0.435 | 0.065 ± 0.032 | $2.9 \pm 0.9\text{ps}$ | 0.155 ± 0.033 | $7.7 \pm 0.8\text{ps}$ | 0.483 ± 0.0006 | $> 1\text{ns}$ |
| | 1.21 | 0.147 ± 0.023 | $1.8 \pm 0.6\text{ps}$ | 0.442 ± 0.032 | $7.1 \pm 0.3\text{ps}$ | 0.646 ± 0.0010 | $> 1\text{ns}$ |

Table 2.1: Coefficients and decay times for the two colloidal solutions of 1.9nm diameter oleate-capped PbS in hexane based on exponential fits to non-normalized transients, recorded with a pulse spectrum centered at 800nm. A , B , and C are coefficients in the multi-exponential fits while τ_x denotes the time constant for decay, $Ae^{-t/\tau_3} + Be^{-t/\tau_2} + Ce^{-t/\tau_1}$. Dashes denote no values associated with the respective coefficient and τ .

Robel, et al. [12] report a universal *effective* AR rate constant C_A that is dependent on QD

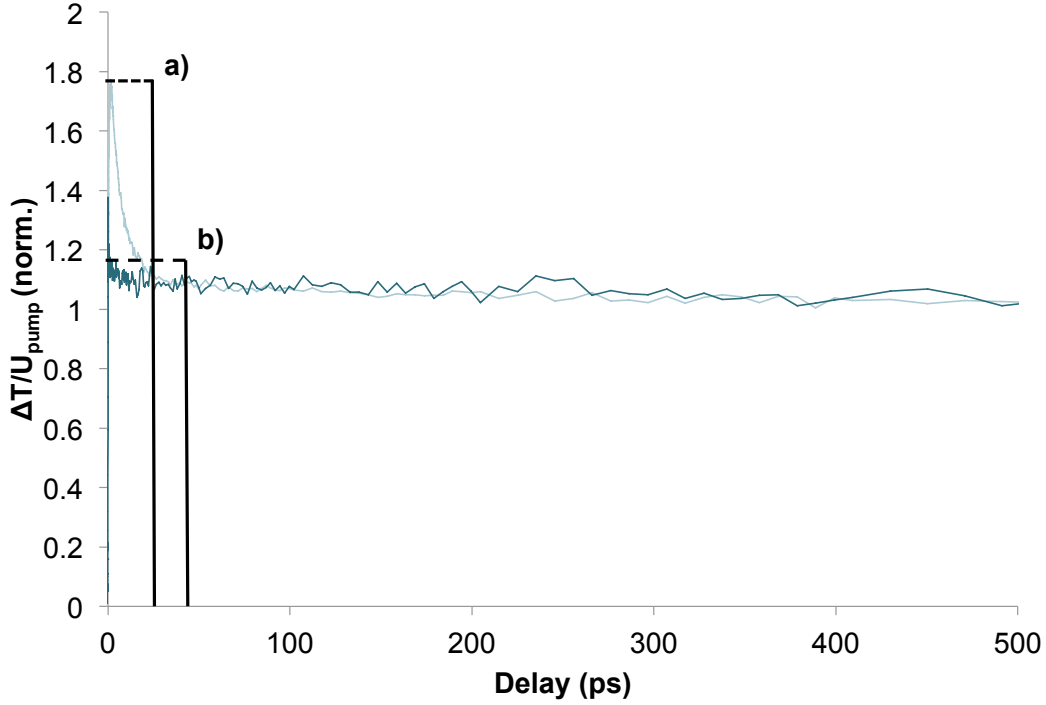


Figure 2.9: The long-time normalized transients, recorded with the center of the pulse spectrum at 800 nm, of the PbS QDs in solution with $\langle N \rangle = 1.57$ and $\langle N \rangle = 0.0184$ are shown here. **a** is the amplitude at early times when the greatest contribution from multiexcitons is present and **b** is the initial single single exciton contribution obtained from the lowest $\langle N \rangle$ transient. The ratio, **a/b** reflects the average number of excitons photoexcited per excited QD, which is 1.5 in this example.

| $\langle N \rangle$ | A | τ_3 | B | τ_2 | C | τ_2' | D | τ_1 |
|---------------------|--------------------|------------------------|-------------------|------------------------|-------------------|--------------------------|--------------------|----------------|
| 0.0189 | 0.002 ± 0.0001 | $3.6 \pm 0.6\text{ps}$ | - | - | - | - | 0.029 ± 0.0001 | $> 1\text{ns}$ |
| 0.0443 | 0.006 ± 0.002 | $0.4 \pm 0.1\text{ps}$ | 0.009 ± 0.001 | $6.7 \pm 0.6\text{ps}$ | - | - | 0.065 ± 0.0001 | $> 1\text{ns}$ |
| 0.443 | - | - | 0.158 ± 0.008 | $6.8 \pm 0.1\text{ps}$ | - | - | 0.274 ± 0.0005 | $> 1\text{ns}$ |
| 1.56 | - | - | 0.373 ± 0.008 | $6.0 \pm 0.3\text{ps}$ | 0.057 ± 0.007 | $64.0 \pm 19.4\text{ps}$ | 0.213 ± 0.0061 | $> 1\text{ns}$ |

Table 2.2: Coefficients and decay times for the array of 1.9nm diameter oleate-capped PbS QDs based on exponential fits to non-normalized transients, recorded with the pulse spectrum centered at 800nm. A , B , and C are coefficients in the multi-exponential fits while τ_x denotes the time constant for decay, $Ae^{-t/\tau_3} + Be^{-t/\tau_2} + Ce^{-t/\tau_1}$. Dashes denote no values associated with the respective coefficient and τ .

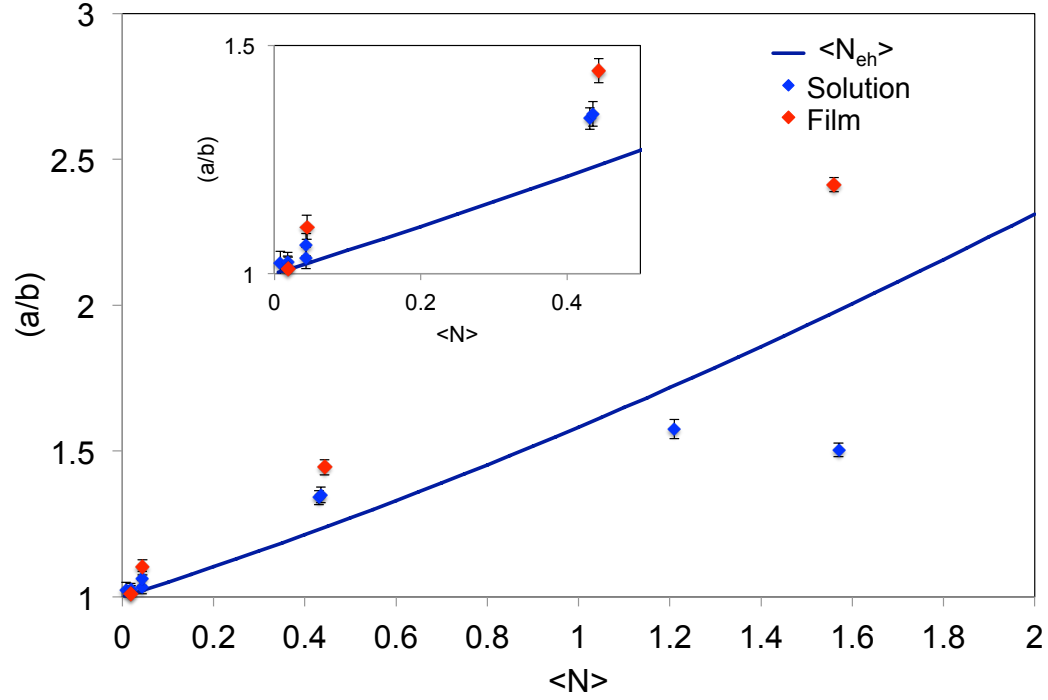


Figure 2.10: (a/b) , found from degenerate pump-probe transients recorded with the center of the pulse spectrum at 800nm, from the array (red) and the two solution samples (blue). These are compared to $\langle N_{eh} \rangle = \frac{\langle N \rangle}{1 - e^{-\langle N \rangle}}$ versus $\langle N \rangle$ (blue curve). Spatially averaged Poisson statistics apply at low $\langle N \rangle$ but are not valid once the sample is saturated at higher $\langle N \rangle$.

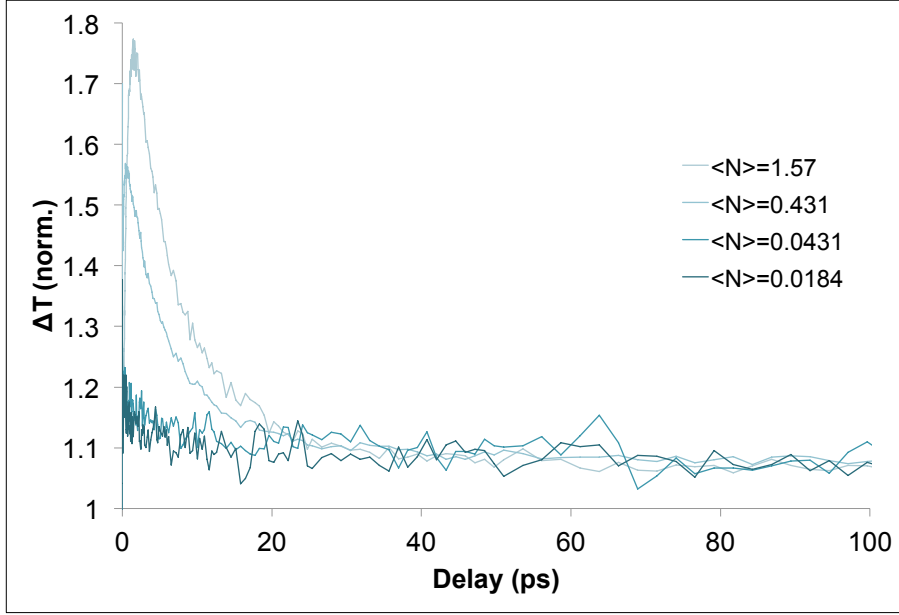


Figure 2.11: Transients of the first oleate-capped PbS colloidal solution, recorded with the center of the pulse spectrum at 800nm (shown in Figure 2.8), are normalized by their average amplitude at long-times, between 0.5 and 1ns. Assuming that the oleate-capped PbS solution transient with $\langle N \rangle = 0.0184$ includes only a single exciton decay signal, the larger amplitude at early times of transients with $\langle N \rangle = 1.57$, $\langle N \rangle = 0.431$, and $\langle N \rangle = 0.0431$ signify multi-exciton decay.

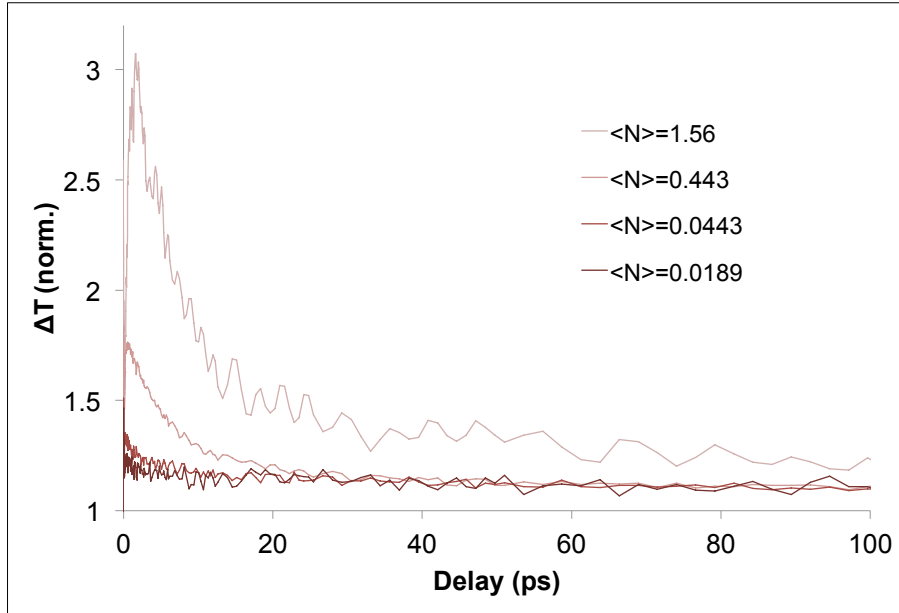


Figure 2.12: As in Figure 2.11, transients of the oleate-capped PbS array, recorded with the center of the pulse spectrum at 800nm (shown in Figure 2.7), are normalized by their average amplitude at long-times, between 0.5 and 1ns. Assuming that the PbS film transient with $\langle N \rangle = 0.0189$ includes only a single exciton decay signal, the larger amplitude at early times of transients with $\langle N \rangle = 1.56$, $\langle N \rangle = 0.443$, and $\langle N \rangle = 0.0443$ signify multi-exciton decay.

size rather than material and relates to the biexciton lifetime τ_2 as $C_A = V_0^2(8\tau_2)^{-1}$, where V_0 is the QD volume. This report suggests the biexciton lifetime for dots 2nm in diameter is between 0.5ps and 8.8ps. My data results in biexciton lifetimes, τ_2 within this suggested range, based on QD size.

One hypothesis that might explain the 64ps time constant present for the $\langle N \rangle = 1.56$ film transient is Auger recombination (AR) after excitation energy transfer (EET). The EET transfer rate would be rate limiting and determine this timescale. On this hypothesis, the sum of amplitudes for the lifetime and EET time for the QD film should be in the same proportion to the initial amplitude as the lifetime is to the initial amplitude in QD solution. This is not true for the exponential fits, but the confined EET/AR process may not have an exponential time dependence, so further consideration is warranted.

For an estimate to asses this hypothesis, I assume here that only one excitation energy transfer step is required for one exciton to find another exciton and undergo AR. Förster resonance energy transfer [13] can occur non-radiatively between closely spaced QDs via transition dipole- transition dipole coupling. A simple, initial calculation evaluates the minimum interparticle distance necessary for a transfer to occur in a colloidal solution of PbS in hexane on a 100ps timescale.

Based on Förster's article on energy migration [13] (equations 15-17') for EET, a critical separation is calculated:

$$R_0 = \sqrt[6]{\frac{3\tau_0 c J(\nu_0)}{8\pi^4 n^2 \nu_0^2}} \quad (2.7)$$

where τ_0 is the radiative lifetime, c is the speed of light (cm/s), n is the solvent refractive index, and $J(\nu_0)$ is the overlap integral (centered at frequency ν_0) taken from the experimental absorption and fluorescence spectra. This integral can be expressed in terms of cross-section, rather than molar extinction coefficient, as:

$$J(\nu_0) = \int_0^\infty \sigma_{ab}^a(\nu) \sigma_{em}^d(\nu) d\nu \quad (2.8)$$

σ_{em}^d is the emission cross-section of the donor, d . The absorption cross-section of the acceptor, a ,

σ_{ab}^a is related to the molar decadic extinction coefficient by

$$\sigma(\nu) = \ln(10)\varepsilon(\nu)\frac{1000\text{cm}^3/L}{N_A}, \quad (2.9)$$

where the units of $\sigma(\nu)$ are cm^2 , the units of $\varepsilon(\nu)$ is in $\text{Lmol}^{-1}\text{cm}^{-1}$, and N_A is Avogadro's number.

For the $J(\nu_0)$ calculation, I make use of the mirror symmetry of the absorption spectrum in the absence of the fluorescence spectrum. I calculate the overlap integral using parameters of the experimentally obtained absorption spectrum, with a mirror image reflection and a red-shift estimated from the Stoke's shift found in the literature for similarly sized PbS QDs, 0.28eV (180nm) [3], in lieu of the fluorescence spectrum. The lifetime is estimated to be 10ns based on literature values for similarly sized QDs. [4,9]

The result is a critical separation $R_0 = 5\text{nm}$ between QDs for EET, greater than the surface-to-surface distance of particles based on the length of two oleate ligands, approximately 3.6 nm. The rate of ET, and therefore the timescale, is calculated from Förster's relationship between the rate, k_{ad} , and distance:

$$k_{ad} = \frac{1}{\tau_0} \left(\frac{R_0}{R_{ad}} \right)^6 \quad (2.10)$$

where R_{ad} is the actual distance between two particles. Using the the interparticle distance of 3.6nm results in an EET timescale of $1/k_{ad} \approx 200\text{ns}$, much longer than the time constants found in any of the transients; however, calculating the interparticle distance that would result in an approximately 100ps energy transfer, shows that a distance of 1.0nm between particles would allow energy transfer to occur on the timescale found for the $\langle N \rangle = 1.56$ film transient.

A 1nm surface-to-surface separation of particles, R_{ad} , is found to produce an approximately 100ps EET between particles. Although oleic acid is 1.8nm in length, QD self-organization may allow dots in an array to be more closely spaced than the ligand length implies. Additionally, if ligand bond breaking occurs during deposition, as postulated by Luther, et al. [9], this could further decrease the distance between dots; thus, 1nm interparticle separation may be plausible, allowing EET to occur in $<100\text{ps}$, and might account for the additional time constant found for the $\langle N \rangle = 1.56$ film transient. At such small distances, we should also consider electron transfer as

the rate limiting step in an electron transfer/trion decay quenching process.

2.3.2 2nm diameter PbS at less than $2E_g$

Figure 2.13 shows linear absorption spectra of the solution and film used in degenerate pump-probe experiments at 574nm, or $1.4E_g$. The optical densities of the solution and array at 574nm are similar, 0.34 and 0.36, respectively. Figure 2.14 shows the transients of the solution and film at different $\langle N \rangle$.

Figure 2.14 shows pump-probe transients of the colloidal solution and array taken at different $\langle N \rangle$ which all include negative signals, indicative of excited state absorption (ESA). Negative signal means that contributions from ESA are greater than the total contributions from ground state bleach (GSB) and excited state emission (ESE), both of which contribute positive signal.

2.3.2.1 Discussion

Following the analysis used for pump-probe at the band gap, $\frac{\sum_{k=2}^{\infty} kP_k}{P_1}$ is determined for each transient and results in 0.036 and 0.061 for $\langle N \rangle = 0.035$ and 0.059, or approximately 3.6% and 6.1% contamination of the signal from multiexcitons. The transients with higher $\langle N \rangle$ result in 0.12 and 0.14, or about 12% and 14% contributions from multiexcitons.

Since the transients with the lower excitation probabilities here have a higher contribution from multiexcitons than the transients recorded with the pulse spectrum centered at 800nm, normalized multiples are not subtracted from transients with higher $\langle N \rangle$ as was done previously. Instead, the long time portion (50ps to 500ps) of each transient is fit before shorter time dynamics are later included. The early time constants are globally fit while holding the long time parameters constant. The fits are shown in Figures 2.15 and 2.16 and the coefficients and decay times are listed in Table 2.3.

Each transient has initial negative signal growth that maximizes around 200fs, based on initial rise lifetime (τ_3 in Table 2.3), followed by a short-time component of around 10ps and then single exciton decay slower than 1ns. The solution and array transients exhibit similar τ_2 lifetimes,

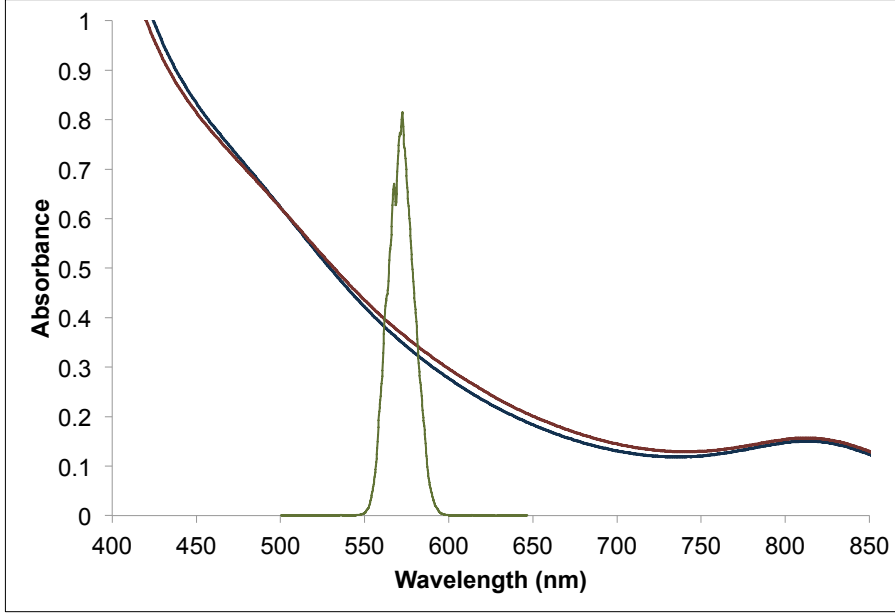


Figure 2.13: Linear absorption spectra of oleate-capped 2nm diameter PbS quantum dots in hexane and as an array. The colloidal solution is in blue [$OD(574nm) = 0.34$ and $E_g = 820nm$] and the array is in red [$OD(574nm) = 0.36$ and $E_g = 822nm$]. They have ODs of 0.15 and 0.17 at their respective E_g , 820nm and 822nm. The pulse spectrum used for pump-probe experiments is overlaid as the green trace, centered at 574nm.

| QD | $\langle N \rangle$ | A | τ_3 | B | τ_2 | C | τ_1 |
|-----------------|---------------------|------|------------------|------|-------------------|------|----------|
| <i>Solution</i> | 0.035 | 0.99 | $0.22 \pm 0.1ps$ | 0.13 | $10.6 \pm 22.8ps$ | 1.94 | $> 1ns$ |
| | 0.13 | 0.49 | $0.14 \pm 0.1ps$ | 0.10 | $19.0 \pm 5.1ps$ | 0.56 | 1ns |
| <i>Film</i> | 0.059 | 0.95 | $0.19 \pm 0.1ps$ | 0.16 | $10.9 \pm 12.4ps$ | 1.31 | $> 1ns$ |
| | 0.11 | 0.54 | $0.15 \pm 0.1ps$ | 0.13 | $9.1 \pm 7.2ps$ | 0.88 | $> 1ns$ |

Table 2.3: Coefficients and decay times for the 1.9nm diameter PbS solution and array based on exponential fits. A , B , and C are coefficients in the fit: $Ae^{-t/\tau_3} + Be^{-t/\tau_2} + Ce^{-t/\tau_1}$. All of the transients have a maximum negative signal around 200fs followed by decay to zero at less than 3ps.

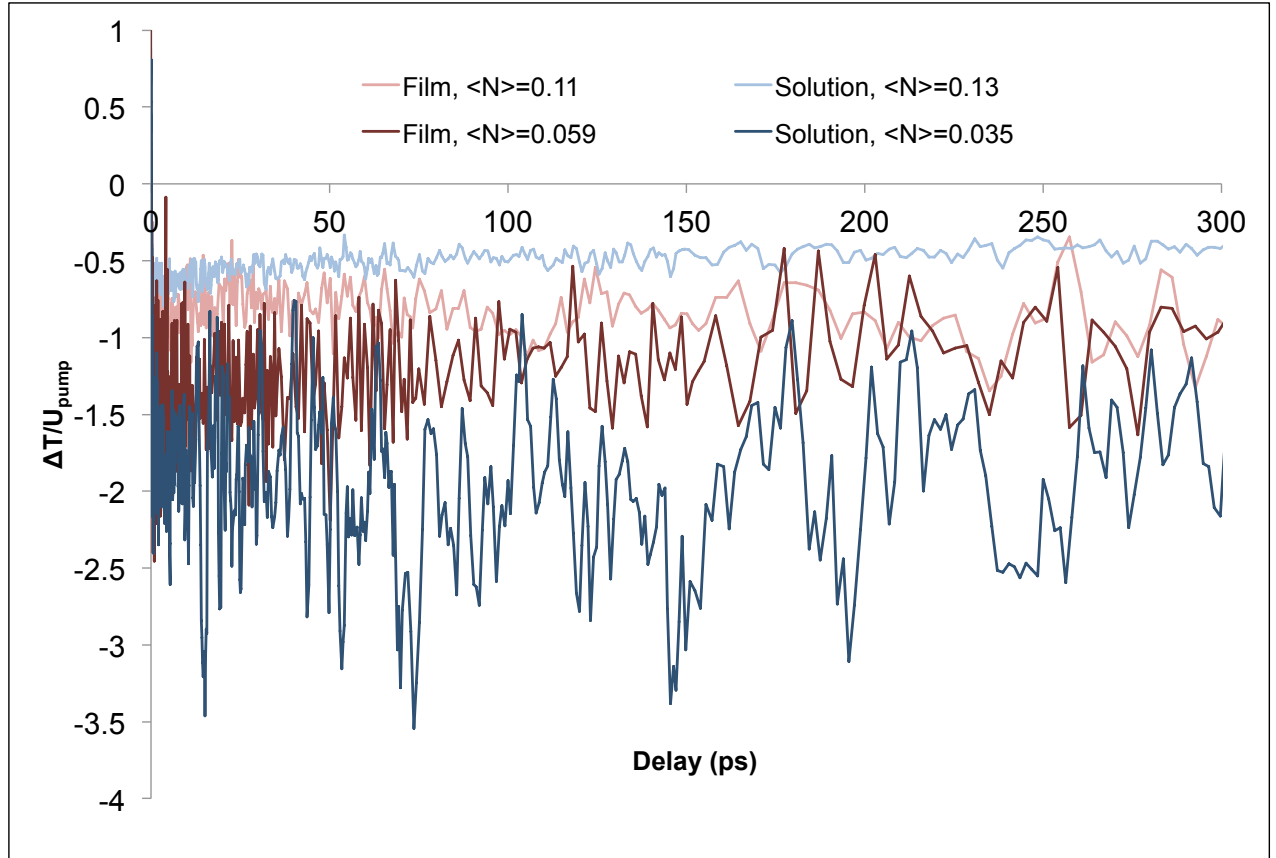


Figure 2.14: Degenerate pump-probe transients, recorded with the pulse spectrum centered at 574nm, of 2nm diameter PbS solution ($\langle N \rangle = 0.035$ and 0.13) and film ($\langle N \rangle = 0.059$ and 0.11), taken while samples were refreshed between laser shots. The pump-induced change in probe transmission, ΔT , on the y-axis, is divided by the respective pump power, which is proportional to energy per pump pulse of the individual spectrum, U_{pump} . Although there is a difference in amplitude between solution and film, the overall shape appears similar within the signal to noise.

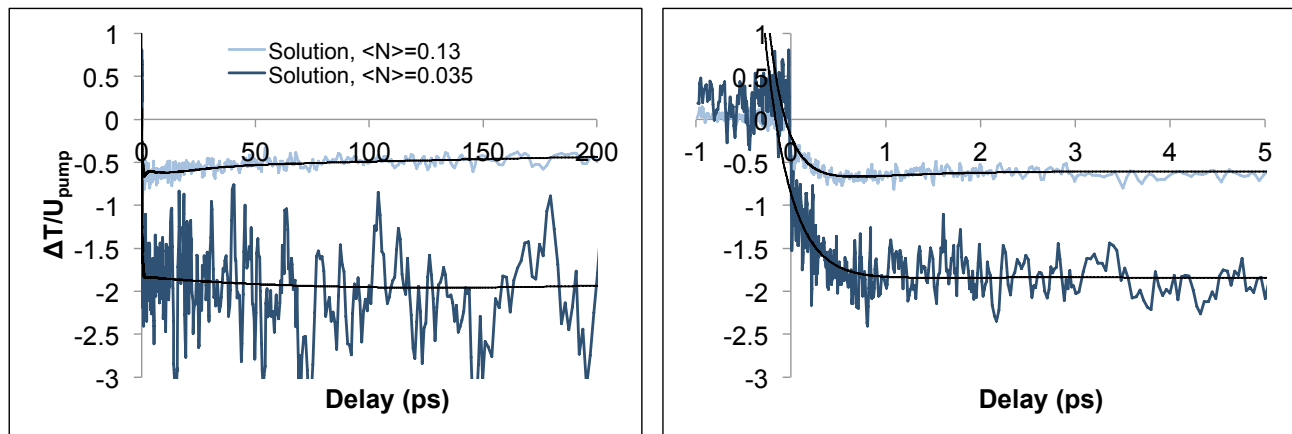


Figure 2.15: Degenerate pump-probe transients, recorded with the center of the pulse spectrum at 574nm, of 2nm diameter oleate-capped PbS in hexane, $\langle N \rangle = 0.035$ and 0.13, with multi-exponential fits. Transients and fits are shown out to 200ps (left) and to 5ps (right), although fits were made out to 500ps. The initial decays at early time appear very similar but some deviation can be seen at later times. The $\langle N \rangle = 0.035$ transient appears to decrease at long times (become more negative) but it is difficult to quantify because of the noise.

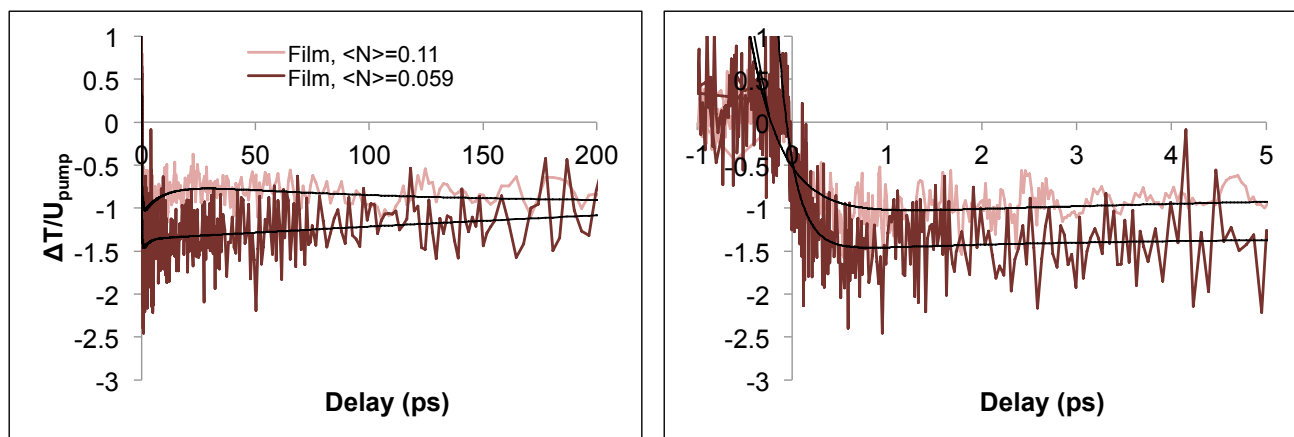


Figure 2.16: Pump-probe transients, recorded with the pulse spectrum centered at 574nm, for a film made from 2nm diameter oleate-capped PbS quantum dots, $\langle N \rangle = 0.059$ and 0.11, with multi-exponential fits. The transients are shown out to 200ps (left) and 5ps (right).

which are near the time constants found above at the band gap, but the low signal-to-noise of these transients produce very large errors that make it impossible to accurately compare them quantitatively.

Normalizing the transients at 1ps, just after the initial rise in negative signal, allows a qualitative comparison of the transient shapes for the solution and array at a particular $\langle N \rangle$. Figures 2.17 and 2.18 compare transients with similar $\langle N \rangle$ and show agreement within noise between the signals.

2.4 Conclusion

Results show that there is little to no difference in early time dynamics between colloidal solutions compared to uncoupled films of PbS when investigated with degenerate pump-probe at E_g or at $1.4E_g$. Although there are differences in experimental conditions between this study and previous studies that compare colloidal solutions to uncoupled arrays [4, 5] and find different biexciton lifetimes, some of these differences are not expected to affect the final results. Differences include: 1) refreshing both the film and the solution samples between laser shots; 2) pumping and probing degenerately; 3) studying PbS instead of PbSe; and 4) studying very small PbS. Each of these is addressed below:

First, 574nm pump-probe data was also taken of stationary film and solution samples. These transients (shown in the Appendix) have differences in amplitude, but normalizing at 1ps results in agreement within signal-to-noise for dynamics at early times (less than 50ps), which is within the timescale of biexciton decay in dots of this size. [12] Experiments at 800nm while refreshing and while stationary could further test this.

Second, data was taken both at the band gap, where other researchers probe [4, 9], and at less than $2E_g$. At both photon energies, multiple photons should be the only cause of multiple excitations. Both sets of data exhibit agreement in early time dynamics between solutions and films and they also show agreement in biexciton population decay times between one another. Extending the experiment to higher $\langle N \rangle$ (higher pump energies) at $< 2E_g$ would provide further evidence.

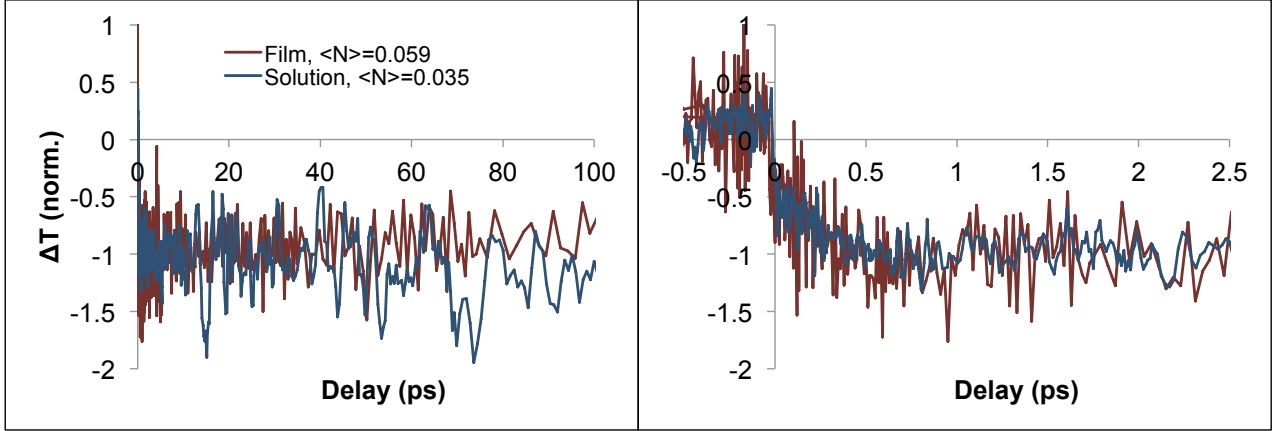


Figure 2.17: Pump-probe transients, recorded with a pulse spectrum centered at 574nm, for a film made from 2nm diameter oleate-capped PbS and for colloidal solution of the same dots, $\langle N \rangle = 0.059$ and 0.035, normalized at 1ps in order to compare the overall shape of decay and recovery of the signal. Transients are shown out to 100ps (left) and 2.5ps (right). With the normalization, it is apparent that the solution and film have the same decay and recovery dynamics (within the signal-to-noise) over the first hundred picoseconds.

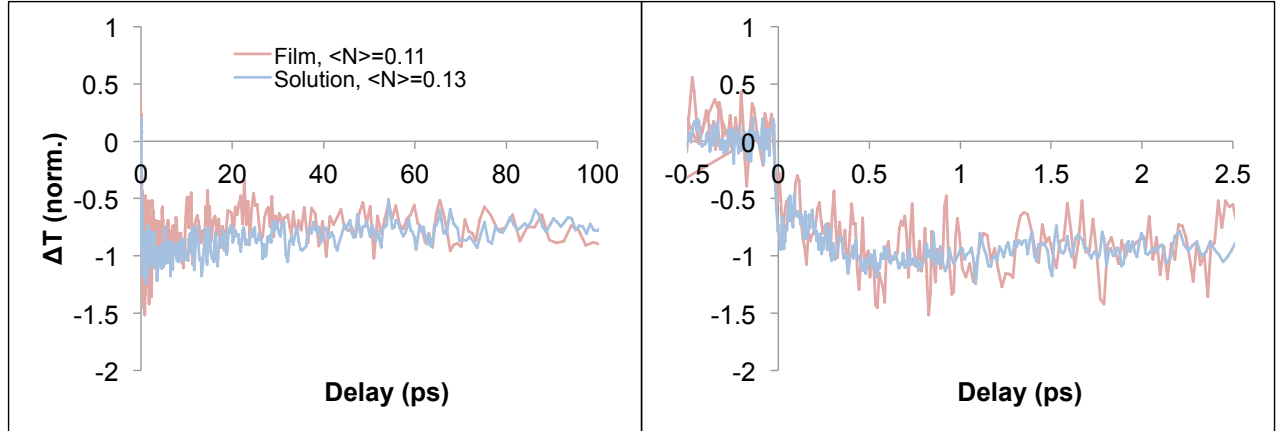


Figure 2.18: Degenerate pump-probe transients, recorded with the pulse spectrum centered at 574nm, of 2nm diameter PbS solution and film, $\langle N \rangle = 0.13$ and 0.11, normalized at 1ps in order to compare the overall shape of the decay and recovery of the signal. The transients are again shown out to 100ps (left) and 2.5ps (right). With the normalization, it is apparent that the solution and film have the same decay and recovery dynamics within the signal-to-noise, including a small dip that occurs at approximately 100fs and is not seen in samples at lower $\langle N \rangle$.

Third, many previous reports focus on the dynamics of PbSe while my study focuses on PbS; however, dynamics in lead chalcogenide systems follow similar trends so that differences in the biexciton decay of a PbSe solution and a PbSe array are also expected to be seen in a PbS solution and PbS array. Instead, my results show similar biexciton decay times for the solution and array.

Finally, this study focuses on QDs that are smaller than most other lead chalcogenide studies investigate. While 1.9nm diameter PbS are small, they are comparable to the 3.7nm diameter PbSe in the previously mentioned study by Beard et al [4] in their magnitude of confinement. This is because the Bohr exciton radius of PbSe is twice that of PbS (46nm compared to 18nm), so that they experience quantum confinement to a similar degree.

The most significant difference listed above is the degeneracy of pump and probe pulses. My use of degenerate pump-probe assures that resulting transients are not affected by differing attenuation of the pulses due to the frequency-dependence of the absorption cross-section which is not true of other studies that use non-degenerate pump-probe. Repeating measurements at 800nm on both refreshed and stationary samples would add additional evidence to the agreement of biexciton lifetimes in solution and film found as a result, but refreshing the sample does not appear to be a large influencing factor for the biexciton timescale as seen by degenerate pump-probe at 570nm.

This study is the first to compare a colloidal lead sulfide solution with an untreated film while refreshing both samples between laser shots and avoiding complications of the frequency-dependent absorption cross-section by using degenerate pump-probe. PbS dots have been used in recent, successful PV devices, [14] necessitating more fundamental studies to build a knowledge base about this material.

In summary, faster single exciton recombination is seen in the film compared to the solution and agrees with observations from a previous study of PbSe [9]. While the authors attribute it to an increase in surface recombination, exciton migration between QDs with subsequent quenching may also contribute. A 64ps time constant is observed for the film at the highest $\langle N \rangle$ but not for any of the other samples. Förster ET calculations indicate a minimum timescale of approximately

100ps if inter-particle spacing is decreased sufficiently, due to ligand breakage or contraction and packing during film deposition, which can account for this additional lifetime. At the highest $\langle N \rangle$, the sample is saturated which may also contribute to the likelihood of ET between neighboring QDs.

2.5 References

- [1] A. P. Spencer, R. J. Hill, W. K. Peters, D. Baranov, B. Cho, and D. M. Jonas, “Probed-volume sample renewal by beam scanning with applications to noncollinear pump-probe spectroscopy at kilohertz repetition rates,” (in preparation), 2014.
- [2] G. Konstantatos and E. H. Sargent, “PbS colloidal quantum dot photoconductive photodetectors: Transport, traps, and gain,” Applied Physics Letters, vol. 91, no. 17, pp. 173505–173505, 2007.
- [3] J. Lewis, S. Wu, and X. Jiang, “Unconventional gap state of trapped exciton in lead sulfide quantum dots,” Nanotechnology, vol. 21, no. 45, p. 455402, 2010.
- [4] M. C. Beard, A. G. Midgett, M. Law, O. E. Semonin, R. J. Ellingson, and A. J. Nozik, “Variations in the quantum efficiency of multiple exciton generation for a series of chemically treated PbSe nanocrystal films,” Nano Letters, vol. 9, no. 2, pp. 836–845, 2009.
- [5] J. M. Luther, M. Law, Q. Song, C. L. Perkins, M. C. Beard, and A. J. Nozik, “Structural, optical, and electrical properties of self-assembled films of PbSe nanocrystals treated with 1, 2-ethanedithiol,” ACS Nano, vol. 2, no. 2, pp. 271–280, 2008.
- [6] J. J. Urban, D. V. Talapin, E. V. Shevchenko, and C. B. Murray, “Self-assembly of PbTe quantum dots into nanocrystal superlattices and glassy films,” Journal of the American Chemical Society, vol. 128, no. 10, pp. 3248–3255, 2006.
- [7] A. Wolcott, V. Doyeux, C. A. Nelson, R. Gearba, K. W. Lei, K. G. Yager, A. D. Dolocan, K. Williams, D. Nguyen, and X.-Y. Zhu, “Anomalously large polarization effect responsible for excitonic red shifts in pbse quantum dot solids,” The Journal of Physical Chemistry Letters, vol. 2, no. 7, pp. 795–800, 2011.
- [8] B. Cho, V. Tiwari, and D. M. Jonas, “Simultaneous all-optical determination of molecular concentration and extinction coefficient,” Analytical Chemistry, 2013.
- [9] J. M. Luther, M. C. Beard, Q. Song, M. Law, R. J. Ellingson, and A. J. Nozik, “Multiple exciton generation in films of electronically coupled PbSe quantum dots,” Nano Letters, vol. 7, no. 6, pp. 1779–1784, 2007.
- [10] W. K. Peters, B. Cho, R. J. Hill, T. L. Courtney, and D. M. Jonas, “Band filling dynamics and auger recombination in lead sulfide nanocrystals,” in International Conference on Ultrafast Phenomena, Optical Society of America, 2010.
- [11] R. D. Schaller, M. A. Petruska, and V. I. Klimov, “Effect of electronic structure on carrier multiplication efficiency: Comparative study of PbSe and CdSe nanocrystals,” Applied Physics Letters, vol. 87, no. 25, pp. 253102–253102, 2005.
- [12] I. Robel, R. Gresback, U. Kortshagen, R. D. Schaller, and V. I. Klimov, “Universal size-dependent trend in auger recombination in direct-gap and indirect-gap semiconductor nanocrystals,” Physical Review Letters, vol. 102, no. 17, p. 177404, 2009.
- [13] T. Förster, “Zwischenmolekulare energiewanderung und fluoreszenz [Intermolecular energy migration and fluorescence],” Annalen der physik, vol. 437, no. 1-2, pp. 55–75, 1948.

- [14] A. H. Ip, S. M. Thon, S. Hoogland, O. Voznyy, D. Zhitomirsky, R. Debnath, L. Levina, L. R. Rollny, G. H. Carey, A. Fischer, et al., “Hybrid passivated colloidal quantum dot solids,” Nature nanotechnology, vol. 7, no. 9, pp. 577–582, 2012.

Chapter 3

Octylamine and 1,2-Ethanedithiol Treated Lead Sulfide Quantum Dots

3.1 Introduction

Building on the studies outlined in Ch. 2, this chapter addresses similar pump-probe experiments performed on lead sulfide quantum dots (QDs) that have been chemically treated to substitute the oleate ligand with a shorter organic ligand. In order to make quantum dots viable candidates for photovoltaics, strongly coupled arrays must be investigated. Many studies of lead chalcogenide dots pump and probe at different wavelengths to study stationary films that have undergone ligand exchange of bulky, passivating ligands, such as oleate, with smaller molecules that will decrease interparticle separation. [1–4]

In my study of QDs that have undergone ligand exchange, I employ degenerate pump-probe at the band gap and use the beam scanning technique developed in the Jonas group to minimize effects of repeated photoexcitation of the sample over a short period of time. [5] Using degenerate pump and probe pulses reduces complications that can occur due to the frequency-dependence of the absorption cross-section. [6]

For a meaningful comparison, I look at ligand exchange in solution in addition to investigating arrays of coupled dots that undergo ligand exchange as a film. Many of the ligands used to produce strongly coupled arrays are often not able to provide colloidal stability for dots in solution, so exchange is performed on an array; however, somewhat larger organics that are still less bulky than the original ligand can be used for ligand exchange in solution. In my work, I use octylamine for ligand exchange in solution and study these dots in their colloidal form and as an array made from

the colloidal solution before investigating coupled arrays treated with 1,2-ethanedithiol.

3.2 Experimental Procedure

3.2.1 Sample Preparation

Oleate-capped lead sulfide quantum dots dispersed in hexanes were purchased from Voxel Inc. Based on sizing information from Voxel, the center of the first absorption peak of the untreated colloidal solution at 820nm corresponds to a diameter of 1.9nm . As described in Chapter 2, colloidal samples were stored in the glovebox and transferred to air-free quartz cuvettes (1-mm path length) under argon after which the sealed sample cell was used in ambient atmosphere.

Anhydrous solvents ($\geq 99\%$) and ligands were purchased from Sigma-Aldrich. Hexane, octane, and octylamine (99%) were degassed by bubbling argon through for several hours on the Schlenk line before being transferred to the glovebox. Ethanol (200 proof) was purchased from Decon Laboratories, Inc. and degassed on the Schlenk line by bubbling argon through it for eight hours. 3\AA molecular sieves (alumina silicate) were purchased from Mallinckrodt Chemicals and added to the ethanol in the glovebox to absorb remaining water. 1,2-ethanedithiol ($\geq 98\%$ GC) was shipped from Sigma-Aldrich under air-free conditions, sealed with a Sure/SealTM cap, and immediately placed in the glovebox upon receipt. The glovebox atmosphere remained at ≤ 0.1 ppm O_2 and H_2O after degassed chemicals were introduced.

All thin film preparation took place in the glovebox with degassed, anhydrous solvents and ligands. Films were prepared on 1-inch (25.4mm) diameter (1mm thick) optical grade fused quartz substrates (Esco Optics) by drop-casting quantum dot solution (9:1 hexane:octane) onto the substrate. Films were allowed to dry overnight before sealing them in an air-free sample cell, described in Chapter 2.

Ligand exchanges were performed using two systems: octylamine and 1,2-ethanedithiol (EDT) in acetonitrile. EDT treatment was adapted from procedures described by Luther, et al. [7] and from personal correspondence with Dr. Joseph Luther at the National Renewable Energy Labora-

tory (NREL). This treatment consisted of placing an oleate-capped drop-cast film in 1mM EDT in acetonitrile for two minutes and then allowing it to dry in the glovebox for approximately 10 minutes.

Octylamine treatment was based on procedures detailed by the Sargent lab at the University of Toronto [8–10]. In the glovebox, 1mL of degassed, anhydrous octylamine was added to approximately 2mL of a concentrated solution (3mg/mL) of oleate-capped PbS in hexanes, the mixture was shaken by hand to allow mixing of the reagents, and then allowed to sit undisturbed for 48hours. The octylamine treated QDs were precipitated by addition of ethanol, a non-solvent, followed by centrifugation. The dots were re-dispersed in approximately 3mL of hexane to produce a concentrated stock solution that could be diluted as needed based on OD. The colloidal solution and thin films were stored in the glovebox and sealed in the air-free cuvette and sample cells as described previously.

3.2.2 Characterization

Linear absorption spectra were taken with a Varian Cary 500 UV-VIS-NIR Spectrophotometer. Spectra of the octylamine-treated solution are compared to those of the original oleate-capped dots in Figure 3.1 and spectra of the EDT- and octylamine-treated arrays are compared to an oleate-capped array in Figure 3.2.

The first absorption feature of the octylamine-treated solution, as well as the film made from it, and the EDT-treated films are red-shifted with respect to the untreated samples. A similar small red-shift between solution and uncoupled array has been reported in other studies. [4, 5] This shift has previously been attributed to: 1) an increase in dipole-dipole interactions between neighboring dots [11]; 2) polarization effects caused by dielectric changes in the environment [12]; 3) a combination of 1 & 2 [7]; or 4) sintering of properly oriented particles spaced very closely together [13].

Some ligand treatments, such as EDT, also cause changes in the shape of the absorbance spectrum, resulting in the increased slope at energies higher than the bandgap and broadening of

the first exciton peak. In previous reports, linear absorption spectra of EDT treated QDs show continued absorption on the low energy side of E_g , which the authors attribute to scattering. [1, 7] A similar feature is seen in Figure 3.2 for the second EDT-treated sample and continues to decrease out to 2500nm, the end of the collected spectrum. An alternative explanation of this feature is the formation of bulk-like areas of the film, produced as some of the dots sinter together, resulting in both bulk and QD contributions to the linear absorption spectrum.

The first EDT-treated sample shows less absorption red of E_g than the second, which varies depending on the portion of the film in the path of the light. This observation suggests that the method of EDT-treatment under our conditions is not reproducible and may result in varying dynamics for each of the samples.

All pump-probe transients were taken on samples of quantum dots from the same batch but have different OD and spectral shape due to the effects of various treatments. The resulting first exciton peaks and ODs at 800nm are 867nm and 0.19 (first EDT-treated film), 876nm and 0.13 (second EDT-treated film), 830nm and 0.078 (octylamine-treated solution), and 832nm and 0.031 (octylamine-treated film). Similar to the untreated colloidal solution and film discussed in Ch. 2, deposition of the octylamine-treated solution results in a small red-shift of the first absorption peak.

In order to assess whether dots retained their size and shape after ligand exchange, images of the oleate-capped and octylamine-treated QDs were taken with a 300kV [$\lambda = 1.97\text{pm}$] Phillips CM30 Transmission Electron Microscope (TEM) with the help of Dr. Joseph Luther at the National Renewable Energy Laboratory and are shown in Figure 3.3. From the images that were taken, the octylamine-treated QDs appear to be more closely spaced than the oleate-capped PbS. Although oleate ligand length suggests a 3.6nm distance between QDs, a high packing density results in a decrease in particle separation [14] resulting in an estimated 2nm separation between oleate-capped dots, while 1nm interparticle distance is expected from the octylamine-treated dots. The expected difference is due to the length of octylamine, an 8-carbon chain, compared to that of oleic acid, an 18-carbon chain.

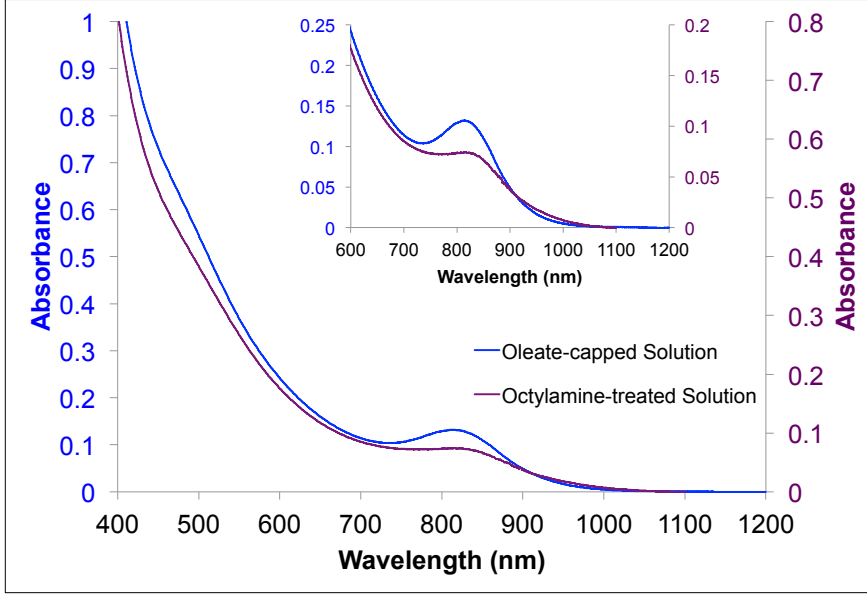


Figure 3.1: Linear absorption spectra of 2nm diameter PbS quantum dots in hexane. The oleate-capped PbS is in blue and the octylamine-treated PbS is in purple [$OD(800nm) = 0.078$ and $E_g = 830nm$]. The blue y-axis shows OD for the oleate-capped PbS while the purple axis shows OD for the octylamine-treated PbS. The inset highlights the small red-shift and broadening of the first exciton peak after treatment.

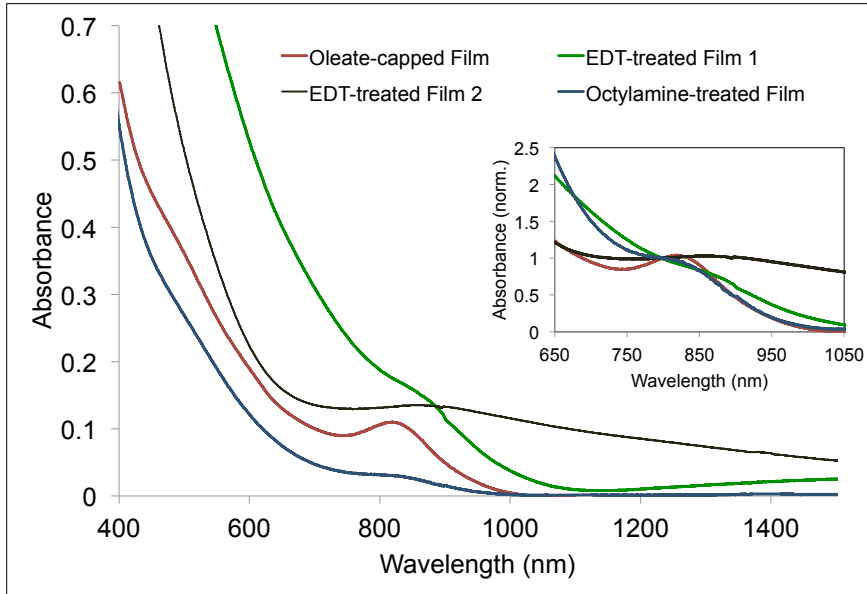


Figure 3.2: Linear absorption spectra of 2nm diameter PbS quantum dot arrays. The oleate-capped PbS is in red; the octylamine-treated PbS is in blue [$OD(800nm) = 0.032$ and $E_g = 832nm$]; the first PbS sample treated with EDT is in green [$OD(800nm) = 0.19$ and $E_g = 867nm$]; and the second PbS sample treated with EDT is in dark brown [$OD(800nm) = 0.13$ and $E_g = 876nm$]. The inset shows the arrays normalized at 800nm.

Comparing the TEM images of the oleate-capped dots and the octylamine treated dots, the latter sample appears to have some aggregation. This could be caused by QDs on top of one another as a consequence of sample preparation (i.e., too concentrated a sample was used) or by ‘sintering’ occurring between dots properly oriented and closely spaced to one another. [13] In order to distinguish the possible cause, TEM images of more dilute solutions and/or high-resolution TEM (HRTEM) images are needed but have yet to be obtained.

3.2.3 Pump-Probe Measurements

Pump-probe measurements were made using the sub-100fs, 800nm output of a RegA 9000 regenerative amplifier with 10kHz repetition rate and approximately $50\mu\text{m}$ spot size at the sample. The spot size is determined by characterizing the overlap of the pump and probe beams as described in Chapter 2 and was found to be $42.4\mu\text{m}$, $51\mu\text{m}$, $51\mu\text{m}$, $43.7\mu\text{m}$, and $48.4\mu\text{m}$ for the first EDT-treated film (EDT1), the second EDT-treated film (EDT2), the octylamine-treated film, the first octylamine-treated solution (S1), and a second octylamine-treated solution (S2), respectively.

The average probe power was maintained around $5.5\mu\text{W}$ while the pump power was varied, in some cases from $28\mu\text{W}$ to $660\mu\text{W}$, to collect data at different excitation probabilities, or average number of photons absorbed per quantum dot $\langle N \rangle$, which is calculated as described in Ch. 2.

3.3 Results & Discussion

3.3.1 Octylamine-treated PbS

Since ligand exchange involving octylamine is done in solution, it is possible to obtain transients of the solution as well as the film. Figure 3.4 shows both solution and film data, normalized by the respective pump power and OD. At a later date, the experiment was repeated on another solution sample but not on the film. The linear absorption spectrum of the second solution (S2) includes some broadening of the first exciton peak but no peak shift compared to the first solution (S1), which indicates a change in QD size distribution over time, and is shown in the Appendix.

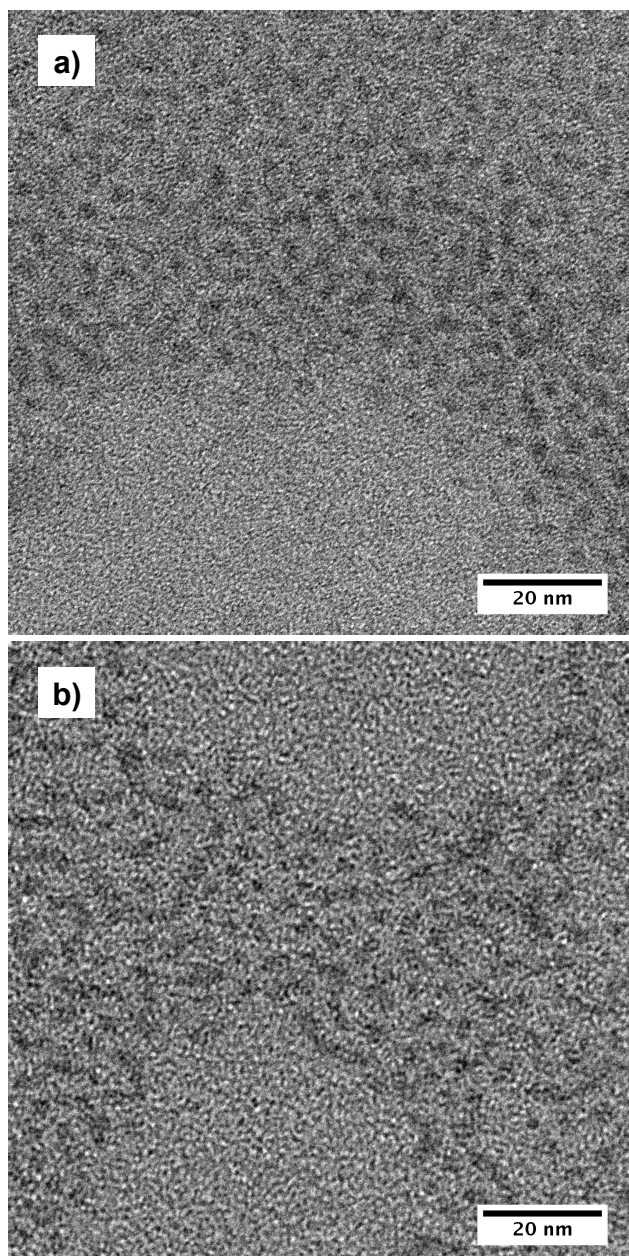


Figure 3.3: Images of 1.9nm diameter oleate-capped PbS (a) and octylamine-treated PbS (b) taken with a Phillips CM30 TEM at NREL. Octylamine-treated QDs are more closely spaced than oleate-capped dots due to the shorter ligand length. The text provides a further description of differences.

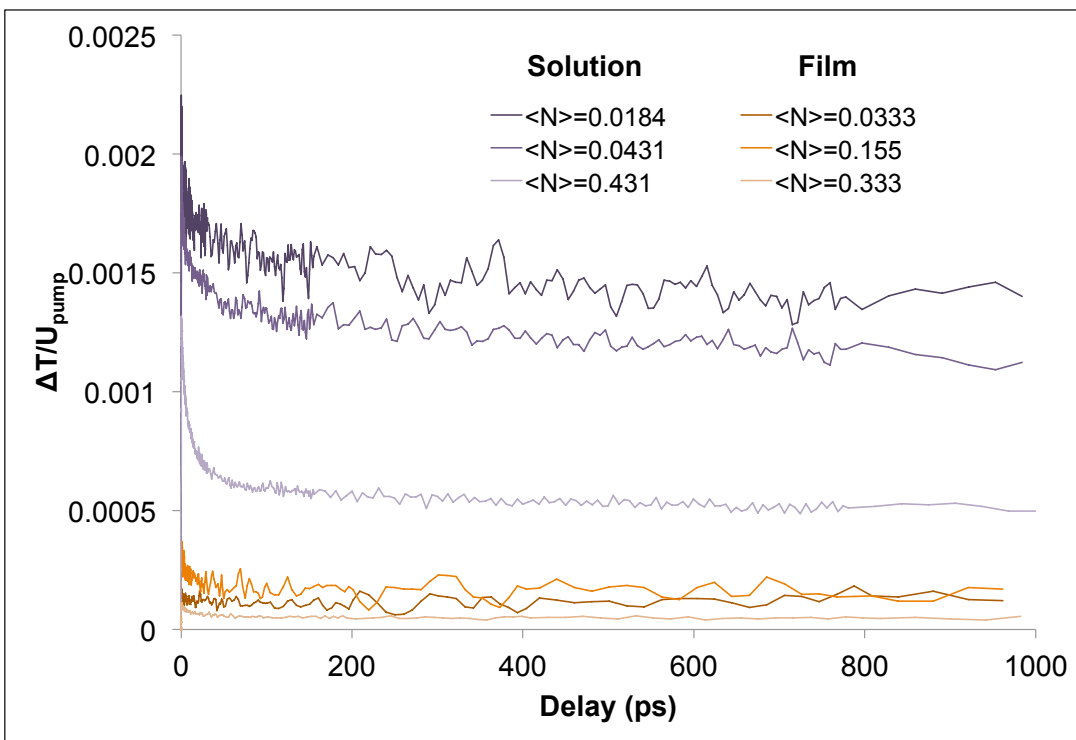


Figure 3.4: Pump-probe transients recorded using pulse spectra centered at 800nm for octylamine-treated PbS in hexane solution ($OD(800nm) = 0.078$) and as a drop-cast film ($OD(800nm) = 0.031$). The pump-induced change in probe transmission, ΔT , is divided by the respective energy per pump pulse and OD of the sample.

Figure 3.5 compares the two solution samples after normalizing at their respective pump powers and OD. Figure 3.6 shows them normalized at long times, when single exciton recombination is expected to be the same. S1 transients were taken in late September 2012 and S2 transients were taken in early November 2012, less than two months apart. When transients of the two solutions are normalized at long times (Figure 3.5) differences in signal amplitude are apparent, but transients have a similar overall shape.

3.3.1.1 Discussion

Octylamine-treated samples are initially analyzed, as described in Chapter 2, by determining the ratio of (a/b) for each transient, which is proportional to the number of excitons per quantum dot. As described in Chapter 2, ‘ a ’ is the signal at early times of the long-time normalized transient while ‘ b ’ is found from the early time signal of the long-time normalized transient with the lowest $\langle N \rangle$. The transient with the lowest $\langle N \rangle$ is assumed to contain predominately signal from single exciton decay and negligible contributions from multiexcitons. The experimentally found number of excitons per dot for these samples is discussed below.

For S1, $(a/b) = 1.1; 1.2; \text{ and } 1.8$ in order of increasing $\langle N \rangle$, while the film results in $(a/b) = 1.2; 1.6; \text{ and } 1.9$ as the fluence increases; however, S2 shows a more rapid increase in the number of excitons as $\langle N \rangle$ increases, resulting in $(a/b) = 1.3; 1.4; 1.7; 2.3; \text{ and } 2.9$. The large difference in (a/b) for S1 and S2 may be related to the broadening of the first exciton peak in S2. Again, data for low $\langle N \rangle$ transients are expected to follow Poisson statistics at E_g because of the eight-fold degeneracy in lead chalcogenides, but will deviate at higher $\langle N \rangle$, when the sample is saturated. As in Chapter 2, (a/b) is assumed to be equal to $\langle N_{eh} \rangle$, found using Poisson statistics. Figure 3.7 shows that while the film and the first solution (S1) agree with one another and are near the Poisson curve at low $\langle N \rangle$, the second solution (S2) deviates more quickly and is similar to data shown for MEG experiments [15], which lies above the Poisson curve.

Transients in each sample with the lowest $\langle N \rangle$ are assumed to contain negligible contributions from multiexcitons and reflect decay from only single excitons. Normalizing each set of transients

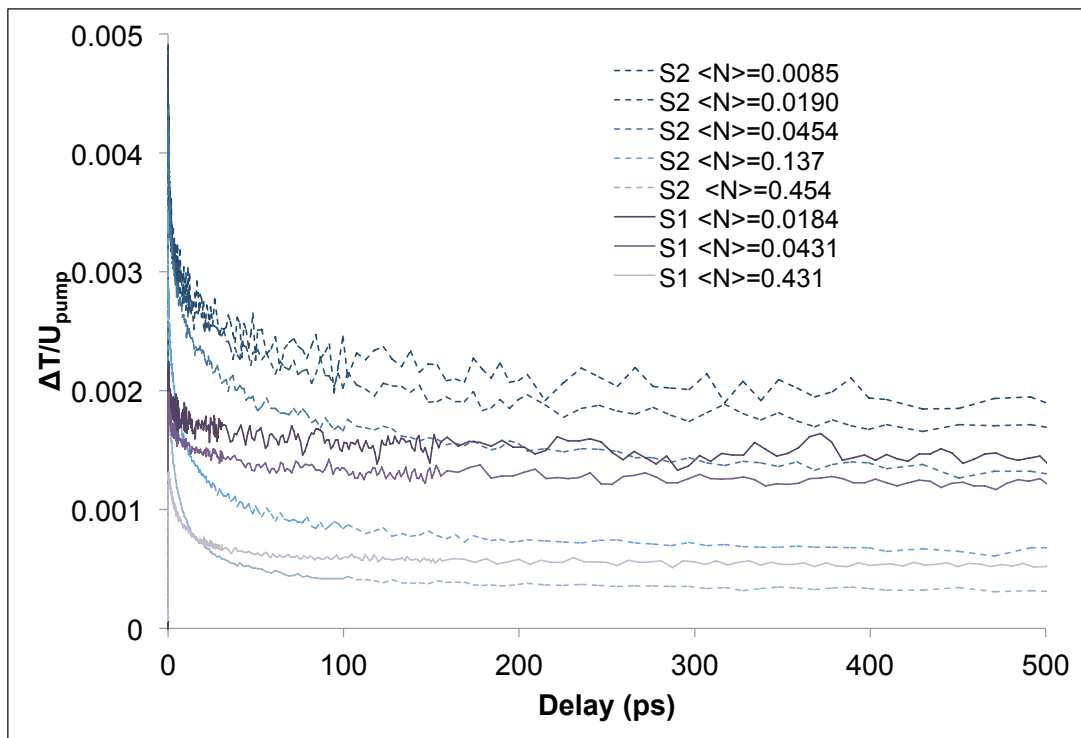


Figure 3.5: Pump-probe transients recorded using pulse spectra centered at 800nm for octylamine-treated PbS in hexane. S1(purple) and S2 (blue) represent solutions taken from the same stock solution at different times and diluted to similar ODs. S2 transients were taken less than two months after S1 transients. The pump-induced change in probe transmission, ΔT , is divided by the respective energy per pump pulse and OD of the sample.

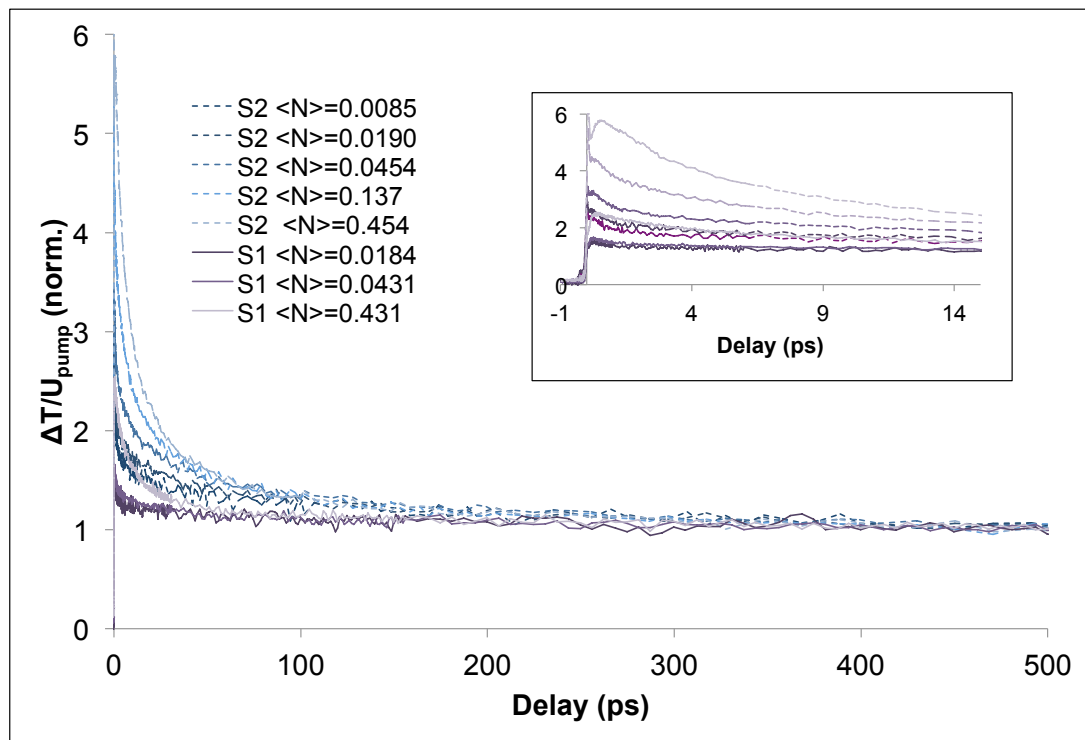


Figure 3.6: Pump-probe transients, recorded using pulse spectra centered at 800nm, of the two octylamine-treated PbS solutions from Figure 3.5 are normalized at long times to find (a/b) , as described in the text.

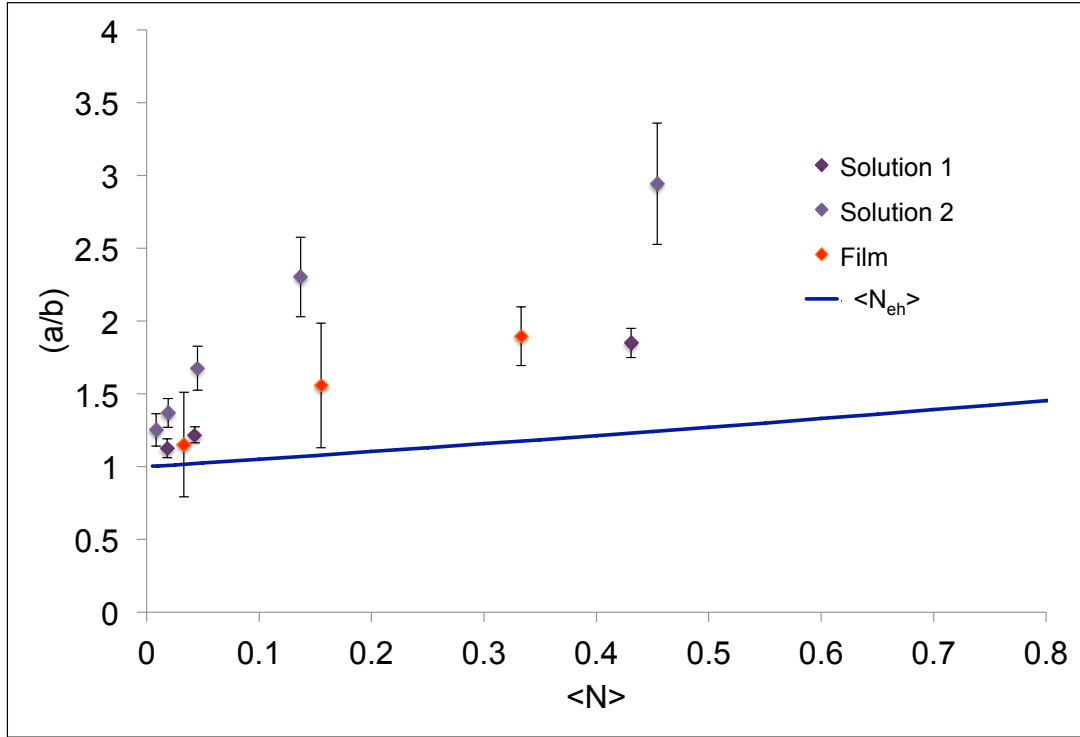


Figure 3.7: The octylamine-treated film in orange and the two solution samples in purple are compared to the expected number of excitons using Poisson assumptions. The spatially averaged number of photons absorbed per QD, $\langle N \rangle$, is shown on the x-axis, while the experimental indicator for the number of excitons per QD, (a/b) , is on the y-axis. The (a/b) ratio is experimentally determined but the curve, $\langle N_{eh} \rangle = \frac{\langle N \rangle}{1 - e^{-\langle N \rangle}}$, is the number of excitons expected based on Poisson assumptions. These equations are discussed in Chapter 2. Although the data points for S1 and the film are similar to one another, data from S2 shows an early departure from the other samples as well as the curve.

at long times allows a multiple of the lowest excitation probability signal to be subtracted from transients with higher $\langle N \rangle$. The resulting transients for both solutions and the film are shown in Figures 3.8-3.10. While the decay of a single exciton is usually described by a single exponential in the literature, the lowest $\langle N \rangle$ transients require multi-exponential fits, which are summarized in Table 3.1.

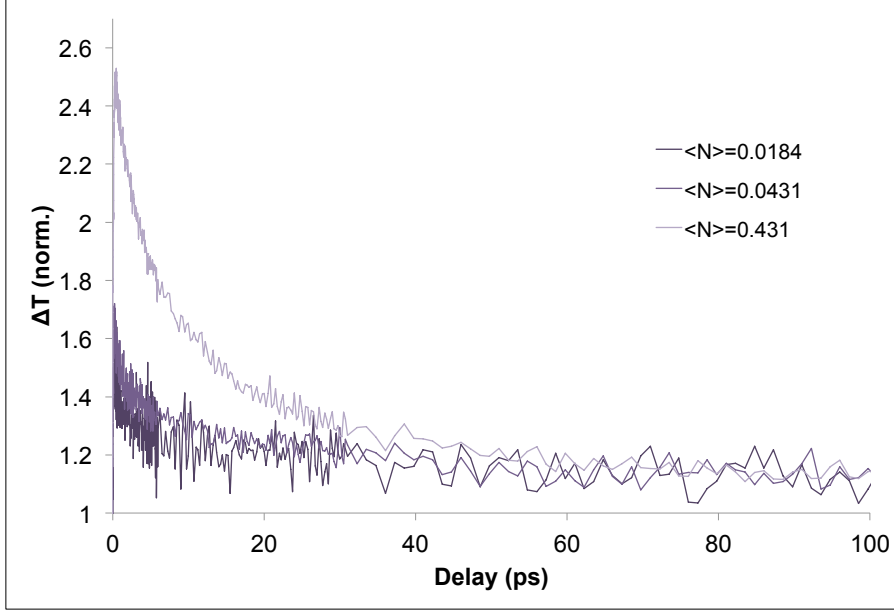


Figure 3.8: Long-time normalized pump-probe transients of the first sample of 2nm diameter octylamine-treated PbS in hexane (S1) for $\langle N \rangle = 0.431$ and $\langle N \rangle = 0.0431$ (shown in Figure 3.6) with the normalized multiple of the lowest excitation probability signal, $\langle N \rangle = 0.0184$, subtracted.

While differences in signal size can be seen in the transients, τ_2 values in both solutions and in the array are consistent with one other but systematically a few picoseconds shorter than those found for the untreated samples in Ch. 2. There is an early time decay seen in both solutions at low $\langle N \rangle$ of less than 1ps which may not be discernible in the film transient due to noise. This early time constant, labeled τ_3 , is similar to that found in the untreated samples discussed in Ch. 2.

An additional lifetime is present, $\tau_{2'}$, for the two solutions and the array, which agree at the lowest $\langle N \rangle$ of each sample, but vary as $\langle N \rangle$ increases, especially in the case of S2. They are similar in order of magnitude and although they do not agree as closely as in the case of τ_2 , $\tau_{2'}$ values agree well within error for the film and S1. Like τ_2 , the $\tau_{2'}$ amplitude increases with $\langle N \rangle$.

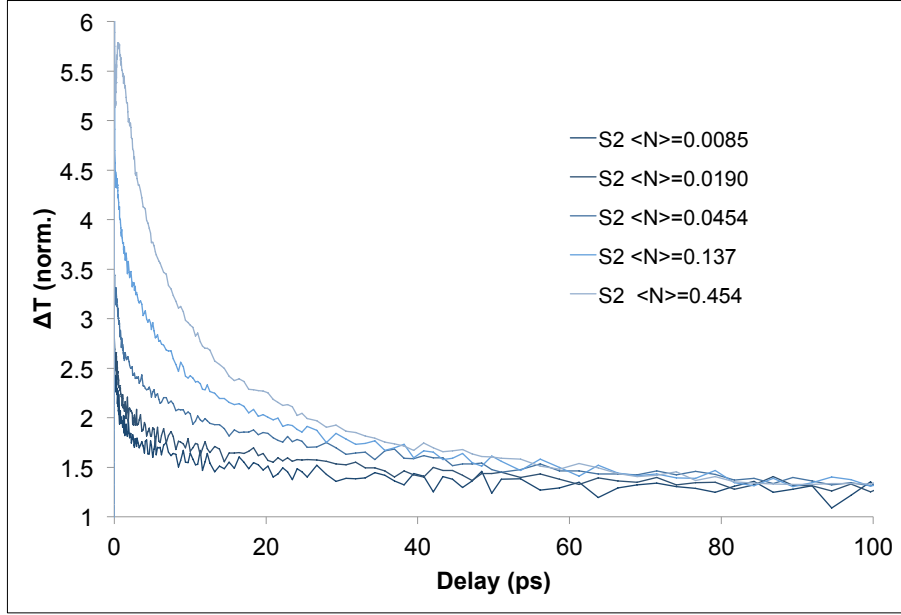


Figure 3.9: Long-time normalized pump-probe transients of the second sample of 2nm diameter octylamine-treated PbS in hexane (S2) for $\langle N \rangle = 0.454$, $\langle N \rangle = 0.137$, $\langle N \rangle = 0.0454$, and $\langle N \rangle = 0.0190$ (shown in Figure 3.6) with the normalized multiple of the lowest excitation probability signal, $\langle N \rangle = 0.0085$, subtracted.

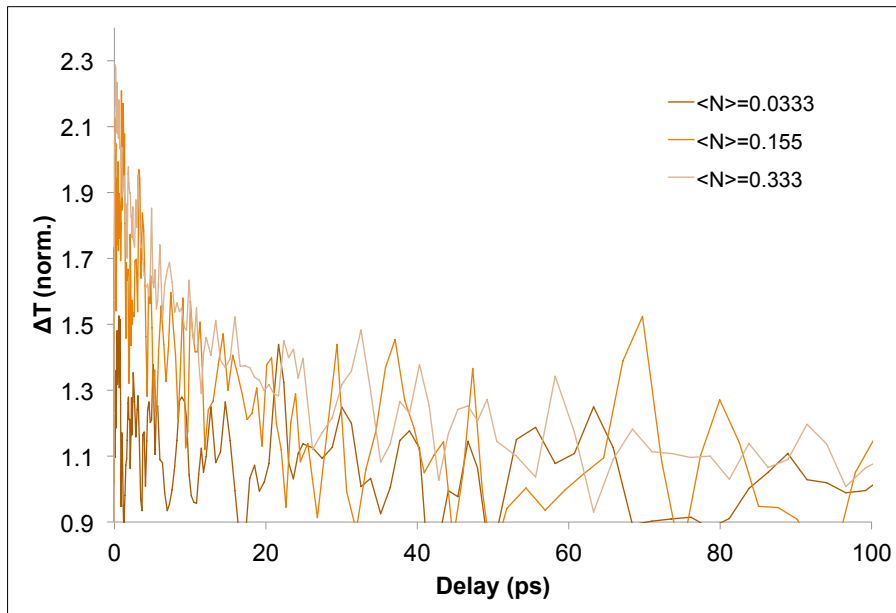


Figure 3.10: Long-time normalized pump-probe transients of film made from 2nm diameter octylamine-treated PbS for $\langle N \rangle = 0.333$ and $\langle N \rangle = 0.155$ (shown in Figure 3.4), with the normalized multiple of the lowest excitation probability signal, $\langle N \rangle = 0.0333$, subtracted.

| | $\langle N \rangle$ | A | τ_3 | B | τ_2 | C | $\tau_{2'}$ | D | τ_1 |
|------|---------------------|-------------|--|------|------------------------|------|--------------------------|-------------|-------------------------------------|
| Film | 0.0333 | - | - | - | - | 0.24 | $23.3 \pm 7.0\text{ps}$ | 0.97 | $> 1\text{ns}$ |
| | 0.155 | - | - | 0.47 | $3.8 \pm 1.7\text{ps}$ | 0.47 | $34.8 \pm 12.0\text{ps}$ | <i>0.97</i> | <i>$> 1\text{ns}$</i> |
| | 0.333 | - | - | 0.58 | $3.0 \pm 0.5\text{ps}$ | 0.59 | $40.5 \pm 4.7\text{ps}$ | <i>0.97</i> | <i>$> 1\text{ns}$</i> |
| S1 | 0.0184 | 0.27 | $0.8 \pm 0.1\text{ps}$ | - | - | 0.18 | $26.3 \pm 3.8\text{ps}$ | 1.13 | $> 1\text{ns}$ |
| | 0.0431 | 0.25 | <i>$0.8 \pm 0.1\text{ps}$</i> | 0.09 | $4.3 \pm 1.8\text{ps}$ | 0.23 | $29.0 \pm 4.1\text{ps}$ | <i>1.13</i> | <i>$> 1\text{ns}$</i> |
| | 0.431 | 0.21 | <i>$0.8 \pm 0.1\text{ps}$</i> | 0.77 | $5.1 \pm 0.2\text{ps}$ | 0.53 | $27.6 \pm 1.5\text{ps}$ | <i>1.13</i> | <i>$> 1\text{ns}$</i> |
| S2 | 0.0085 | 0.76 | $0.8 \pm 0.1\text{ps}$ | - | - | 0.52 | $21.2 \pm 1.5\text{ps}$ | 1.40 | $> 1\text{ns}$ |
| | 0.0190 | <i>0.76</i> | <i>$0.8 \pm 0.1\text{ps}$</i> | 0.12 | $3.6 \pm 1.3\text{ps}$ | 0.15 | $68.0 \pm 14.8\text{ps}$ | <i>1.40</i> | <i>$> 1\text{ns}$</i> |
| | 0.0454 | <i>0.76</i> | <i>$0.8 \pm 0.1\text{ps}$</i> | 0.48 | $4.0 \pm 0.3\text{ps}$ | 0.47 | $57.7 \pm 3.2\text{ps}$ | <i>1.40</i> | <i>$> 1\text{ns}$</i> |
| | 0.137 | <i>0.76</i> | <i>$0.8 \pm 0.1\text{ps}$</i> | 1.35 | $4.5 \pm 0.2\text{ps}$ | 0.92 | $34.3 \pm 1.8\text{ps}$ | <i>1.40</i> | <i>$> 1\text{ns}$</i> |
| | 0.454 | <i>0.76</i> | <i>$0.8 \pm 0.1\text{ps}$</i> | 2.83 | $4.8 \pm 0.2\text{ps}$ | 1.34 | $26.7 \pm 1.4\text{ps}$ | <i>1.40</i> | <i>$> 1\text{ns}$</i> |

Table 3.1: Coefficients and decay times for 1.9nm diameter octylamine-treated PbS in hexane and as an array based on the multi-exponential fit, $Ae^{-t/\tau_3} + Be^{-t/\tau_2} + Ce^{-t/\tau_{2'}} + De^{-t/\tau_1}$. Values in italics denote those taken from the fit of the transient with the lowest $\langle N \rangle$, rather than an independent fit, and dashes denote no values associated with the respective coefficient and τ .

The $\tau_{2'}$ lifetime may be a contribution from dots that sintered during the ligand exchange process in solution, producing a larger nanocrystal with its corresponding longer AR lifetime. Although there is no apparent contribution of sintered QDs in the linear absorption spectra of either the octylamine-treated solution or film, a small fraction of sintered dots may be responsible for $\tau_{2'}$ but not be easily observed in the linear spectra. Guyot-Sionnest attributes the majority of the red-shift and broadening of the first-exciton peak in closely packed arrays to sintering of closely spaced, properly oriented QDs. [13] This explanation is also plausible when considering ligand exchange occurring in a highly concentrated solution of QDs, as in the case of the octylamine exchange.

Robel et al. [16] report a universal *effective* biexciton rate constant dependent on QD size, $C_A = (V_0)^2(8\tau_2)^{-1}$, in colloidal solutions of dots passivated with bulky organic ligands. It is not apparent that this can be extended to dots that have undergone ligand exchange since exchanges on arrays with shorter molecules, such as 1,2-ethanedithiol, are reported to have much longer biexciton lifetimes compared to the original QDs with bulky ligands [1,2], but may be applicable in the case of the octylamine-exchange in solution. However, analysis of the octylamine-treated dots shows that the τ_2 values in Table 3.1 fall within the predicted range of 0.5ps to 8ps for 2nm diameter QDs. If some fraction of QDs became sintered during the solution exchange, then at least a 2- or 3-fold increase in the original QD volume is expected. Extrapolating biexciton lifetimes from reports of volume dependence of nanorod lifetimes, in which $\tau_{2'} \propto V$ (volume) [17,18], yields a lifetime between 30ps and 45ps, which agrees with lifetimes listed as $\tau_{2'}$.

3.3.2 EDT-treated PbS

Figures 3.11 and 3.12 show pump-probe transients obtained for two different EDT-treated films, made from the same batch of 1.9nm QDs at different times. The first film (EDT1), shown in 3.11, shows an increasingly negative signal with increasing excitation probability within the first picosecond, which reflects an increase in excited state absorption (ESA). The transient with $\langle N \rangle = 0.310$ recovers in less than 2ps and has a small bleach around 2.5ps but the signal becomes negative again at 5ps, finally becoming positive near 200ps and remaining constant to 1ns. The

second EDT-treated array (EDT2) shows a ground state bleach (GSB) that decreases in amplitude with increasing $\langle N \rangle$, but remains a positive signal before decaying to zero.

The difference in transients of samples that have undergone the same treatment and have similar $\langle N \rangle$ indicates that the EDT-ligand exchange used here is not well reproduced. As mentioned earlier, this is also seen by the difference in the linear absorption spectra.

3.3.2.1 Discussion

Carrier dynamics in coupled films, such as the EDT-treated ones described here, are complicated by fast exciton transfer between QDs, which is more likely to occur in these films than in uncoupled or weakly coupled arrays. In this case, low $\langle N \rangle$ may not necessarily mean that a single exciton exists per QD since carriers can more easily travel between dots. For this reason, it is better to find multi-exponential fits to each transient individually rather than assuming a normalized multiple of the transient with lowest $\langle N \rangle$ can be subtracted, as done with the octylamine-treated samples. Coefficients and lifetimes obtained from multi-exponential fits are shown in Table 3.2.

| | $\langle N \rangle$ | A | τ_2 | B | $\tau_{2'}$ | C | τ_1 |
|------|---------------------|-------|------------------------|--------|-------------------------|--------|--------------------------|
| EDT1 | 0.310 | 0.096 | $5.3 \pm 0.6\text{ps}$ | -0.096 | $212 \pm 29.6\text{ps}$ | 0.050 | $> 1\text{ns}$ |
| | 0.140 | 0.11 | $3.8 \pm 0.8\text{ps}$ | 0.18 | $19.9 \pm 1.6\text{ps}$ | 0.026 | $> 1\text{ns}$ |
| | 0.013 | 0.42 | $3.5 \pm 0.6\text{ps}$ | 0.44 | $38.8 \pm 3.7\text{ps}$ | -0.093 | $> 1\text{ns}$ |
| EDT2 | 0.331 | 0.025 | $2.3 \pm 0.6\text{ps}$ | 0.069 | $13.3 \pm 0.7\text{ps}$ | 0.014 | $256 \pm 79.4\text{ps}$ |
| | 0.149 | 0.040 | $1.4 \pm 0.4\text{ps}$ | 0.071 | $13.2 \pm 0.9\text{ps}$ | 0.031 | $87.0 \pm 5.5\text{ps}$ |
| | 0.033 | 0.041 | $2.4 \pm 1.5\text{ps}$ | 0.070 | $13.2 \pm 3.2\text{ps}$ | 0.036 | $85.0 \pm 11.2\text{ps}$ |

Table 3.2: Coefficients and decay times for 1.9nm diameter EDT-treated PbS arrays based on multiexponential fits of individual transients, $Ae^{-t/\tau_2} + Be^{-t/\tau_{2'}} + Ce^{-t/\tau_1}$. A , B , and C are coefficients in the fits.

Auger recombination lifetimes, τ_2 values, are similar for each of the samples with varying $\langle N \rangle$ but are slightly longer in the case of EDT1 compared to EDT2. Similar to the octylamine-treated samples discussed previously, an additional lifetime is found, $\tau_{2'}$, which agrees for different $\langle N \rangle$ in EDT2, but varies in EDT1. As with the octylamine-treated sample, $\tau_{2'}$ may be due to sintering of QDs during ligand exchange, which results in a mixture of the original 1.9 nm diameter PbS dots and larger volume nanocrystals; however, the 13ps lifetime found for EDT2 is shorter than the

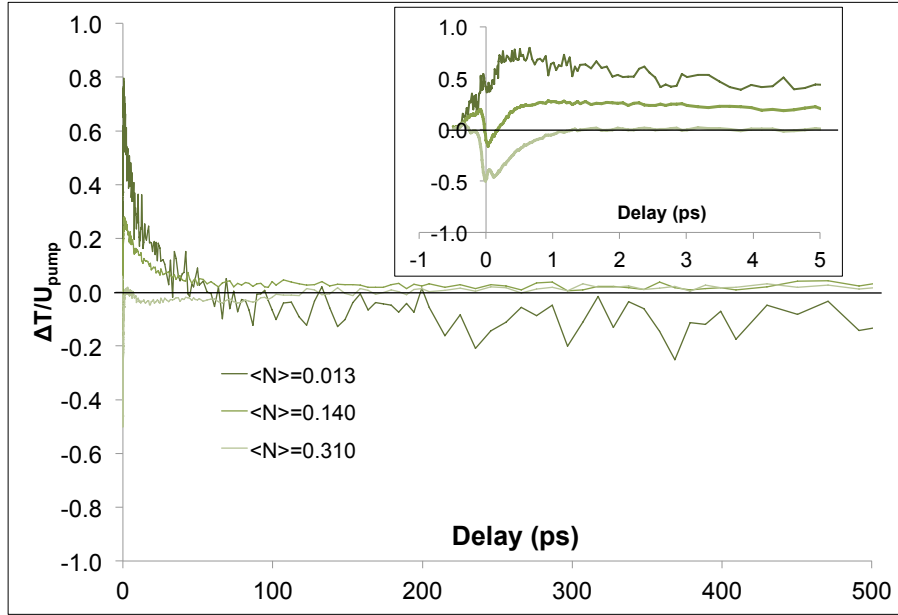


Figure 3.11: Pump-probe transients, recorded using a pulse spectrum centered at 800nm, of the first EDT-treated array (EDT1) are shown ($OD(800nm) = 0.19$). The inset shows that transients approach zero very early compared to uncoupled arrays. The positive amplitude at early times of the transient with the lowest excitation probability, $\langle N \rangle = 0.013$, reflects a ground state bleach, but an initial negative signal (induced absorption) appears at time zero for a higher excitation probability of 0.140. This signal quickly recovers, within 200fs, and becomes positive. Raising $\langle N \rangle$ to 0.310 increases the negative signal at time zero, which does not decay to zero until approximately 1.5ps. Higher $\langle N \rangle$ also appears to prevent ground state bleach from making large signal contributions.

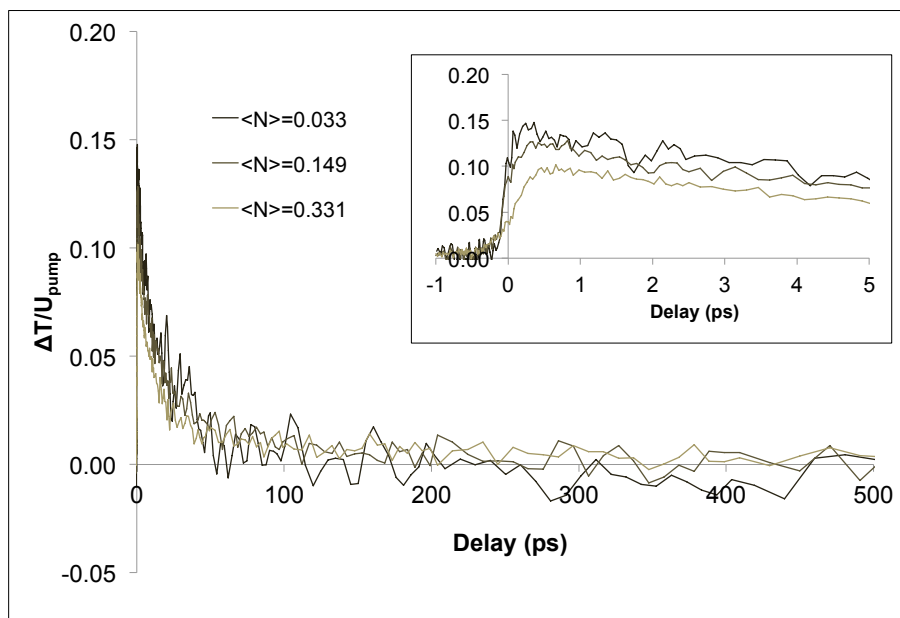


Figure 3.12: Pump-probe transients, recorded using a pulse spectrum centered at 800nm, of the second EDT-treated film, EDT2 ($OD(800nm) = 0.13$). The positive transient signals at time zero (see inset) indicate ground state bleach dominates, regardless of $\langle N \rangle$. Similar to transients for EDT1, the signals quickly approach zero within about 100ps.

30-45ps constant expected for a 2- or 3-fold increase in nanocrystal volume [16]. The increase in AR from the untreated sample of 6-7ps to 13ps for EDT2 agrees with previous studies that attribute the increase to electron delocalization [1].

EDT1 is more complicated due to the negative signal caused by an increase in excited state absorption that appears with $\langle N \rangle = 0.310$. In addition, the longtime signal of $\langle N \rangle = 0.13$, which appears to go below zero, forces a negative coefficient for τ_1 . Single exciton lifetimes, τ_1 , for EDT2 are orders of magnitude shorter than for untreated QDs and increase with increasing fluence. A shorter lifetime is seen in other studies, but is an order of magnitude greater than what is observed here. [1,2] This difference may be partially attributed to trap state formation during ligand exchange here, but may also be a result of the small size of the QDs studied here.

3.4 Conclusion

To summarize, 2 nm diameter PbS QDs treated with octylamine are shown to have similar biexciton lifetimes in colloidal solution and in an array, but an additional, short (<100ps) lifetime is also found in these experiments. This agreement indicates that deposited films are more similar to their colloidal precursors than previously shown. Since the additional time component is found in both solution and array, it may be due to partial sintering of dots that occurs during the ligand-exchange process, as was discussed earlier in the context of TEM results.

While exciton delocalization over neighboring QDs in a film, as discussed in literature [1], may account for the $\tau_{2'}$ lifetime in the octylamine-treated array studied here, it does not account for τ_2 , which corresponds to the AR time of the original oleate-capped PbS sampled discussed in Ch. 2. Those reports that attribute longer AR lifetimes in ligand-exchanged samples to delocalization look only at array samples and do not compare the lifetimes to colloidal solutions of ligand-exchanged QDs. The agreement between AR lifetimes in the octylamine-solution and array indicate that sintering is likely responsible for the increase in AR lifetime rather than electron delocalization, an effect which should not be seen in a colloidal solution since dots are not closely spaced.

Similarly, an additional lifetime is found for the 2nm PbS QDs from the same stock solution,

but treated with EDT rather than octylamine. Based on previous reports and the octylamine-treated samples discussed in this chapter, it is reasonable to assume that sintering may have also occurred during EDT treatment and contributes to the additional lifetime. Although EDT-ligand exchange resulted in films of varying properties, as seen in linear absorption spectra and discussed earlier, transients of the two samples yielded similar lifetimes of several picoseconds, τ_2 .

Assigning the AR time as $\tau_{2'}$ for the EDT-treated films is consistent with the increases in biexciton decay time reported after other ligand exchanges [1, 2]; however, these studies do not report a shorter lifetime, such as τ_2 , which corresponds to the AR of untreated samples. An unsuccessful ligand exchange would result in an AR time similar to τ_2 , suggesting that $\tau_{2'}$ arises from dot aggregates. This implies that ligand exchange procedures of bulky organics for shorter ones are not as reproducible as they must be to provide consistent thin films that can be used in photovoltaic devices, but alternatively, this lifetime may exist but not be observed in other studies because of non-degenerate pump-probe techniques which complicate results by differences in the absorption cross-section at the pump and probe wavelengths and pulse attenuation.

3.5 References

- [1] M. C. Beard, A. G. Midgett, M. Law, O. E. Semonin, R. J. Ellingson, and A. J. Nozik, “Variations in the quantum efficiency of multiple exciton generation for a series of chemically treated PbSe nanocrystal films,” Nano Letters, vol. 9, no. 2, pp. 836–845, 2009.
- [2] J. M. Luther, M. C. Beard, Q. Song, M. Law, R. J. Ellingson, and A. J. Nozik, “Multiple exciton generation in films of electronically coupled PbSe quantum dots,” Nano Letters, vol. 7, no. 6, pp. 1779–1784, 2007.
- [3] J. Tang, K. W. Kemp, S. Hoogland, K. S. Jeong, H. Liu, L. Levina, M. Furukawa, X. Wang, R. Debnath, D. Cha, et al., “Colloidal-quantum-dot photovoltaics using atomic-ligand passivation,” Nature materials, vol. 10, no. 10, pp. 765–771, 2011.
- [4] W. A. Tisdale, K. J. Williams, B. A. Timp, D. J. Norris, E. S. Aydil, and X.-Y. Zhu, “Hot-electron transfer from semiconductor nanocrystals,” Science, vol. 328, no. 5985, pp. 1543–1547, 2010.
- [5] A. P. Spencer, R. J. Hill, W. K. Peters, D. Baranov, B. Cho, and D. M. Jonas, “Probed-volume sample renewal by beam scanning with applications to noncollinear pump-probe spectroscopy at kilohertz repetition rates,” (in preparation), 2014.
- [6] I. Moreels, K. Lambert, D. Smeets, D. De Muynck, T. Nollet, J. C. Martins, F. Vanhaecke, A. Vantomme, C. Delerue, G. Allan, et al., “Size-dependent optical properties of colloidal PbS quantum dots,” ACS Nano, vol. 3, no. 10, pp. 3023–3030, 2009.
- [7] J. M. Luther, M. Law, Q. Song, C. L. Perkins, M. C. Beard, and A. J. Nozik, “Structural, optical, and electrical properties of self-assembled films of PbSe nanocrystals treated with 1, 2-ethanedithiol,” ACS Nano, vol. 2, no. 2, pp. 271–280, 2008.
- [8] L. Bakueva, S. Musikhin, M. Hines, T.-W. Chang, M. Tzolov, G. Scholes, and E. Sargent, “Size-tunable infrared (1000–1600 nm) electroluminescence from PbS quantum-dot nanocrystals in a semiconducting polymer,” Applied Physics Letters, vol. 82, no. 17, pp. 2895–2897, 2003.
- [9] J. Tang, L. Brzozowski, D. A. R. Barkhouse, X. Wang, R. Debnath, R. Wolowiec, E. Palmiano, L. Levina, A. G. Pattantyus-Abraham, D. Jamakosmanovic, et al., “Quantum dot photovoltaics in the extreme quantum confinement regime: the surface-chemical origins of exceptional air-and light-stability,” ACS Nano, vol. 4, no. 2, pp. 869–878, 2010.
- [10] T.-W. F. Chang, S. Musikhin, L. Bakueva, L. Levina, M. A. Hines, P. W. Cyr, and E. H. Sargent, “Efficient excitation transfer from polymer to nanocrystals,” Applied physics letters, vol. 84, no. 21, pp. 4295–4297, 2004.
- [11] H. Döllefeld, H. Weller, and A. Eychmüller, “Semiconductor nanocrystal assemblies: experimental pitfalls and a simple model of particle-particle interaction,” The Journal of Physical Chemistry B, vol. 106, no. 22, pp. 5604–5608, 2002.
- [12] C. Leatherdale and M. Bawendi, “Observation of solvatochromism in CdSe colloidal quantum dots,” Physical Review B, vol. 63, no. 16, p. 165315, 2001.
- [13] P. Guyot-Sionnest, “Electrical transport in colloidal quantum dot films,” The Journal of Physical Chemistry Letters, vol. 3, no. 9, pp. 1169–1175, 2012.

- [14] Z. Wang, C. Schliehe, K. Bian, D. Dale, W. A. Bassett, T. Hanrath, C. Klinke, and H. Weller, “Correlating superlattice polymorphs to internanoparticle distance, packing density, and surface lattice in assemblies of PbS nanoparticles,” Nano Letters, vol. 13, no. 3, pp. 1303–1311, 2013.
- [15] V. I. Klimov, “Spectral and dynamical properties of multiexcitons in semiconductor nanocrystals,” Annual Review of Physical Chemistry, vol. 58, pp. 635–673, 2007.
- [16] I. Robel, R. Gresback, U. Kortshagen, R. D. Schaller, and V. I. Klimov, “Universal size-dependent trend in auger recombination in direct-gap and indirect-gap semiconductor nanocrystals,” Physical Review Letters, vol. 102, no. 17, p. 177404, 2009.
- [17] L. A. Padilha, J. T. Stewart, R. L. Sandberg, W. K. Bae, W.-K. Koh, J. M. Pietryga, and V. I. Klimov, “Carrier multiplication in semiconductor nanocrystals: Influence of size, shape, and composition,” Accounts of Chemical Research, 2013.
- [18] L. A. Padilha, J. T. Stewart, R. L. Sandberg, W. K. Bae, W.-K. Koh, J. M. Pietryga, and V. I. Klimov, “Aspect ratio dependence of auger recombination and carrier multiplication in PbSe nanorods,” Nano Letters, vol. 13, no. 3, pp. 1092–1099, 2013.

Chapter 4

High energy transitions in Lead Sulfide Quantum Dots

4.1 Introduction

Bulk lead sulfide is well studied [1, 2] and transitions taken from the bulk band diagram (Figure 4.1) [2] are assigned to peaks in quantum dot (QD) linear absorption spectra. PbS QDs are reported to be bulk-like beginning around the E_2 transition or 3.1eV (400nm) [3] while at lower energy, near the band gap (labeled E_g in QDs but E_0 in bulk), strong confinement effects are present as demonstrated by the increase in the absorption peak energy with decreasing size. Likewise, the E_1 transition peak moves to higher energies as the size of the dot decreases but less quickly than E_g . For example, the E_1 transition shifts from 2.0eV in 8nm diameter PbS to 2.5eV in 2nm PbS while E_g increases from 0.69eV to 1.5eV in these same dots.

The E_1 peak also exists near the excitation wavelength of many multiple exciton generation (MEG) experiments, but these experiments probe at the band gap, or at least well red of E_1 . When probing at E_g , a ground state bleach is both expected and observed, as shown in data presented in Chapter 2. Experiments discussed in this chapter make use of degenerate ultrafast visible pump and probe pulses to examine the high energy area around the E_1 transition, where the signal is expected to reflect a mixture of excited state absorption (ESA) and excited state emission (ESE), but no significant contribution from ground state bleach (GSB). In addition, linear absorption spectra of several different sizes of PbS QDs are fit and analyzed based on both the 2nd derivative and the original spectra to examine higher energy transitions.

4.2 Experimental Procedure

4.2.1 Sample Preparation

Lead sulfide quantum dots were purchased from Evident Technologies and Voxel Inc. QDs from Voxel had first exciton peaks at 820nm, 870nm and 898nm with diameters of 1.9nm, 2.3nm, and 2.5nm, respectively, and were dispersed in hexanes. QDs from Evident had first exciton peaks at 1168nm, 1434nm, and 1800nm with diameters of 4.3nm, 5.2nm, and 7.8nm, respectively, and were dispersed in toluene. Samples were diluted as needed with anhydrous 99.8% toluene and $\geq 99\%$ hexane (purchased from Sigma Aldrich) but air free conditions were not maintained during sample handling and data collection unless specifically noted.

Smaller QDs, 1.6nm diameter PbS ($E_g=758\text{nm}$), were also studied. The synthesis for these dots was adapted from published procedures [4, 5] and personal correspondence with Dr. Joseph Luther at NREL. Lead(II) oxide, technical grade (90%) oleic acid (OA), and technical grade (90%) 1-octadecene (ODE) were purchased from Sigma Aldrich and stored in atmosphere. Ethanol (200 proof) was purchased from Decon Laboratories, Inc. and degassed on the Schlenk line by bubbling argon through it for eight hours before placing it in the glovebox. 3\AA molecular sieves (alumina silicate) were purchased from Mallinckrodt Chemicals and added to the ethanol in the glovebox to absorb remaining water.

Bis(trimethylsilyl)sulfide (TMS_2S) was also purchased from Sigma Aldrich and shipped with a Sure/SealTM cap to maintain air free conditions. The TMS_2S was stored in the glovebox upon receipt. Approximately 50mL of ODE was degassed by bubbling argon through on the Schlenk line for several hours. This aliquot was stored in the glovebox for later use as a solvent for TMS_2S . Anhydrous hexane was similarly degassed and stored in the glovebox.

0.461g of PbO, 1.232g OA, and 10.13g ODE were placed in a two-neck flask with a stir bar, which was then sealed and placed under vacuum on the Schlenk line. Argon was bubbled through and alternated with vacuum over a period of approximately 30 minutes. The reaction mixture was then kept under flowing Ar for the duration of the synthesis procedure. A heating mantle was used

to heat the reaction mixture to 150°C while stirring and kept at this heat for approximately one hour.

The reaction mixture was allowed to cool to 65°C and 135 μ L of TMS₂S in 2mL of ODE from the glovebox was injected into the flask. The reaction was allowed to proceed for 25 seconds and then the heating mantle was quickly removed and replaced with a room temperature water bath to quench the reaction. Approximately 20mL of hexane from the glovebox was added and the solution was cannulated into a purged filter flask that contained ethanol, a non-solvent, to precipitate the dots. The solution was then filtered, leaving the precipitated QDs in the flask. Hexane was cannulated into the flask to re-disperse the QDs and the process was repeated before transferring the flask containing QDs dispersed in hexane into the glovebox. This concentrated solution of QDs was stored in the glovebox to be diluted based on optical density as needed.

4.2.2 Characterization

Linear absorption spectra were provided for QDs purchased from Voxel and Evident but additional spectra of all samples were taken using a Varian Cary 500 UV-VIS-NIR Spectrophotometer and are shown in Figure 4.2. Images of samples were taken with a 300kV Phillips CM30 Transmission Electron Microscope (TEM) (system resolution is 2.3Å) with the help of Dr. Joseph Luther at the National Renewable Energy Laboratory and are shown in Figure 4.3.

4.2.3 Spectroscopic Measurements

Degenerate pump-probe data was taken on the QDs purchased from Evident (4.3nm, 5.2nm, and 7.8nm diameters) at varying wavelengths around the E_1 transition. Sub-25fs pulses were generated from a home-built visible non-collinear optical parametric amplifier (NOPA), pumped by a 50fs 800nm regenerative amplifier (Coherent RegA) at a 10kHz repetition rate. Samples were refreshed using a spinning sample cell so that a particular volume of the sample was excited less often than every 33ms. The excitation probability, $\langle N \rangle$, was kept below 0.1 to limit the probability of a QD absorbing more than a single photon. As mentioned in Chapter 2, degenerate

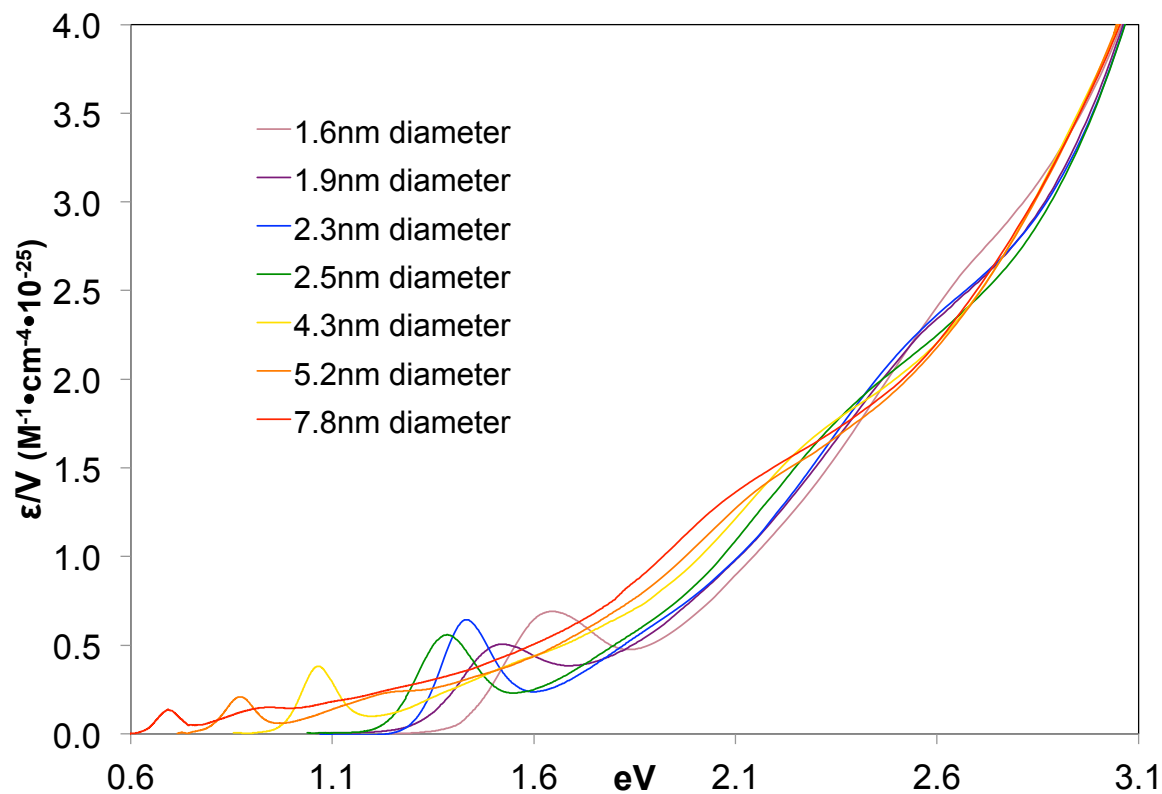


Figure 4.2: Linear absorption spectra of oleate-capped PbS QDs synthesized in the lab (1.6nm), purchased from Voxel Inc. (1.9, 2.3, and 2.5nm), and purchased from Evident Technologies (4.3, 5.2, 7.8nm). The molar extinction coefficient ϵ ($M^{-1}cm^{-1}$) on the y-axis is divided by the nanocrystal volume in this figure to enable a direct comparison of spectra.

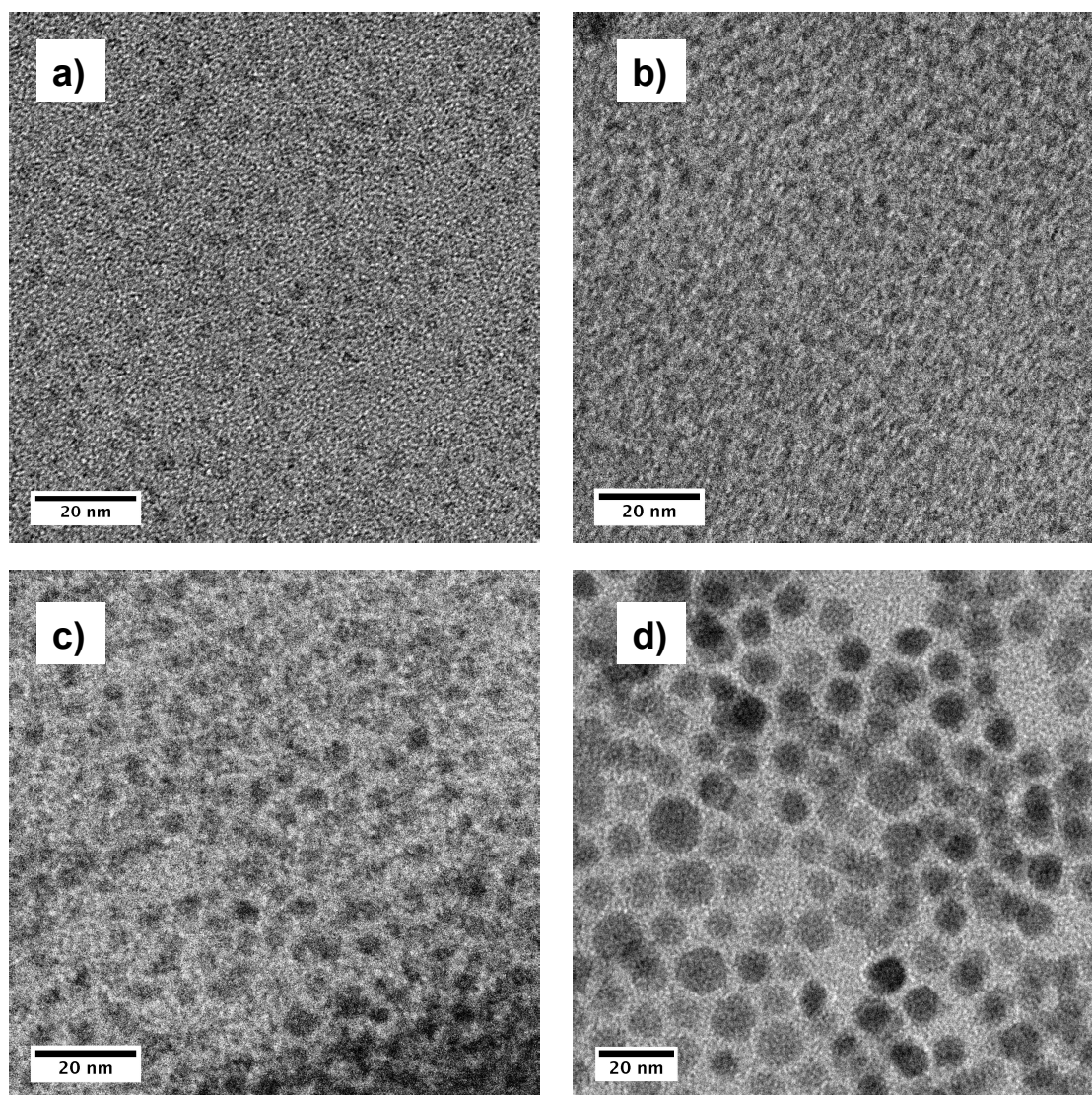


Figure 4.3: Images taken at NREL with a Phillips CM30 TEM with the assistance of Dr. Joseph Luther. a) 1.9nm diameter PbS from Voxel, b) 2.5nm diameter PbS from Voxel, c) 4.3nm diameter PbS from Evident, and d) 7.8nm PbS from Evident.

pump-probe ensures that frequency-dependent variations in the absorption cross-section do not complicate the pump-probe signal or subsequent analysis.

4.3 Results & Discussion

Figures 4.4, 4.5, and 4.6 show the degenerate pump-probe transients of the three sizes of PbS QDs, taken with the pulse spectrum centered at different excitation wavelengths. An initial negative signal is indicative of excited state absorption (ESA) at each of the wavelengths, indicating that at these early times and low $\langle N \rangle$, carriers already excited by the pump are more likely to be excited to a higher electronic state by the probe than undergo stimulated emission back down to the ground electronic state.

As seen in Figures 4.4-4.6, excited state absorption is the predominant feature at each wavelength, but a short-lived positive signal (bleach) occurs when pumping and probing at 610nm (2.03eV), 570nm (2.18eV), and 550nm (2.26eV) for 7.8nm, 5.3nm, and 4.2nm dots, respectively. A bleach can arise from depletion of absorption by the ground state, ground state bleach (GSB), or from stimulated emission by the excited state, excited state emission (ESE). In addition, ESA begins to quench more rapidly over time (within 1.5ps) when the pump-probe wavelength is shorter than that of the E_1 transition ($\lambda < E_1$). This is seen most clearly in Figure 4.6 when the pump and probe are tuned to 507nm.

The short-lived bleach occurs at a different wavelength for each size of QD, but in each case the wavelength closely corresponds to the peak of the E_1 transition in the respective linear absorption spectrum.

The conduction and valence bands in Figure 4.1 can be numbered, beginning with the lowest lying VB, from one (1) to ten (10), increasing in number with increasing energy; therefore the E_0 transition occurs from band 5 to band 6 at the L -point.

The E_1 transition is usually labeled as occurring at the Σ -point from band 5 to band 6 in the bulk diagram, as in Figure 4.1, but some early reports attribute the E_1 peak to either the $L_6^+ \rightarrow L_6^-$ transition, from band 5 to band 7 [6], (dashed arrow near E_0 in Figure 4.1) or a combination

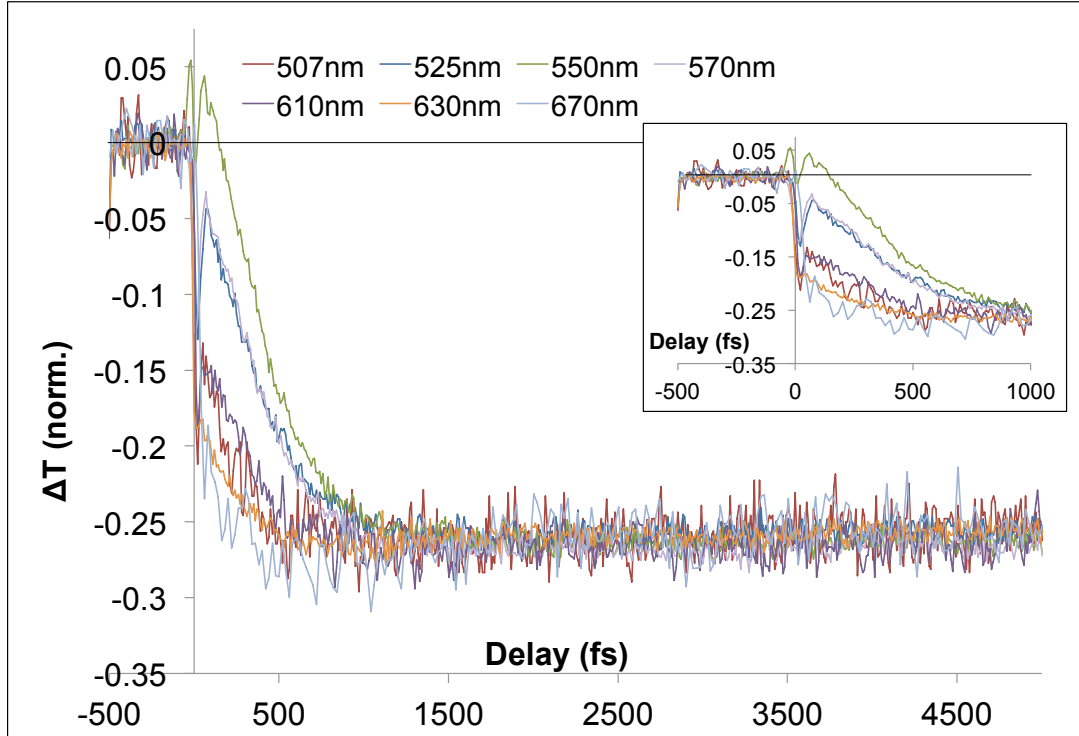


Figure 4.4: Degenerate pump-probe transients, taken with the pulse spectrum centered at different wavelengths, for the 4.3nm PbS QDs purchased from Evident ($E_g = 1168\text{nm}$ and $E_1 = 556\text{nm}$). ESA is the predominate feature at all of the wavelengths but a short-lived, early-time positive signal is seen for at 550nm which indicates GSB. The inset shows the GSB at around 100fs for $\lambda_{p-p} = 550\text{nm}$.

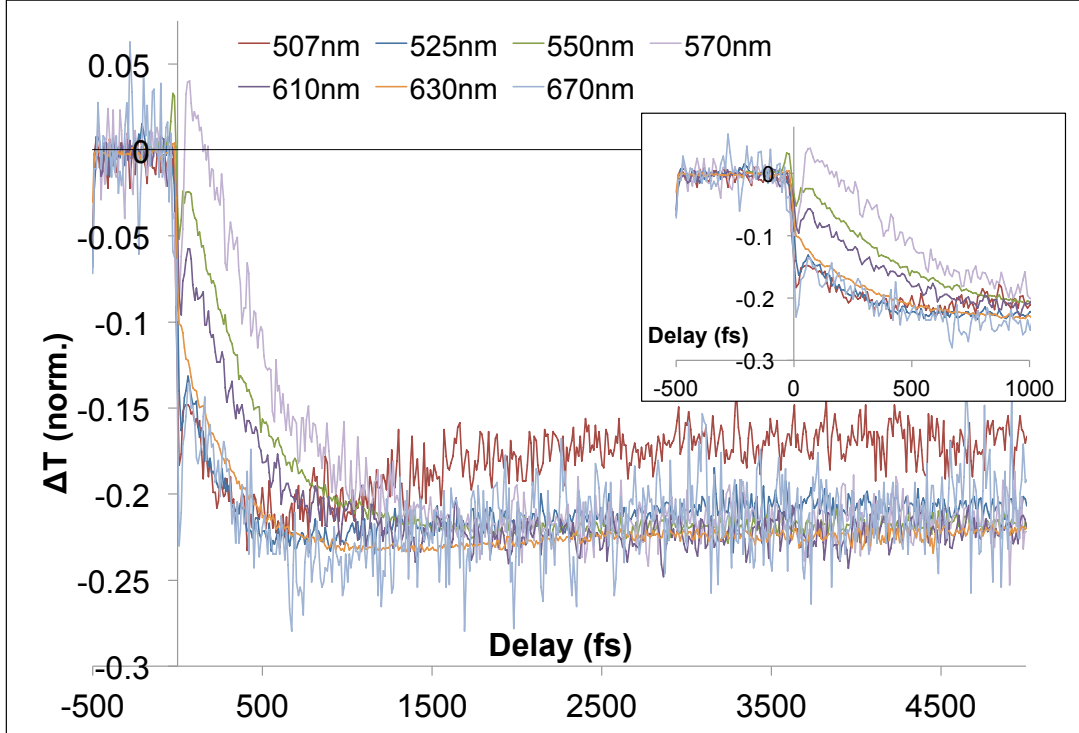


Figure 4.5: Degenerate pump-probe transients, taken with the pulse spectrum centered at different wavelengths, for the 5.2nm PbS QDs purchased from Evident ($E_g = 1434\text{nm}$ and $E_1 = 584\text{nm}$). As in Figure 4.4, ESA dominates each transient but an early, short-lived bleach is seen with $\lambda_{p-p} = 570\text{nm}$, again, near the center of the E_1 transition for this size of QD. Additionally, $\lambda_{p-p} = 507\text{nm}$ shows an increased decay toward zero, compared to other transients, beginning around 500fs. The inset shows GSB around 100fs for $\lambda_p - p = 570\text{nm}$.

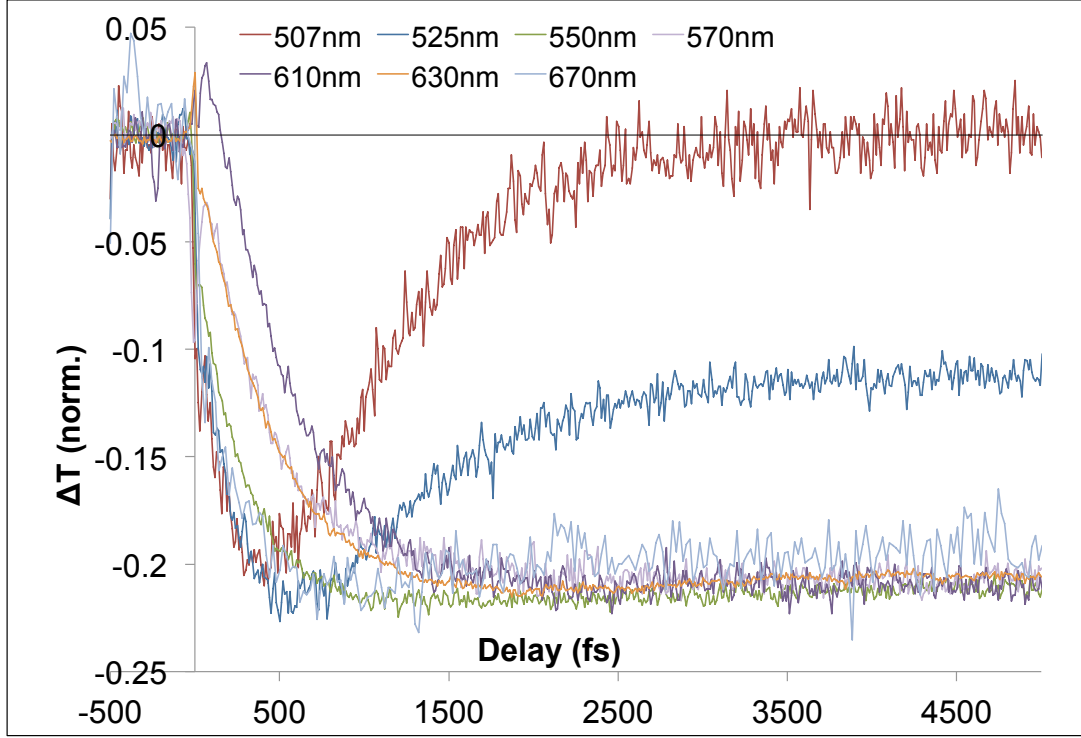


Figure 4.6: Degenerate pump-probe transients, taken with the pulse spectrum centered at different wavelengths, for the 7.8nm PbS QDs purchased from Evident ($E_g = 1800\text{nm}$ and $E_1 = 610\text{nm}$). Similar to transients of 4.3nm and 5.2nm QDs, the 7.8nm QDs show increasing ESA at early times ($< 500\text{fs}$) for all λ_{p-p} except that near the E_1 peak, $\lambda_{p-p} = 610\text{nm}$. Like the 5.2nm QD transients with $\lambda_{p-p} = 507\text{nm}$, there is a decay toward zero beginning around 500fs, but in this case it is much larger and reaches zero by 3ps. Additionally, a lesser rise is seen with $\lambda_{p-p} = 525\text{nm}$.

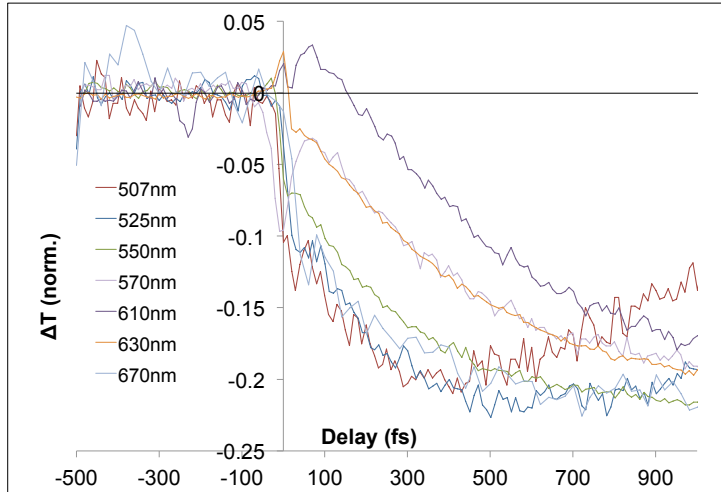


Figure 4.7: The first 1ps of transients, taken with the pulse spectrum centered at different wavelengths, for the 7.8nm PbS QDs (Figure 4.6) is shown. GSB is observed around 100fs at $\lambda_{p-p} = 610\text{nm}$.

of the $\Sigma_5 \rightarrow \Sigma_5$, band 5 to band 6 (labeled E_1 in Figure 4.1), and $L_6^+ \rightarrow L_6^-$, band 5 to band 7, transitions [2, 7]. These assignments are taken into account in analysis of the transients and linear absorption spectra.

4.3.1 Degenerate Pump-probe Signals

4.3.1.1 $\lambda_{p-p} > E_1$

Considering the transients taken when wavelength of the pump and probe pulses is greater than that of the E_1 transition ($\lambda > E_1$), signal contributions may initially come from GSB, ESE, and ESA, at $T \ll 1\text{ps}$ (within the first hundreds of femtoseconds). These processes are illustrated in Figure 4.8. As the time-delay of the probe pulse increases, the contribution from ESA remains while contributions from ESE decrease as electrons and holes cool to the conduction and valence band edges. Cooling to the band edge normally occurs well within the first couple of picoseconds. [8]

Although early contributions from ground state bleach are expected, which would be at a maximum when carriers have not yet relaxed to the band edges, ESA dominates the pump-probe signal. As a pump-excited electron relaxes to the edge of the conduction band, the absorption spectrum red-shifts, allowing the probe to more easily excite a second electron, which means the probe can excite an electron from the valence band to the conduction band, producing a second electron-hole pair via two-particle ESA.

4.3.1.2 $\lambda_{p-p} \approx E_1$

The transients that result for each dot when the wavelength is approximately equal to the peak of the E_1 transition ($\lambda \approx E_1$) show a short-lived bleach around 100fs. At these excitation energies, similar contributions from ESA and ESE may be expected at early times but now an additional contribution from GSB, compared to $\lambda > E_1$ (shown in Figure 4.9), is present. Linear absorption spectra suggest that although a discrete transition exists for E_1 , it lies atop a bulk-like continuum so $\lambda < E_1$ and wavelengths corresponding to the E_1 transition can access higher-lying conduction bands at the L -point, such as the $L_6^+ \rightarrow L_6^-$ transition (band 5 to band 7) shown in

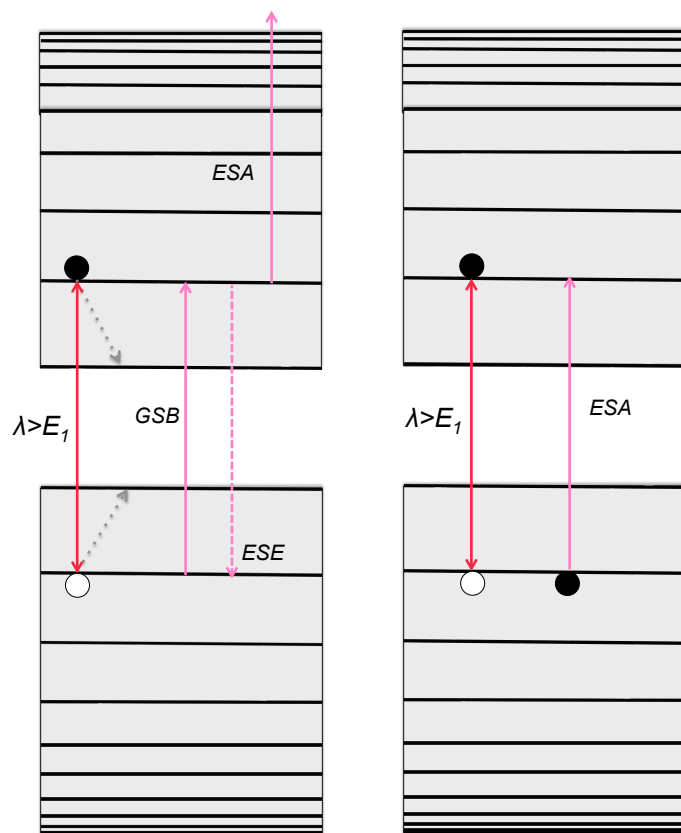


Figure 4.8: Approximations of the L -point electronic energy levels are shown. A photon with $\lambda > E_1$ only contains enough energy to excite an electron from the L -point VB to the lowest lying L -point CB. The initial pump pulse (red) excites an electron and the subsequent probe pulse (pink) may experience GSB, ESE (dashed), or ESA arising from the same electron and hole (left). Electrons and holes may also relax to the edges of the CB and VB, respectively, usually within a few hundred femtoseconds (gray dashed arrows). It is also possible for the excitation of one electron-hole pair to affect the excitation of another carrier, generating a two-particle ESA pump-probe signal (right).

Figure 4.1 with a dashed arrow. With $\lambda \approx E_1$, photon energy is great enough for a bleach to occur at either the L - or Σ - point, but likely is mainly due to the quantum confined electronic energy levels at the Σ -point. The closely spaced levels arising from the L -point allow carriers to quickly cool to a lower energy level, so that no bleach is seen in the transients above or below E_1 , indicating the influence of the bulk band structure; however, ESA contribution remains with increasing time-delay of the probe and quickly dominates over the decreasing GSB.

4.3.1.3 $\lambda_{p-p} < E_1$

Transients of the 7.8nm PbS QDs (Figure 4.6) at $\lambda_{p-p} = 525\text{nm}$ and 507nm ($\lambda < E_1$) exhibit a decay in signal magnitude after the first picosecond not seen at longer wavelengths, suggesting loss mechanisms for these higher energy carriers. At this short wavelength, there are noticeable differences between transients for the different sizes of QDs.

While the 7.8nm diameter PbS QD transients for $\lambda_{p-p} = 507\text{nm}$ and 525nm reflect different amounts of quenching, there is no difference between transients at these wavelengths and longer wavelengths for the 4.3nm QD sample. This may be explained by the greater excess electronic energy available due to the smaller band gap of the larger, 7.8nm, QD. All three QD samples experience excitation at the L -point from band 5 to band 7, but a more strongly quantum confined, smaller sized dot will have less excess energy available for the same photon energy. Processes for $\lambda < E_1$ are illustrated in Figure 4.10.

4.4 Linear Absorption Analysis

To further explore contributions to the E_1 transition, linear absorption spectra are analyzed. If some previous assignments are correct [2, 6, 7], then E_1 in the linear absorption spectra should reflect contributions from the two transitions at the L - and Σ - points. If quantum confined, the peak energies of these transitions and the oscillator strengths will change with changing QD size.

Linear absorption spectra of each sample were taken at various concentrations in order to maintain peak resolution in all regions of a spectrum without saturating the detector. Spectra were

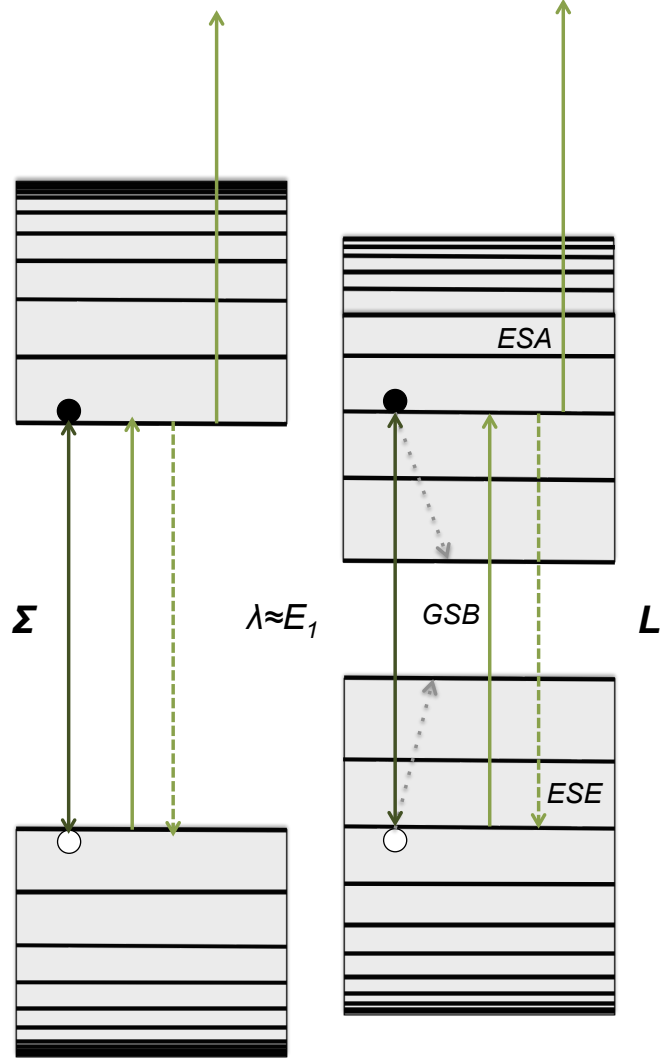


Figure 4.9: A similar picture of the Σ^- - (left) and L - (right) points are shown as in Figure 4.8, but a photon with $\lambda \approx E_1$ now has enough energy to excite an electron at either point. The initial pump pulse (dark green) may excite an electron at either the L -point or the Σ^- -point. The subsequent probe pulse (light green) may experience GSB, ESE (dashed), or ESA (solid). Again the dashed, gray arrows represent electron and hole cooling to the band edges. As in Figure 4.8, two-particle ESA signals are possible, but not shown here.

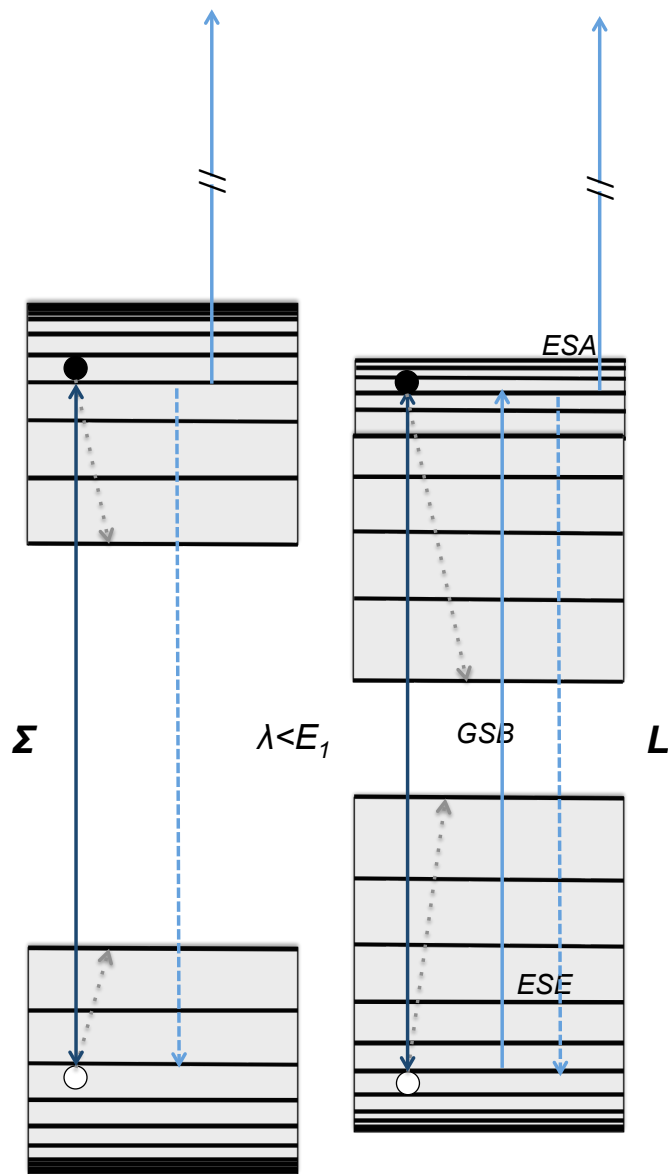


Figure 4.10: Similar to Figure 4.9, a pump photon with $\lambda < E_1$ (dark blue) has enough energy to excite an electron at either the L -point or Σ - point. The subsequent probe pulse (light blue) may experience GSB, ESE (dashed), or ESA (solid). Again the dashed, gray arrows represent electron and hole cooling to the band edges and as in Figure 4.8, two-particle ESA signals are possible, but not shown here.

then normalized at 400nm, where absorbance per mass concentration is equal to 0.93: [9]

$$\frac{A_{400nm}}{mg/mL} = 0.93 \quad (4.1)$$

and ‘spliced’ together at wavelengths that maintained peak resolution but were not near any prominent transition peaks. These spectra were further divided by the sample path length and the molecular weight of the respective quantum dot, calculated based on QD size and density, to obtain the molar extinction coefficients, ε ($M^{-1}cm^{-1}$).

Absorption spectra were obtained for seven sizes of PbS QDs, all capped with oleate ligands, and plotted as the frequency-divided molar extinction coefficient, $\frac{\varepsilon(\nu)}{\nu}$, versus frequency (in eV). The second derivatives were calculated and are shown overlaid with the absorption spectra for two sizes of QDs (2.5nm and 7.8nm) in Figures 4.11 and 4.12. The fits and analysis of these spectra are discussed below, and the linear absorption spectra and second derivatives for other sizes of QDs are shown in the Appendix.

Before fitting the absorption spectra, second derivatives were fit based on a third order polynomial background and a sum of Gaussians with approximate peak positions based on second derivative minima. These initial fit parameters were used to fit the linear absorption spectrum while the third order polynomial background was allowed to change. Once the best fit background was found, the Gaussian transition parameters, coefficient, peak energy, and full-width at half maximum (FWHM), were floated.

To consider the possibility of multiple transitions occurring at E_1 , a second fit was found for each spectrum in the same way but allowing two Gaussians at E_1 , shown in Figure 4.11 and 4.12. Allowing two transitions to occur at E_1 results in little difference to the linear absorption fit and lower energies of the second derivative, but improves the fit around E_1 and at higher energies of the 2nd derivative.

The FWHM of the single E_1 Gaussians found for the linear spectra are plotted against QD diameter in Figure 4.13 a). It is possible that the data for small dots show an increase of the FWHM with increasing QD size up to 2.3nm diameter with a subsequent decrease, but this is

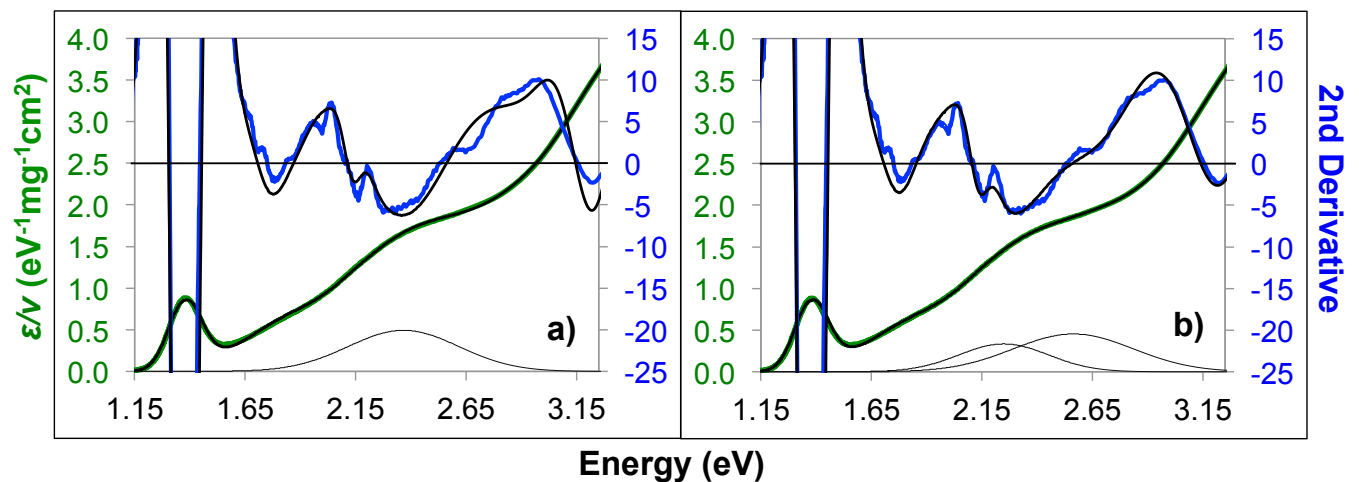


Figure 4.11: Absorption spectra of 2.5nm diameter PbS QDs are shown in green with the second derivative in blue. Fits to absorption spectra and the second derivative are overlaid in black. **a** is the fit using only a single Gaussian to fit the E_1 transition while **b** uses two Gaussians to fit the area around the E_1 transition. Only the Gaussians fit to E_1 transitions are shown under each absorption curve. While there is little difference between the fits at lower energies, the second derivative fit using two Gaussians at E_1 (**b**) accounts for the second derivative minimum at 2.65eV and allows a better fit for the minimum at 3.2eV compared to the fit with only a single Gaussian at the E_1 transition (**a**).

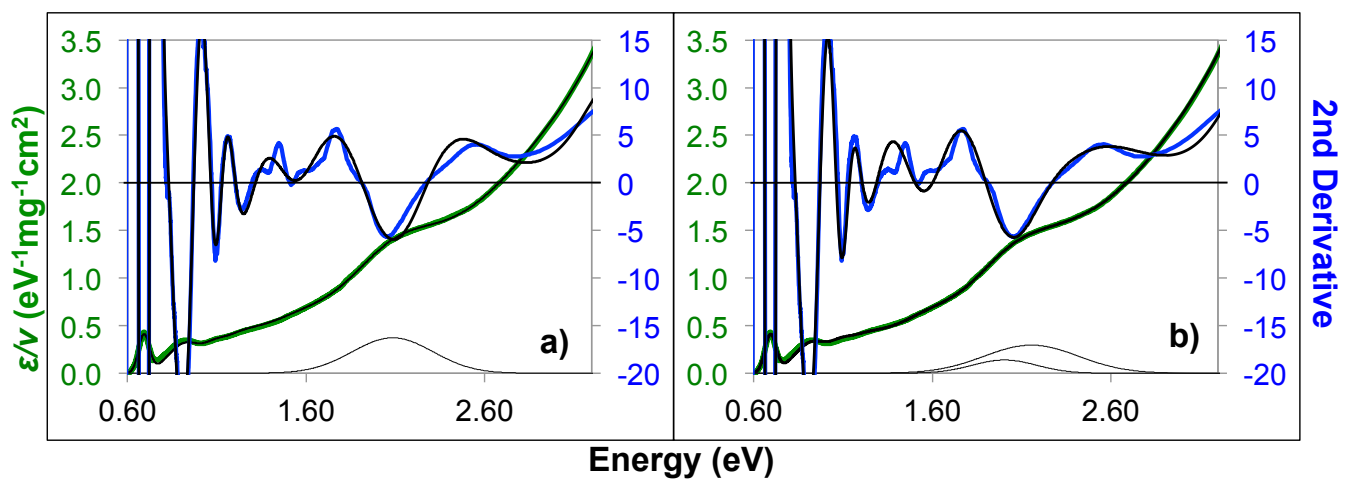


Figure 4.12: Absorption spectra of 7.8nm diameter PbS QDs are shown in green with the second derivative in blue. Fits to absorption spectra and the second derivative are overlaid in black. **a** is the fit using only a single Gaussian to fit the E_1 transition while **b** uses two Gaussians to fit the area around the E_1 transition. Only the Gaussians fit to E_1 transitions are shown under each absorption curve. Again, there is little difference between the fits at lower energies, but the second derivative fit using two Gaussians at E_1 (**b**) better accounts for the shoulders seen around 2.3eV and 2.8eV when compared to the fit with only a single Gaussian at the E_1 transition (**a**).

uncertain. This would suggest changes of the individual Σ - and L - point quantum dot band gaps that each contribute to E_1 but are not separately discernible. Comparing this trend with that of E_g (Figure 4.13) shows that the FWHM of a single band gap transition is expected to increase with decreasing QD diameter. What is certain is that the E_1 transition is much wider than the FWHM of the single transition at the lowest band gap. The E_1 width is also very much less sensitive to size than the width of the lowest band gap transition. Based on Figure 4.1, this would be expected from the effective mass theory of quantum confinement.

Using Einstein coefficients, the frequency-integrated molar extinction coefficient is found to be proportional to the oscillator strength of a transition:

$$\int \frac{\varepsilon(\nu)}{\nu} \propto f_{if} \quad (4.2)$$

where i and f are the initial and final states of the transition. Using this relationship, the trend of the oscillator strength of a particular transition for different sizes of QDs can be found.

The integrated area of the Gaussian fit to each E_1 peak (both for single and two Gaussian E_1 fits) is calculated and plotted against the volume of the corresponding QD in Figure 4.13 b). For the second set of fits that includes two Gaussians around the E_1 transition, the sum of the two f_{if} are shown to agree well with the individual values for the single Gaussian fits. The exact contribution of each transition (Σ and L) is difficult to determine, but the oscillator strength per QD of both transitions decreases as the size of the dot decreases.

4.5 Conclusion

Degenerate pump-probe transients at varying wavelengths around the E_1 transition of three sizes of PbS QDs show a contribution from GSB at early times when excited near the center of the E_1 peak and show fast quenching at shorter wavelengths, which suggest additional loss mechanisms. Linear absorption spectra and second derivatives of seven different sizes of PbS QDs imply contributions at the E_1 transition from two points in the band structure, L and Σ , which vary as the size of the dot decreases.

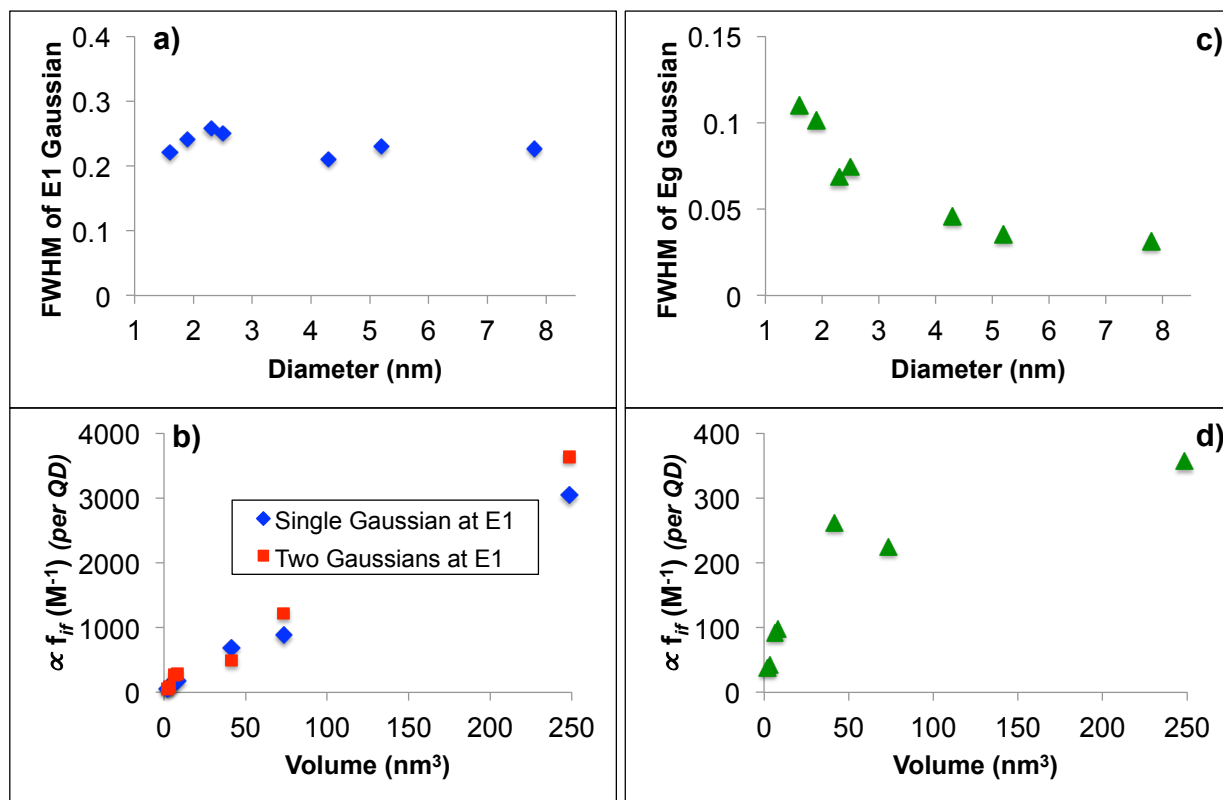


Figure 4.13: **a)** Full width at the half maximum (FWHM) of the single Gaussian fit for the E_1 transition versus the QD diameter (nm). **b)** The y-axis is proportional to the oscillator strength (f_{if}) of the E_1 transition and the x-axis is the volume (nm^3) of the QD. Blue diamonds represent f_{if} for the single Gaussian fit to the E_1 transition while red squares are the sum of f_{if} for the fit with two Gaussians at the E_1 transition. Similar comparisons are shown using the energy of the E_1 peak, instead of QD size, in the Appendix. **c) & d)** The same plots that are described for **a** and **b** are shown here for E_g to illustrate trends for a band gap transition, but it should be noted that the first exciton peaks of the smallest size of QDs likely contain contributions from other transitions that overlap as it blue-shifts.

The short-lived bleach that appears in each transient at the respective wavelength of the E_1 transition of each QD implies that some confinement effects are present, but overwhelming ESA at other wavelengths indicate a strong bulk-like background that dominates most carrier dynamics. In addition, the insensitivity of the FWHM of the E_1 transition, shown in Figure 4.13 a), implies considerable bulk-like behavior beginning as early as E_1 rather than at the higher energy transition, E_2 ; however, the trend in oscillator strength for this transition, shown in Figure 4.13 b), illustrates an increase in f_{if} with increasing QD size. A size-dependent increase of f_{if} per absorbing unit indicates confinement but at the E_1 transition, it is unclear if the entire QD or each PbS should be considered the absorber. In this case, the oscillator trend is shown per QD rather than PbS unit but may be more accurate if the smaller unit is considered the absorber.

These results suggest that even in quantum confined PbS nanocrystals, both bulk band structure and quantum confinement may play a role at energies corresponding to the E_1 peak and at higher energies. The photophysics at this transition are complicated by contributions from both bulk and quantum pictures and require additional investigations to gain a better understanding of the fundamental mechanisms that occur and may play a role in quantum dots with a carrier multiplication threshold, $3E_g$, at E_1 .

4.6 References

- [1] M. Cardona and D. L. Greenaway, “Optical properties and band structure of group IV-VI and group V materials,” Physical Review, vol. 133, no. 6A, p. A1685, 1964.
- [2] S. Kohn, P. Yu, Y. Petroff, Y. Shen, Y. Tsang, and M. Cohen, “Electronic band structure and optical properties of PbTe, PbSe, and PbS,” Physical Review B, vol. 8, pp. 1477–1488, 1973.
- [3] I. Moreels, G. Allan, B. De Geyter, L. Wirtz, C. Delerue, and Z. Hens, “Dielectric function of colloidal lead chalcogenide quantum dots obtained by a Kramers-Krönig analysis of the absorbance spectrum,” Physical Review B, vol. 81, no. 23, p. 235319, 2010.
- [4] C. B. Murray, S. Sun, W. Gaschler, H. DoyLe, T. A. Betley, and C. R. Kagan, “Colloidal synthesis of nanocrystals and nanocrystal superlattices,” IBM Journal of Research and Development, vol. 45, no. 1, pp. 47–56, 2001.
- [5] M. A. Hines and G. D. Scholes, “Colloidal PbS nanocrystals with size-tunable near-infrared emission: observation of post-synthesis self-narrowing of the particle size distribution,” Advanced Materials, vol. 15, no. 21, pp. 1844–1849, 2003.
- [6] P. J. Lin and L. Kleinman, “Energy bands of PbTe, PbSe, and PbS,” Physical Review, vol. 142, no. 2, p. 478, 1966.
- [7] F. Herman, R. L. Kortum, I. B. Ortenburger, and J. P. Van Dyke, “Relativistic band structure of GeTe, SnTe, PbTe, PbSe, and PbS,” Le Journal de Physique Colloques, vol. 29, no. C4, pp. C4–62, 1968.
- [8] I. Gdor, H. Sachs, A. Roitblat, D. B. Strasfeld, M. G. Bawendi, and S. Ruhman, “Exploring exciton relaxation and multiexciton generation in PbSe nanocrystals using hyperspectral near-ir probing,” Acs Nano, vol. 6, no. 4, pp. 3269–3277, 2012.
- [9] W. K. Peters and D. M. Jonas. personal communication, 2013.

Chapter 5

E_1 transition in Lead Sulfide Quantum Dots Treated with 1,2-Ethanedithiol

5.1 Introduction

As mentioned in Chapter 4, the E_1 transition appears in both bulk and quantum dot linear absorption spectra. It has bulk origins but experiences quantum confinement, as seen by its blue shift with decreasing QD size. It occurs near or at the carrier multiplication (CM) threshold of three times the band gap, $3E_g$, depending on the size of the dot, making it important to better understand carrier dynamics at this transition. As mentioned in Chapter 3, coupled arrays are precursors to potential photovoltaic devices and previous investigations of ligand-exchanged films pump at or near E_1 and probe at or near the band gap. [1,2]

I employ *degenerate* pump-probe spectroscopy to investigate this high energy transition in 4nm diameter lead sulfide quantum dots using the visible output of a non-colinear optical parametric amplifier (NOPA). With the band gap at 1158 nm, the E_1 transition (at 560 nm) corresponds to $2.1E_g$, less than the (CM) threshold for this size of dot. These preliminary experiments on a coupled array compared to a colloidal solution avoid complications from frequency-dependence of the absorption cross-section by pumping and probing at the same wavelength. In addition, I again make use of the beam scanning technique developed by others in the Jonas group to minimize effects of repeated photoexcitation of the sample over a short period of time. [3]

5.2 Experimental Procedure

5.2.1 Sample Preparation

The synthesis of 4.3nm diameter PbS ($E_g = 1158$) was adapted from published procedures [4, 5] and personal correspondence with Dr. Joseph Luther at NREL. Lead(II) oxide, technical grade (90%) oleic acid (OA), and technical grade (90%) 1-octadecene (ODE) were purchased from Sigma Aldrich and stored in atmosphere.

Bis(trimethylsilyl)sulfide (TMS_2S) was also purchased from Sigma Aldrich and shipped with a Sure/SealTM cap to maintain air free conditions. The TMS_2S was stored in the glovebox upon receipt. Approximately 50mL of ODE was degassed by bubbling argon through on the Schlenk line for several hours. This aliquot was stored in the glovebox for later use as a solvent for TMS_2S . Ethanol (200 proof) was purchased from Decon Laboratories, Inc. and degassed on the Schlenk line by bubbling argon through it for eight hours before being placed in the glovebox. 3Å molecular sieves (alumina silicate) were purchased from Mallinckrodt Chemicals and added to the ethanol in the glovebox to absorb remaining water. Anhydrous hexane was similarly degassed and stored in the glovebox.

0.23g of PbO, 3.88g OA, and 5.13g ODE were placed in a two-neck flask with a stir bar, which was then sealed and placed under vacuum on the Schlenk line. Argon was bubbled through and alternated with vacuum over a period of approximately 30 minutes. The reaction mixture was then kept under flowing Ar for the duration of the synthesis procedure. A heating mantle was used to heat the reaction mixture to 150°C while stirring and kept at this heat for approximately one hour.

The reaction mixture was allowed to cool to 101°C and 100μL of TMS_2S in 2mL of ODE from the glovebox was injected into the flask. The reaction was allowed to proceed for 25 seconds and then the heating mantle was quickly removed and replaced with a room temperature water bath to quench it. Approximately 20mL of hexane from the glovebox was added and the solution was transferred to the glovebox.

In the glovebox, the colloidal solution was added to ethanol, a non-solvent, to precipitate the dots. This solution was sealed, centrifuged to separate the QDs, and the ethanol-hexane mixture was decanted. The remaining solid QDs were re-dispersed in hexane and this ‘wash’ process was repeated. This concentrated solution of QDs was stored in the glovebox to be diluted based on optical density as needed.

Ligand exchange was performed by Dr. Jianbo Gao at the National Renewable Energy Laboratory using a dip coating apparatus. A 0.025-in thick hard disk glass substrate (2.56-in outer diameter and 0.79-in inner diameter) was dipped into a concentrated solution of the dots, 10mg/mL, and then dipped into a 1mM solution of EDT in acetonitrile. This process was repeated twenty times for a film thickness of around 200nm. One side of the substrate was cleaned with hexane to remove the film, leaving only one side coated.

Linear absorption spectra were taken using a Varian Cary 500 UV-VIS-NIR Spectrophotometer and are shown in Figure 5.1. Similar to previous reports [1, 2] and results in Chapter 3, EDT-treatment results in a red-shift of the first exciton peak and an offset of the absorption spectrum, which continues to decrease red of the band gap out to 2200nm. Previous reports attribute the shift to sintering of properly oriented particles spaced very closely [6]; an increase in dipole-dipole interactions between neighboring dots [7]; polarization effects caused by dielectric changes in the environment [8]; or a combination of increases in inter-dot radiative and electronic non-radiative coupling. [1] Some authors attribute the offset to scattering. [1, 2].

Airfree conditions were maintained as much as possible but due to limitations in space at the sample point in the pump-probe setup, the EDT-treated array could not be kept in the sealed sample cell and was exposed to atmosphere during data collection. The solution was kept in an airfree cuvette and both the solution and array were stored in the glovebox in between data collection. Exposure of the array to atmosphere caused a blue-shift of the first absorption peak, which has been observed previously [1, 9], from 1230nm to 1180nm. Although the higher energy area of the spectrum, which is of interest in this experiment, appears to maintain its shape (Figure 5.2), a second derivative analysis shows a shift of the center of the E_1 peak from 585nm to 560nm.

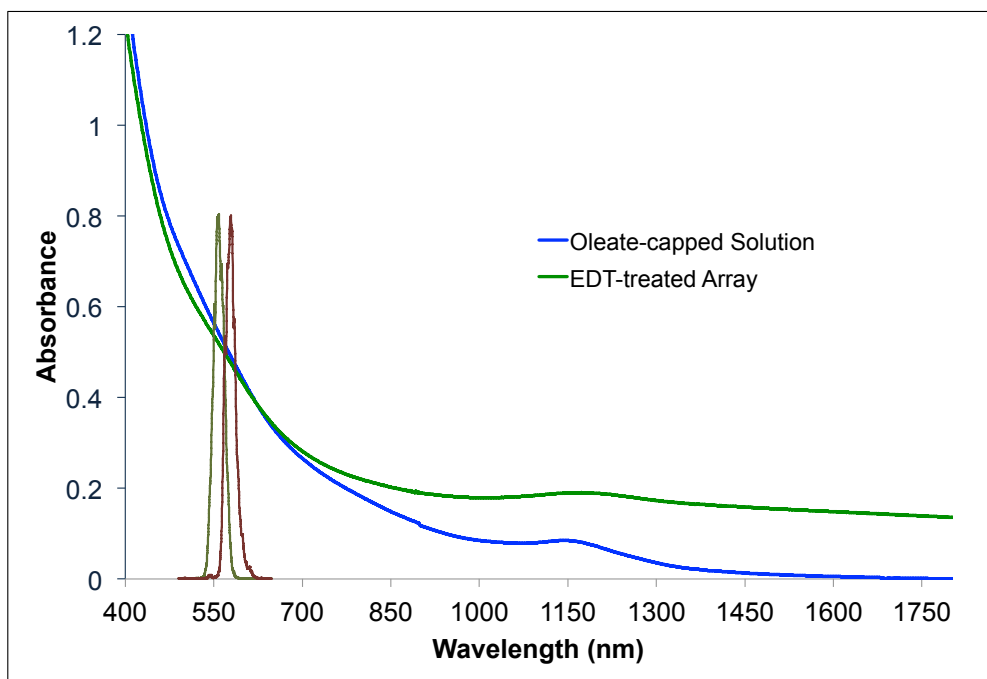


Figure 5.1: Linear absorption spectra of the oleate-capped PbS QD colloidal solution in hexane and the EDT-treated PbS array after exposure to atmosphere. The centers of the pulse spectra, which occur at 560nm and 570nm, used in the experiment are overlaid in green and red, respectively. Similar to previous reports [1,2] and results in Chapter 3, EDT-treatment results in an offset of the absorption spectrum and a red-shift of the first exciton peak, which is discussed further in the text.

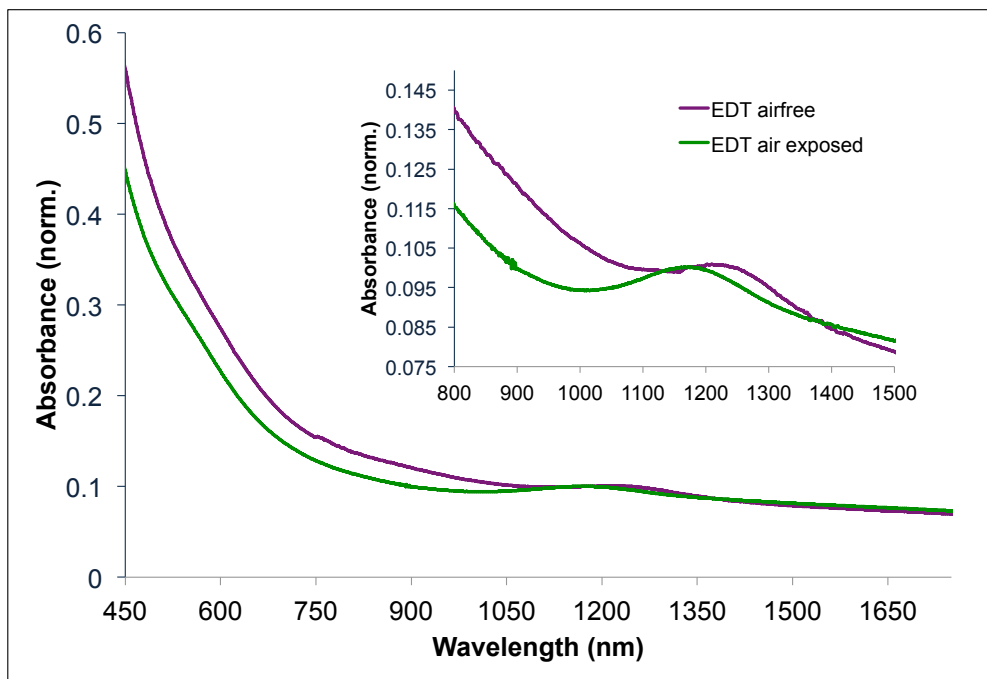


Figure 5.2: Linear absorption spectra of the EDT-treated film in air free conditions shortly after being deposited on the substrate (purple) and after being exposed to atmosphere during data collection (green). The overall shape of the spectrum at higher energies appears the same but includes a blue-shift of the E_1 transition from 585nm to 560nm. A more obvious shift is seen at longer wavelengths where the center of the first exciton peak changes from 1230nm to 1180nm.

5.2.2 Spectroscopic Measurements

Degenerate pump-probe transients on colloidal oleate-capped PbS in hexane and the EDT-treated array are recorded with the center of the pulse spectrum at 570nm, just red of the center of the E_1 transition which occurs at 560nm. Transients of the air-exposed array were also taken with the center of the pulse spectrum at 560nm, the center of the E_1 transition. Sub-30fs pulses were generated from a home-built visible non-collinear optical parametric amplifier (NOPA), pumped by a 100fs 800nm regenerative amplifier (Coherent RegA) at a 10kHz repetition rate. Samples were refreshed using the scanning beam technique mentioned in previous chapters so that a particular volume of the sample was excited less often than every 40ms. The probe was maintained around $9\mu\text{W}$ while the pump was varied at $50\mu\text{W}$ and $100\mu\text{W}$, resulting in probed volume weighted excitation probabilities, $\langle N \rangle$, of approximately 0.25 and 0.50. Lower pump powers were not used because of the low signal-to-noise from the array.

5.3 Results & Discussion

Similar to transients of colloidal solutions shown in Chapter 4, a long-lived negative signal is the predominant feature of the solution and array here, indicating excited state absorption (ESA). All transients show a decrease in negative amplitude over time but the transients of the array show an additional time component not seen in the solution. Figure 5.3 compares the solution and array transients at $\langle N \rangle \approx 0.25$, with the pulse spectrum centered at 570nm. Although the magnitude of the negative signal before 100ps is larger for the array compared to the solution, the transients converge around 200ps and remain in agreement out to 1ns.

A comparison of array transients at different $\langle N \rangle$, Figure 5.4-5.6, shows similar behavior, regardless of the excitation wavelength. All of the transients exhibit a negative signal, indicative of excited state absorption (ESA), that remains fairly constant after about 200ps; however, the transients taken with the pulse spectrum center tuned to 560nm also show a small bleach at very early times, within the first 200fs (Figure 5.6). This is within the temporal resolution of the pulse

(30fs) and appears to be a real feature, similar to the small ground state bleach observed in colloidal solutions when excited at the center of the E_1 transition shown in Chapter 4.

Poisson statistics are used with P_k as the probability of having k excitons per quantum dot:

$$P_k = \frac{\langle N \rangle^k}{k!} e^{-\langle N \rangle} \quad (5.1)$$

to find the ratio of mult-exciton signal to single exciton signal

$$\frac{\sum_{k=2}^{\infty} k P_k}{P_1} \quad (5.2)$$

and show that for each sample with $\langle N \rangle \approx 0.25$, there is 9.6% contamination to the signal from biexcitons and 3.1% contamination from triexcitons. Transients taken with $\langle N \rangle \approx 0.50$ have larger signal contribution from both bi- and tri-excitons, 50% and 12.5%, respectively, with approximately 2% from higher multiples of excitons.

A multi-exponential fit to the solution results in two constants: one at a lifetime attributed to single exciton decay; and one short time constant that is on the order of magnitude of the expected AR lifetime, which is discussed below. Fits to the array include the same short time constant as the solution, but also contain a lifetime of tens of picoseconds, that is attributed to AR. Coefficients and lifetimes are summarized in Table 5.1.

Robel, et al. [10] report a universal *effective* biexciton AR constant that indicates lifetimes on the order of tens of picoseconds for dots approximately 4nm in diameter, an order of magnitude greater than $\tau_{2'}$ in the solution; however, fits to transients of the array contain a time constant, τ_2 , with an excitation probability dependent amplitude, which agrees with the Robel, et al. analysis. Additionally, the fit to the solution transient results in $\tau_{2'}$ with a positive coefficient, which indicates an increase in ESA is happening over this time, rather than decay toward zero.

The AR lifetime assigned to the array, τ_2 , is similar for excitation centered at 570nm with different $\langle N \rangle$ and for excitation centered at 560nm with $\langle N \rangle = 0.229$. The short time constant, $\tau_{2'}$, in the array is similar in magnitude to $\tau_{2'}$ for the solution, but the opposite sign on the coefficient indicates different dynamics are occurring in the array than for the solution.

In addition, transients were taken of the films at different $\langle N \rangle$ while keeping the sample stationary. These transients show agreement, within noise, between stationary and refreshed transients at $\langle N \rangle \approx 0.25$. At $\langle N \rangle \approx 0.50$, stationary and refreshed transients begin to deviate around 200ps, well past the expected AR lifetime.

| | $\langle N \rangle$ | A | $\tau_{2'}$ | B | τ_2 | C | τ_1 |
|--------------------------|---------------------|------------------|--------------------------|------------------|--------------------------|------------------|----------------|
| <i>Solution at 570nm</i> | 0.263 | 0.15 ± 0.02 | $7.76 \pm 2.19\text{ps}$ | - | - | -1.21 ± 0.08 | $> 1\text{ns}$ |
| <i>Film at 570nm</i> | 0.271 | -0.78 ± 0.11 | $6.14 \pm 1.77\text{ps}$ | -1.06 ± 0.12 | $83.7 \pm 20.7\text{ps}$ | -1.56 ± 0.14 | $> 1\text{ns}$ |
| | 0.455 | -0.81 ± 0.12 | $7.11 \pm 2.47\text{ps}$ | -1.98 ± 0.12 | $76.8 \pm 10.7\text{ps}$ | -0.40 ± 0.09 | $> 1\text{ns}$ |
| <i>Film at 560nm</i> | 0.229 | -0.84 ± 0.07 | $4.77 \pm 0.89\text{ps}$ | -0.50 ± 0.17 | $76.3 \pm 47.5\text{ps}$ | -0.90 ± 0.21 | $> 1\text{ns}$ |
| | 0.569 | -0.90 ± 0.19 | $1.99 \pm 0.56\text{ps}$ | -0.69 ± 0.07 | $41.3 \pm 10.5\text{ps}$ | -0.46 ± 0.09 | 900ps |

Table 5.1: Coefficients and decay times for colloidal solution and EDT-treated array of 4nm diameter PbS based on exponential fits. A , B , and C are coefficients in the multiexponential fit, $Ae^{-t/\tau_2'} + Be^{-t/\tau_2} + Ce^{-t/\tau_1}$. Similar to other samples, discussed in Chapters 2 and 3, an additional short lifetime, labeled $\tau_{2'}$ appears here, but is an order of magnitude less than the expected AR lifetime.

5.4 Conclusion

Degenerate pump-probe transients taken of a colloidal solution and an EDT-treated array of 4nm diameter PbS QDs, with the pulse spectrum centered at or near the E_1 transition, are dominated by ESA, seen by the negative transient signals. Exciton lifetimes are assigned based on the assumption that signal decay toward zero implies Auger Recombination of carriers, but the photophysics at the E_1 transition are likely more complicated than this preliminary experiment and analysis address.

The relatively short lifetime in the solution corresponds to an increase in the negative signal, suggesting enhanced recombination mechanisms at this high energy transition for the colloidal sample. Further characterization of the sample is needed to ensure that inadequate surface passivation does not lead to trap states and QD charging that may enhance Auger Recombination and lead to an increase in the rate of recombination. In addition, repeating degenerate pump-probe on an air free array is necessary to qualify any effects from sample degradation after exposure to the atmosphere.

Although further investigation is needed, the initial results showing faster decay of the ESA

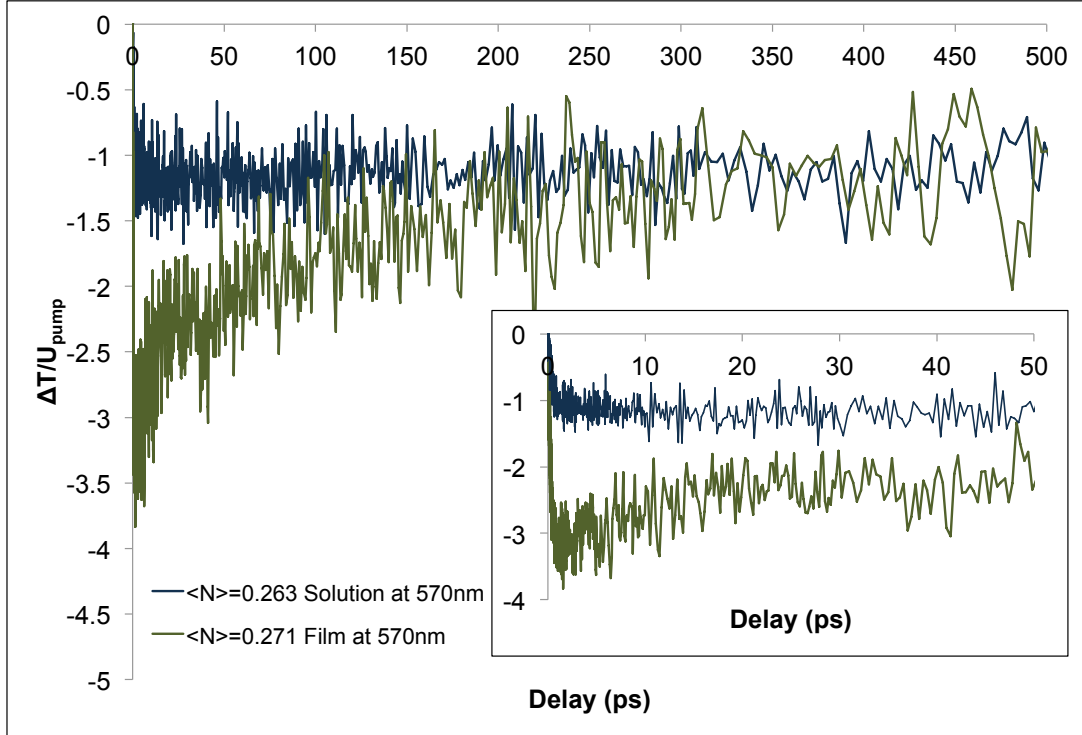


Figure 5.3: Degenerate pump-probe transients, recorded with the center of the pulse spectrum at 570nm and refreshed between laser shots with a 40ms resampling time, of 4nm diameter PbS as a colloidal solution in hexane and as an EDT-treated array with $\langle N \rangle \approx 0.25$. The inset shows the transients over the first 50ps and illustrates the differences at early times. Both transients are normalized by the average pump power.

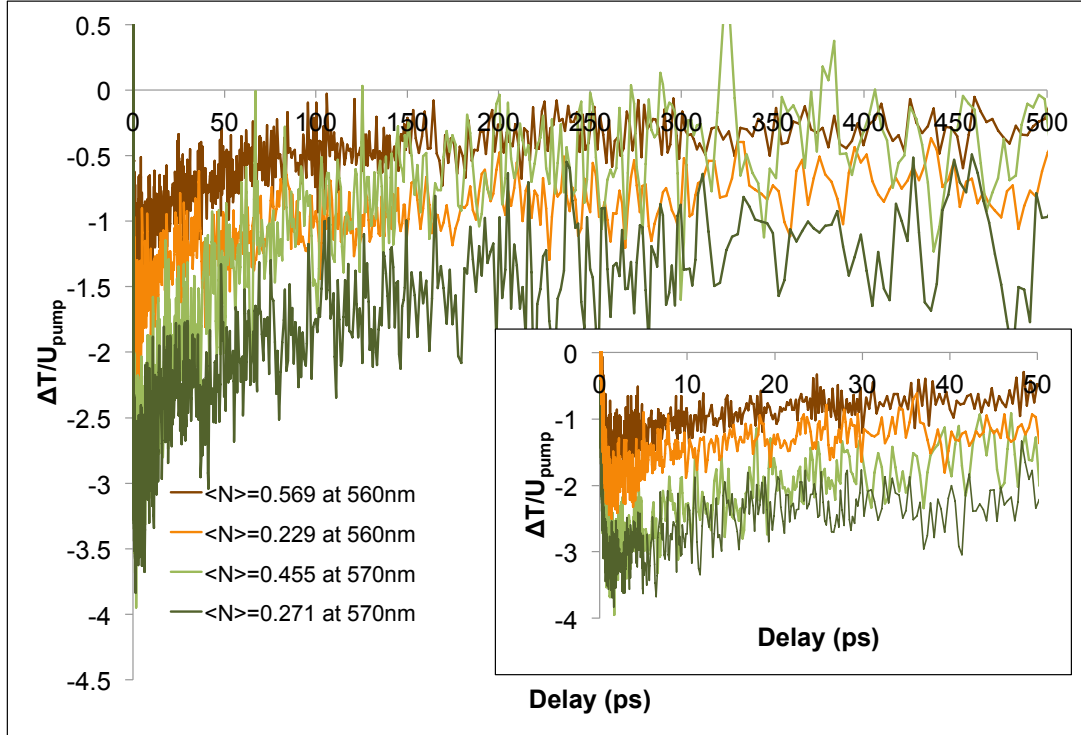


Figure 5.4: Degenerate pump-probe transients, recorded with the center of the pulse spectrum at 560nm and at 570nm and refreshed between laser shots with a 40ms resampling time, of 4nm diameter PbS as an EDT-treated array with $\langle N \rangle \approx 0.25$ and ≈ 0.50 . Transients are normalized by average pump power. At both excitation wavelengths, transients display a large negative signal at early times, indicating ESA. The inset illustrates the similarity in the shape of the transients over the first 50ps.

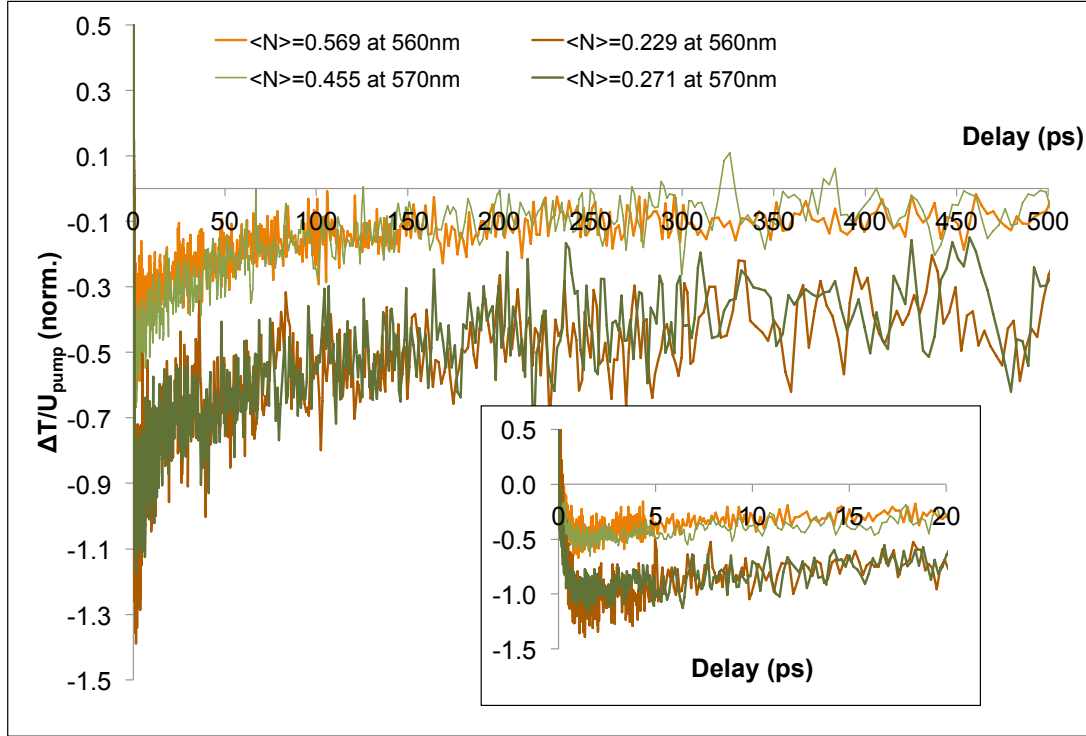


Figure 5.5: Degenerate pump-probe transients, recorded with the center of the pulse spectrum at 560nm and at 570nm and refreshed between laser shots with a 40ms resampling time, of 4nm diameter PbS as an EDT-treated array with $\langle N \rangle \approx 0.25$ and ≈ 0.50 . Transients are normalized at 1ps to compare the shape and the early time dynamics when the pulse spectrum is centered at 560nm and at 570nm. With 1ps normalization, transients exhibit agreement within the signal-to-noise at both early (inset) and late times except for a small bleach at time zero that occurs in transients excited at 560nm (see Figure 5.6), but is not seen in any transients at 570nm.

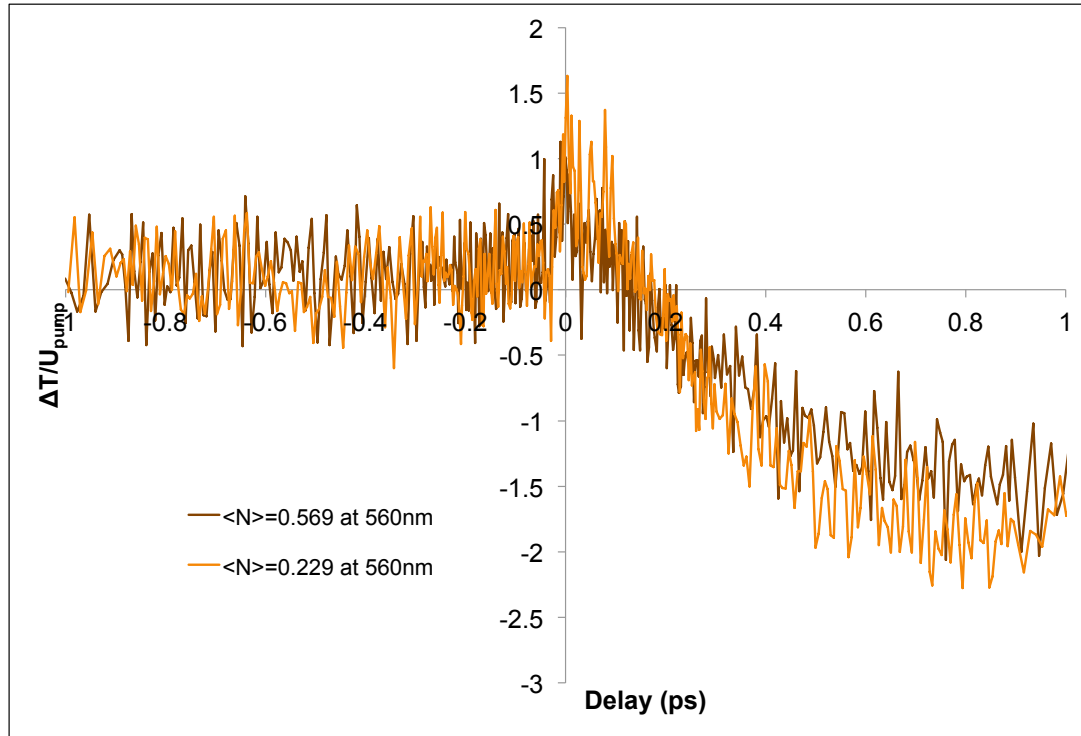


Figure 5.6: The first picosecond of degenerate pump-probe transients, recorded with the center of the pulse spectrum at 560nm and refreshed between laser shots with a 40ms resampling time, of the EDT-treated array of PbS. Transients are normalized by the average pump power. An initial, short-lived bleach is observed that is not seen in transients of the array or solution when the pulse spectrum is centered at 570nm. This positive signal begins just before time zero and continues to almost 200fs, indicating an initial GSB.

signal to zero and an additional lifetime for the array compared to the solution suggest fast energy or electron transfer between dots, not present in the colloidal sample, which leads to an increase in the number of excitons per QD that would not otherwise occur at that $\langle N \rangle$. In addition, a similar examination of larger diameter quantum dots in solution and as coupled arrays, which have an E_1 transition at $3E_g$ or higher (CM threshold), will help to clarify the implications for carrier multiplication in quantum dots and potential photovoltaic devices.

5.5 References

- [1] J. M. Luther, M. Law, Q. Song, C. L. Perkins, M. C. Beard, and A. J. Nozik, “Structural, optical, and electrical properties of self-assembled films of PbSe nanocrystals treated with 1, 2-ethanedithiol,” ACS Nano, vol. 2, no. 2, pp. 271–280, 2008.
- [2] M. C. Beard, A. G. Midgett, M. Law, O. E. Semonin, R. J. Ellingson, and A. J. Nozik, “Variations in the quantum efficiency of multiple exciton generation for a series of chemically treated PbSe nanocrystal films,” Nano Letters, vol. 9, no. 2, pp. 836–845, 2009.
- [3] A. P. Spencer, R. J. Hill, W. K. Peters, D. Baranov, B. Cho, and D. M. Jonas, “Probed-volume sample renewal by beam scanning with applications to noncollinear pump-probe spectroscopy at kilohertz repetition rates,” (in preparation), 2014.
- [4] C. B. Murray, S. Sun, W. Gaschler, H. DoyLe, T. A. Betley, and C. R. Kagan, “Colloidal synthesis of nanocrystals and nanocrystal superlattices,” IBM Journal of Research and Development, vol. 45, no. 1, pp. 47–56, 2001.
- [5] M. A. Hines and G. D. Scholes, “Colloidal PbS nanocrystals with size-tunable near-infrared emission: observation of post-synthesis self-narrowing of the particle size distribution,” Advanced Materials, vol. 15, no. 21, pp. 1844–1849, 2003.
- [6] P. Guyot-Sionnest, “Electrical transport in colloidal quantum dot films,” The Journal of Physical Chemistry Letters, vol. 3, no. 9, pp. 1169–1175, 2012.
- [7] H. Döllefeld, H. Weller, and A. Eychemüller, “Semiconductor nanocrystal assemblies: experimental pitfalls and a simple model of particle-particle interaction,” The Journal of Physical Chemistry B, vol. 106, no. 22, pp. 5604–5608, 2002.
- [8] C. Leatherdale and M. Bawendi, “Observation of solvatochromism in CdSe colloidal quantum dots,” Physical Review B, vol. 63, no. 16, p. 165315, 2001.
- [9] J. Tang, L. Brzozowski, D. A. R. Barkhouse, X. Wang, R. Debnath, R. Wolowiec, E. Palmiano, L. Levina, A. G. Pattantyus-Abraham, D. Jamakosmanovic, et al., “Quantum dot photovoltaics in the extreme quantum confinement regime: the surface-chemical origins of exceptional air-and light-stability,” ACS Nano, vol. 4, no. 2, pp. 869–878, 2010.
- [10] I. Robel, R. Gresback, U. Kortshagen, R. D. Schaller, and V. I. Klimov, “Universal size-dependent trend in auger recombination in direct-gap and indirect-gap semiconductor nanocrystals,” Physical Review Letters, vol. 102, no. 17, p. 177404, 2009.

Bibliography

- [1] Wan Ki Bae, Jin Joo, Lazaro A Padilha, Jonghan Won, Doh C Lee, Qianglu Lin, Weonkyu Koh, Hongmei Luo, Victor I Klimov, and Jeffrey M Pietryga, Highly effective surface passivation of pbse quantum dots through reaction with molecular chlorine, Journal of the American Chemical Society **134** (2012), no. 49, 20160–20168.
- [2] L Bakueva, S Musikhin, MA Hines, T-WF Chang, M Tzolov, GD Scholes, and EH Sargent, Size-tunable infrared (1000–1600 nm) electroluminescence from pbs quantum-dot nanocrystals in a semiconducting polymer, Applied Physics Letters **82** (2003), no. 17, 2895–2897.
- [3] AV Barzykin and M Tachiya, Stochastic models of charge carrier dynamics in semiconducting nanosystems, Journal of Physics: Condensed Matter **19** (2007), no. 6, 065105.
- [4] Matthew C Beard, Multiple exciton generation in semiconductor quantum dots, The Journal of Physical Chemistry Letters **2** (2011), no. 11, 1282–1288.
- [5] Matthew C Beard and Randy J Ellingson, Multiple exciton generation in semiconductor nanocrystals: Toward efficient solar energy conversion, Laser & Photonics Reviews **2** (2008), no. 5, 377–399.
- [6] Matthew C Beard, Kelly P Knutsen, Pingrong Yu, Joseph M Luther, Qing Song, Wyatt K Metzger, Randy J Ellingson, and Arthur J Nozik, Multiple exciton generation in colloidal silicon nanocrystals, Nano Letters **7** (2007), no. 8, 2506–2512.
- [7] Matthew C Beard, Aaron G Midgett, Mark C Hanna, Joseph M Luther, Barbara K Hughes, and Arthur J Nozik, Comparing multiple exciton generation in quantum dots to impact ionization in bulk semiconductors: implications for enhancement of solar energy conversion, Nano letters **10** (2010), no. 8, 3019–3027.
- [8] Matthew C Beard, Aaron G Midgett, Matt Law, Octavi E Semonin, Randy J Ellingson, and Arthur J Nozik, Variations in the quantum efficiency of multiple exciton generation for a series of chemically treated pbse nanocrystal films, Nano letters **9** (2009), no. 2, 836–845.
- [9] DS Boudreaux, F Williams, and AJ Nozik, Hot carrier injection at semiconductor-electrolyte junctions, Journal of Applied Physics **51** (1980), no. 4, 2158–2163.
- [10] Byungmoon Cho, William K Peters, Robert J Hill, Trevor L Courtney, and David M Jonas, Bulklike hot carrier dynamics in lead sulfide quantum dots, Nano letters **10** (2010), no. 7, 2498–2505.

- [11] Joshua J Choi, Yee-Fun Lim, MitkEl B Santiago-Berrios, Matthew Oh, Byung-Ryool Hyun, Liangfeng Sun, Adam C Bartnik, Augusta Goedhart, George G Malliaras, Hector D Abrua, et al., Pbse nanocrystal excitonic solar cells, *Nano letters* **9** (2009), no. 11, 3749–3755.
- [12] Julian D. Dole, Perturbation methods in applied mathematics, Winsdell Publishing Company, 1967.
- [13] Herwig Döllefeld, Horst Weller, and Alexander Eychmüller, Semiconductor nanocrystal assemblies: experimental pitfalls and a simple model of particle-particle interaction, *The Journal of Physical Chemistry B* **106** (2002), no. 22, 5604–5608.
- [14] Randy J Ellingson, Matthew C Beard, Justin C Johnson, Pingrong Yu, Olga I Micic, Arthur J Nozik, Andrew Shabaev, and Alexander L Efros, Highly efficient multiple exciton generation in colloidal pbse and pbs quantum dots, *Nano Letters* **5** (2005), no. 5, 865–871.
- [15] Martin A Green, Third generation photovoltaics: advanced solar energy conversion, Springer, 2003.
- [16] MC Hanna and AJ Nozik, Solar conversion efficiency of photovoltaic and photoelectrolysis cells with carrier multiplication absorbers, *Journal of Applied Physics* **100** (2006), no. 7, 074510–074510.
- [17] A Haug, Band-to-band auger recombination in semiconductors, *Journal of Physics and Chemistry of Solids* **49** (1988), no. 6, 599–605.
- [18] Robert J. Hill, Enabling two-dimensional fourier transform electronic spectroscopy on quantum dots, Ph.D. thesis, University of Colorado at Boulder, 2013.
- [19] Alexander H Ip, Susanna M Thon, Sjoerd Hoogland, Oleksandr Voznyy, David Zhitomirsky, Ratan Debnath, Larissa Levina, Lisa R Rollny, Graham H Carey, Armin Fischer, et al., Hybrid passivated colloidal quantum dot solids, *Nature nanotechnology* (2012).
- [20] Robert Klann, Thomas Hofer, Rainer Buhleier, Thomas Elsaesser, and Jens W Tomm, Fast recombination processes in lead chalcogenide semiconductors studied via transient optical nonlinearities, *Journal of applied physics* **77** (1995), no. 1, 277–286.
- [21] VI Klimov, JA McGuire, RD Schaller, and VI Rupasov, Scaling of multiexciton lifetimes in semiconductor nanocrystals, *Physical Review B* **77** (2008), no. 19, 195324.
- [22] VI Klimov, AA Mikhailovsky, DW McBranch, CA Leatherdale, and MG Bawendi, Quantization of multiparticle auger rates in semiconductor quantum dots, *Science* **287** (2000), no. 5455, 1011–1013.
- [23] Victor I Klimov, Multiexciton phenomena in semiconductor nanocrystals, *Nanocrystal Quantum Dots* **2** (2010).
- [24] Sabine Kolodinski, Jurgen H Werner, Thomas Wittchen, and Hans J Queisser, Quantum efficiencies exceeding unity due to impact ionization in silicon solar cells, *Applied Physics Letters* **63** (1993), no. 17, 2405–2407.
- [25] Peter T. Landsberg, Recombination in semiconductors, Cambridge University Press, 1991.

- [26] PT Landsberg, H Nussbaumer, and G Willeke, Band-band impact ionization and solar cell efficiency, Journal of applied physics **74** (1993), no. 2, 1451–1452.
- [27] Henry Lao, Linear acoustic processes in rocket engines, Ph.D. thesis, University of Colorado at Boulder, 1979.
- [28] Q. Lao, D. R. Kassoy, and K. Kirkkopru, Nonlinear acoustic processes in rocket engines, J. Fluid Mechanics **3** (1997), 245–261.
- [29] Matt Law, Joseph M Luther, Qing Song, Barbara K Hughes, Craig L Perkins, and Arthur J Nozik, Structural, optical, and electrical properties of pbse nanocrystal solids treated thermally or with simple amines, Journal of the American Chemical Society **130** (2008), no. 18, 5974–5985.
- [30] CA Leatherdale and MG Bawendi, Observation of solvatochromism in cdse colloidal quantum dots, Physical Review B **63** (2001), no. 16, 165315.
- [31] Antonio Luque, Will we exceed 50% efficiency in photovoltaics?, Journal of Applied Physics **110** (2011), no. 3, 031301–031301.
- [32] Joseph M Luther, Matthew C Beard, Qing Song, Matt Law, Randy J Ellingson, and Arthur J Nozik, Multiple exciton generation in films of electronically coupled pbse quantum dots, Nano letters **7** (2007), no. 6, 1779–1784.
- [33] Joseph M Luther, Matt Law, Matthew C Beard, Qing Song, Matthew O Reese, Randy J Ellingson, and Arthur J Nozik, Schottky solar cells based on colloidal nanocrystal films, Nano Letters **8** (2008), no. 10, 3488–3492.
- [34] Joseph M Luther, Matt Law, Qing Song, Craig L Perkins, Matthew C Beard, and Arthur J Nozik, Structural, optical, and electrical properties of self-assembled films of pbse nanocrystals treated with 1, 2-ethanedithiol, Acs Nano **2** (2008), no. 2, 271–280.
- [35] John A McGuire, Jin Joo, Jeffrey M Pietryga, Richard D Schaller, and Victor I Klimov, New aspects of carrier multiplication in semiconductor nanocrystals, Accounts of chemical research **41** (2008), no. 12, 1810–1819.
- [36] John A McGuire, Milan Sykora, Jin Joo, Jeffrey M Pietryga, and Victor I Klimov, Apparent versus true carrier multiplication yields in semiconductor nanocrystals, Nano letters **10** (2010), no. 6, 2049–2057.
- [37] Aaron G Midgett, Hugh W Hillhouse, Barbara K Hughes, Arthur J Nozik, and Matthew C Beard, Flowing versus static conditions for measuring multiple exciton generation in pbse quantum dots, The Journal of Physical Chemistry C **114** (2010), no. 41, 17486–17500.
- [38] James E Murphy, Matthew C Beard, and Arthur J Nozik, Time-resolved photoconductivity of pbse nanocrystal arrays, The Journal of Physical Chemistry B **110** (2006), no. 50, 25455–25461.
- [39] Gautham Nair, Liang-Yi Chang, Scott M Geyer, and Mouni G Bawendi, Perspective on the prospects of a carrier multiplication nanocrystal solar cell, Nano letters **11** (2011), no. 5, 2145–2151.

- [40] Gautham Nair, Scott M Geyer, Liang-Yi Chang, and Mouni G Bawendi, Carrier multiplication yields in pbs and pbse nanocrystals measured by transient photoluminescence, *Physical Review B* **78** (2008), no. 12, 125325.
- [41] U.S.D.O.E. National Renewable Energy Laboratory, Reference solar spectral irradiance, April 2013.
- [42] ———, Research cell efficiency records, April 2013.
- [43] Zhijun Ning, Yuan Ren, Sjoerd Hoogland, Oleksandr Voznyy, Larissa Levina, Philipp Stadler, Xinzhen Lan, David Zhitomirsky, and Edward H Sargent, All-inorganic colloidal quantum dot photovoltaics employing solution-phase halide passivation, *Advanced Materials* **24** (2012), no. 47, 6295–6299.
- [44] Lazaro A Padilha, John T Stewart, Richard L Sandberg, Wan Ki Bae, Weon-Kyu Koh, Jeffrey M Pietryga, and Victor I Klimov, Carrier multiplication in semiconductor nanocrystals: Influence of size, shape, and composition, *Accounts of chemical research* (2013).
- [45] William K. Peters and David M. Jonas, personal communication, 2013.
- [46] JJH Pijpers, R Ulbricht, KJ Tielrooij, A Osherov, Y Golan, C Delerue, G Allan, and M Bonn, Assessment of carrier-multiplication efficiency in bulk pbse and pbs, *Nature Physics* **5** (2009), no. 11, 811–814.
- [47] Yu I Ravich and D Khokhlov, Lead chalcogenides: basic physical features, *Lead Chalcogenides: Physics & Applications*; Khokhlov, D., Ed.; Taylor and Francis: New York (2003), 3.
- [48] István Robel, Ryan Gresback, Uwe Kortshagen, Richard D Schaller, and Victor I Klimov, Universal size-dependent trend in auger recombination in direct-gap and indirect-gap semiconductor nanocrystals, *Physical review letters* **102** (2009), no. 17, 177404.
- [49] Robert T Ross and Arthur J Nozik, Efficiency of hot-carrier solar energy converters, *Journal of Applied Physics* **53** (1982), no. 5, 3813–3818.
- [50] Sven Rühle, Menny Shalom, and Arie Zaban, Quantum-dot-sensitized solar cells, *ChemPhysChem* **11** (2010), no. 11, 2290–2304.
- [51] Justin B Sambur, Thomas Novet, and BA Parkinson, Multiple exciton collection in a sensitized photovoltaic system, *Science* **330** (2010), no. 6000, 63–66.
- [52] Richard D Schaller and Victor I Klimov, High efficiency carrier multiplication in pbse nanocrystals: implications for solar energy conversion, *Physical review letters* **92** (2004), no. 18, 186601.
- [53] Richard D Schaller, Melissa A Petruska, and Victor I Klimov, Effect of electronic structure on carrier multiplication efficiency: Comparative study of pbse and cdse nanocrystals, *Applied Physics Letters* **87** (2005), no. 25, 253102–253102.
- [54] Richard D Schaller, Milan Sykora, Jeffrey M Pietryga, and Victor I Klimov, Seven excitons at a cost of one: redefining the limits for conversion efficiency of photons into charge carriers, *Nano Letters* **6** (2006), no. 3, 424–429.

- [55] Octavi E Semonin, Joseph M Luther, and Matthew C Beard, Quantum dots for next-generation photovoltaics, *Materials Today* **15** (2012), no. 11, 508–515.
- [56] Octavi E Semonin, Joseph M Luther, Sukgeun Choi, Hsiang-Yu Chen, Jianbo Gao, Arthur J Nozik, and Matthew C Beard, Peak external photocurrent quantum efficiency exceeding 100% via meg in a quantum dot solar cell, *Science* **334** (2011), no. 6062, 1530–1533.
- [57] William Shockley and Hans J Queisser, Detailed balance limit of efficiency of p-n junction solar cells, *Journal of Applied Physics* **32** (1961), no. 3, 510–519.
- [58] T. M. Smitty, R. L. Coach, and F. B. Höndra, Unsteady flow in simulated solid rocket motors, 16st Aerospace Sciences Meeting, 78, no. 0112, AIAA, 1978.
- [59] Dmitri V Talapin and Christopher B Murray, Pbse nanocrystal solids for n-and p-channel thin film field-effect transistors, *Science* **310** (2005), no. 5745, 86–89.
- [60] Jiang Tang, Lukasz Brzozowski, D Aaron R Barkhouse, Xihua Wang, Ratan Debnath, Remigiusz Wolowiec, Elenita Palmiano, Larissa Levina, Andras G Pattantyus-Abraham, Damir Jamakosmanovic, et al., Quantum dot photovoltaics in the extreme quantum confinement regime: the surface-chemical origins of exceptional air-and light-stability, *ACS nano* **4** (2010), no. 2, 869–878.
- [61] Jiang Tang, Kyle W Kemp, Sjoerd Hoogland, Kwang S Jeong, Huan Liu, Larissa Levina, Melissa Furukawa, Xihua Wang, Ratan Debnath, Dongkyu Cha, et al., Colloidal-quantum-dot photovoltaics using atomic-ligand passivation, *Nature materials* **10** (2011), no. 10, 765–771.
- [62] Frank W Wise, Lead salt quantum dots: the limit of strong quantum confinement, *Accounts of Chemical Research* **33** (2000), no. 11, 773–780.

Appendix A

Additional Figures

Figures Appendix: This Appendix includes additional figures referred to in Chapters 2-5.



Figure A.1: Chem-Vac[™] Chem-Cap[®] valve with single sidearm from Chemglass Life Sciences.

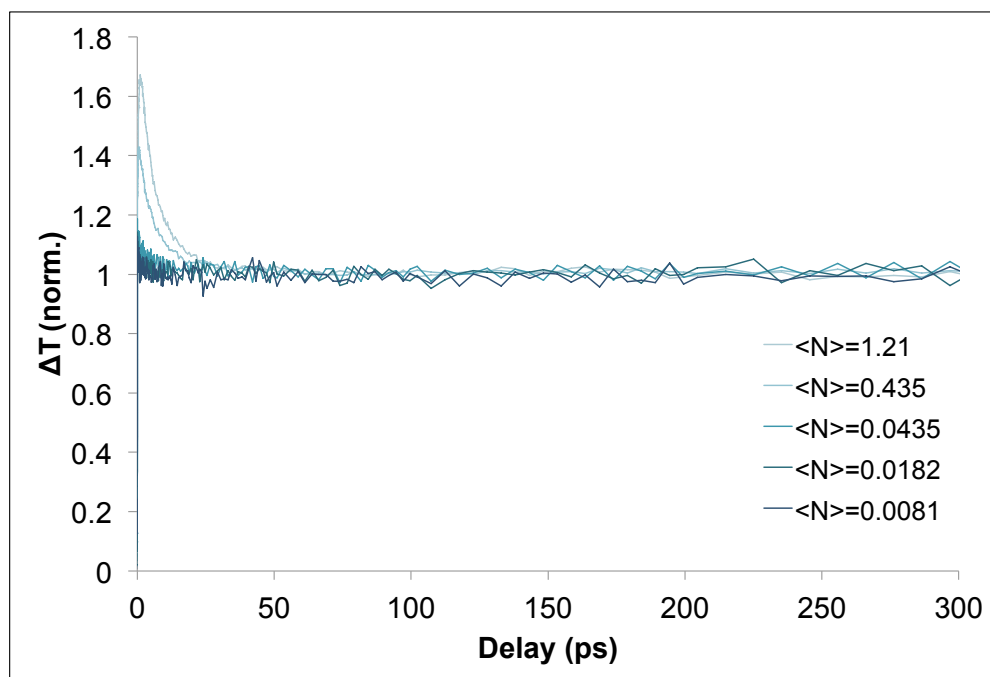


Figure A.2: A second set of degenerate pump-probe transients were recorded in addition to those shown in Chapter 2, with a pulse spectrum centered at 800nm, of 1.9nm oleate-capped PbS QDs in hexane ($OD(800\text{nm})=0.12$ and $E_g=820\text{nm}$). Transients were normalized at long-time using the average amplitude between 0.5ns and 1ns.

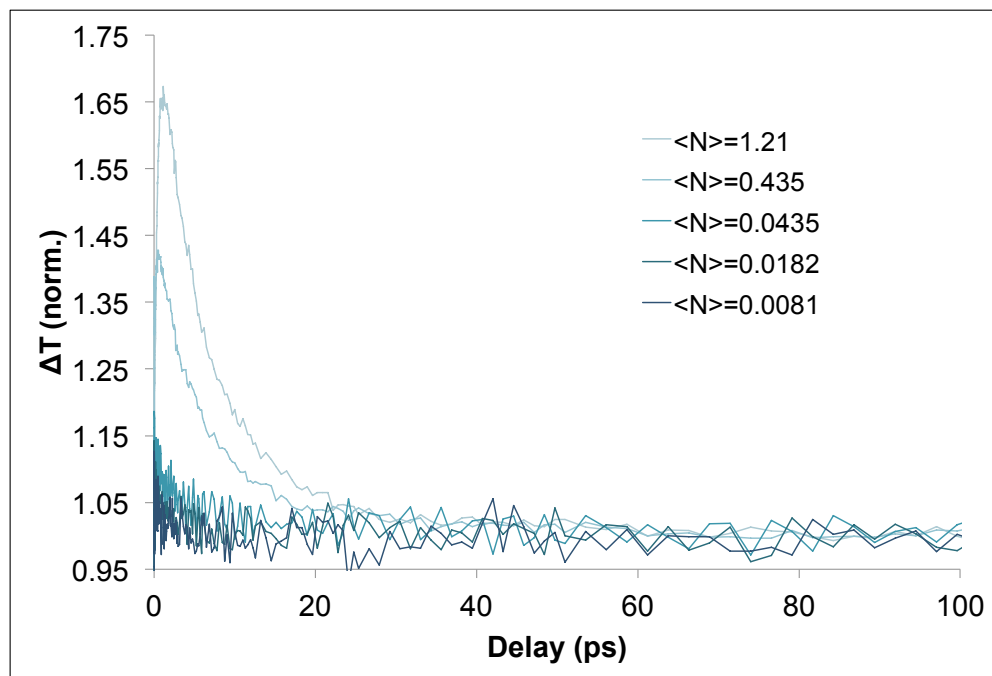


Figure A.3: Assuming that the oleate-capped PbS solution transient with $\langle N \rangle = 0.0081$ includes only a single exciton decay signal, tail-matching multiples are subtracted from the $\langle N \rangle = 1.57$, $\langle N \rangle = 0.431$, and $\langle N \rangle = 0.0431$ transients of the solution shown in Figure A.2. The resulting data and fits are shown here.

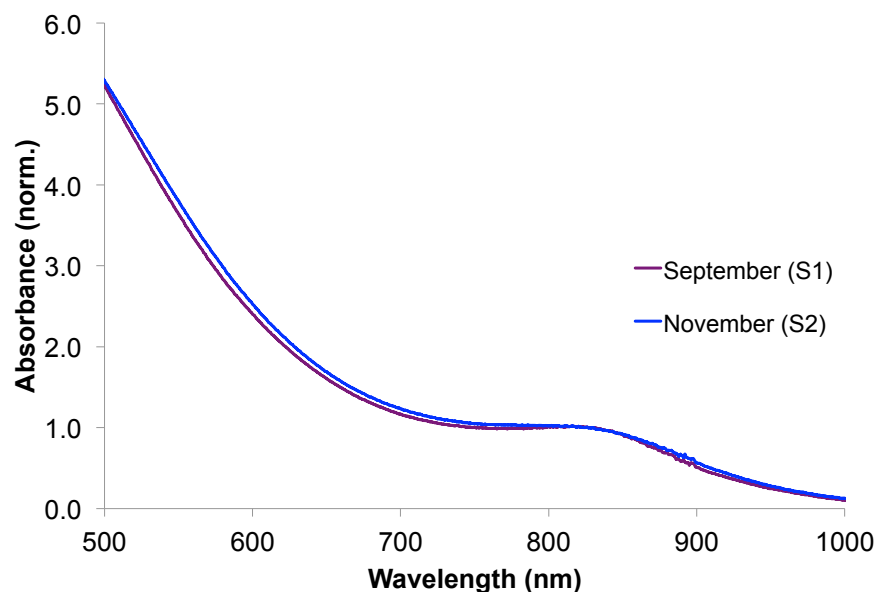


Figure A.4: Linear absorption spectra of 1.9nm diameter octylamine-treated PbS in hexane. Individual samples were taken at different times from stock solution stored in the glovebox. S1 was taken on September 24, 2012 and S2 was taken on November 13, 2012, less than two months apart.

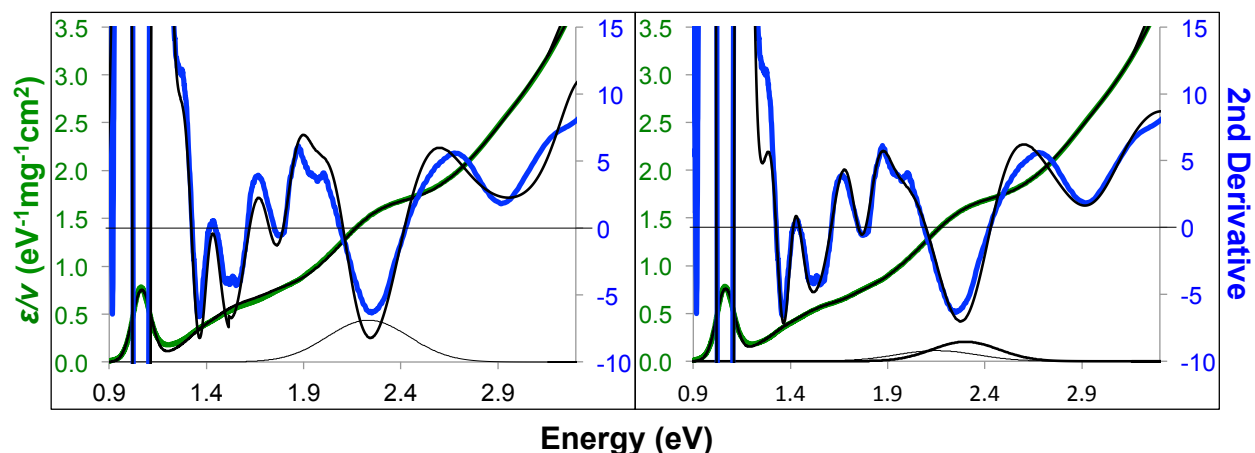


Figure A.5: Absorption spectra of 4.3nm diameter PbS QDs are shown in green with the second derivative in blue. Fits to absorption spectra and the second derivative are overlaid in black and based on a third order polynomial background with a sum of Gaussians to describe discrete transitions. The figure on the left is a fit using only a single Gaussian at the E_1 transition while the figure on the right uses two Gaussians to fit the area around the E_1 transition. Only the Gaussians fit at E_1 transitions are shown under each absorption curve.

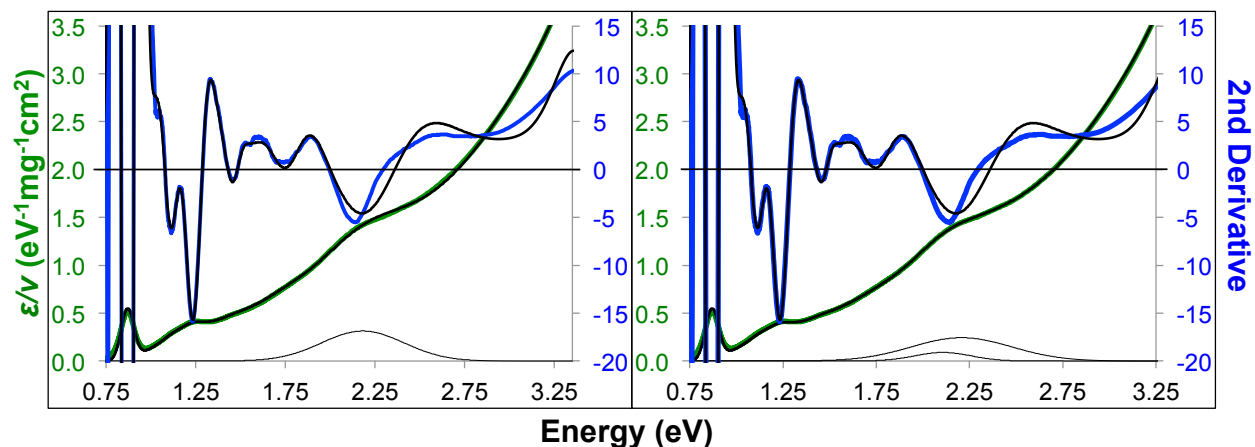


Figure A.6: Absorption spectra of 5.2nm diameter PbS QDs are shown in green with the second derivative in blue. Fits to absorption spectra and the second derivative are overlaid in black and based on a third order polynomial background with a sum of Gaussians to describe discrete transitions. The figure on the left is a fit using only a single Gaussian at the E_1 transition while the figure on the right uses two Gaussians to fit the area around the E_1 transition. Only the Gaussians fit at E_1 transitions are shown under each absorption curve.

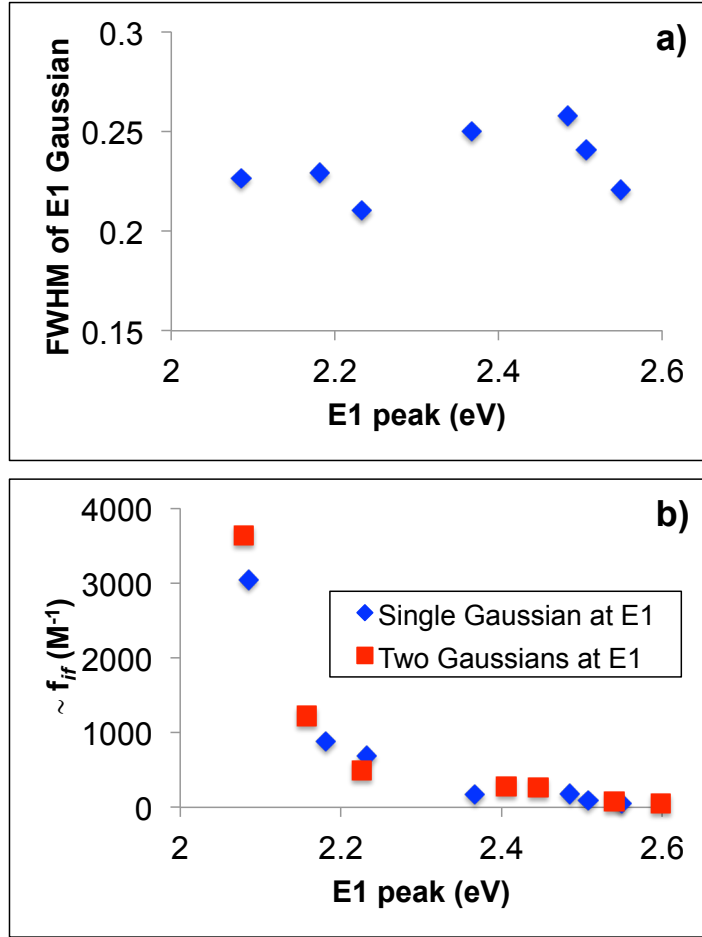


Figure A.7: **a)** Full width at the half maximum (FWHM) of the single Gaussian fit for the E_1 transition versus the energy peak (eV). The FWHM increases as the location of the E_1 peak increases in energy (with decreasing QD diameter) until it reaches a maximum at 2.48eV (2.3nm diameter) and then begins decreasing at 2.51eV (1.9nm diameter). **b)** The y-axis is proportional to the oscillator strength (f_{if}) of the E_1 transition and the x-axis is the energy peak (eV) of the transition. Blue diamonds represent f_{if} for the single Gaussian fit to the E_1 transition while red squares are the sum of f_{if} for the fit with two Gaussians at the E_1 transition. The E_1 peak energy for the two Gaussian fit is taken to be the average of the two peak energies. The oscillator strengths the different fits follow the same trend although the peak energies do not agree exactly.